POLITECNICO DI TORINO

DIPARTIMENTO DI INGEGNERIA MECCANICA E AEROSPAZIALE

Master degree course in Aerospace Engineering

Master Degree Thesis

Turbo-Electric propulsion system of a high bypass-ratio turbofan engine for civil liner aircraft

Supervisor
prof. Lorenzo Casalino

Candidate
Mirko Zafferetti
matricola: s234649

Internship supervisor
Prof. Vassilios Pachidis
Director of Rolls-Royce UTC
Head of Gas Turbine Engineering Group

Academic year 2017 – 2018

To my parents.

"Regarde attentivement, car ce que tu vas voir
n'est plus ce que tu viens de voir."
Leonardo da Vinci

Summary

In 2000s era, aircraft propulsion systems are achieving an outstanding level of efficiency. Design optimization further increases components' performance, while lean combustion processes tend to reduce CO_2 and NO_x emissions. However, pollution reduction targets, especially those imposed for the next 30 years, are extremely strict and demanding, so much that conventional architectures, based on the thermodynamic Brayton cycle, can not fulfil them. Because of this main reason, alternative energies has to be taken into account, and precisely the electric one is going to be the leader. Coupling a gas-turbine engine within an electric propulsion system is one of the main challenges which aeronautical industries are facing to, but it is also one of the principal ways forward in order to meet emissions' goals. This new configuration, which is actually a novelty, aimed at reducing fuel burn by feeding power to the low pressure spool through an external source, i.e. an electric motor powered by an energy storage system, like the one represented by batteries. In this way, the hybridization process takes place and the percentage of electrical power to the total required, the so called power-split, is chosen as a design variable. If considering the propulsion system alone, the immediate consequence is a surprisingly reduction in fuel consumption, along with a possible weight saving coming from the fact that the low pressure turbine does not need all its stages any more, and can be resized smaller. However, when the engine is integrated within the aircraft, something may change due to their mutual interaction; electrical components' mass comes into play and this is one of the major parameters that is going to affect the overall system. From these considerations, one can expect that there will be an optimum, i.e. a link between weight and electrical power added, that maximizes performance and minimizes emissions. Above this value, determined by actual state-of-the-art technology, trends flip backwards, and further increase the power-split setting will not bring additional benefits. This last could be achieved if current limits will be pushed forward, so as to give rise to a striking revolutionary aircraft concept, the all-electric superconducting one. Superconducting technology, in a nutshell, is based on cryogenic working temperatures, in such a way to eliminate any possible losses coming from the resistance tide meets along its path. Thanks to this, electrical components' power density drops up, and they can be shrank, solving a lot of problems and penalties related to their volume and weight.

Aircraft's hybridization process is actually the main road which will permit a huge reduction of fuel emissions and a subsequent efficiency increment. However, many challenges have to be coped in this process, precisely because it is something new, something involving interdisciplinarity among different engineering branches, something never done before.

Acknowledgements

First of all, great thanks are due to my parents, for always trusting me and especially for their support.
There are other few people I would like to thank, among them Professor Vassilios Pachidis, who gave me the opportunity to come to Cranfield University for performing my final project and for the new and challenging subject he suggested me to work on.
I also thank Dr. Mourouzidis and Dr. Roumeliotis for being my supervisors, for their readiness and for the useful advices they gave to me.
Thanks are also due to Professor Casalino Lorenzo for agreeing to be my supervisor at Politecnico and for his willingness.

Contents

List of Tables

List of Figures

Chapter 1

Introduction

1.1 Background

Since the beginning, dating back to 17^{th} December 1903, when the two inventors Orville and Wilburg Wright flew the world's first and successful airplane [1] on a camp at Kill Devil Hill, in North Carolina, man has constantly pushed the boundary of technology ever further, till nowadays.
A step which significantly marked aviation history was the conception of the gas-turbine engine, simultaneously developed by the English RAF officer Sir Frank Whittle and the German engineer Hans Von Ohain. Both created a power plant capable to sustain high altitude and speed flight, overcoming all the drawbacks related to internal combustion engines. That was how the era of jet-engines was born. Moving on, there have been many improvements concerning propulsion systems: compressor pressure ratio moved from 12 in the late 1950s to about 40, turbine inlet temperature has risen from 1000 K to more than 1700 K in 2000s, and so forth. However, the achievement of more power to reach better performance, other than the need to keep up with aircraft size, increasingly impressive due to the larger number of passengers seats, has led aviation industry to deal with a problem that is anything but trivial, i.e that of pollution.
Here is the reason from which the International Air Transport Association (IATA), in conjunction with the European Commission (EC), stated ambitious emissions reduction targets. By 2035, 30% cutback in propulsive energy should be expected, whereas for the horizon 2050, 75% reduction in CO_2 emissions is prospected [1].
At a first glance, this energy saving is directly translated into propulsion systems' efficiency.

[1] The Flyer I.

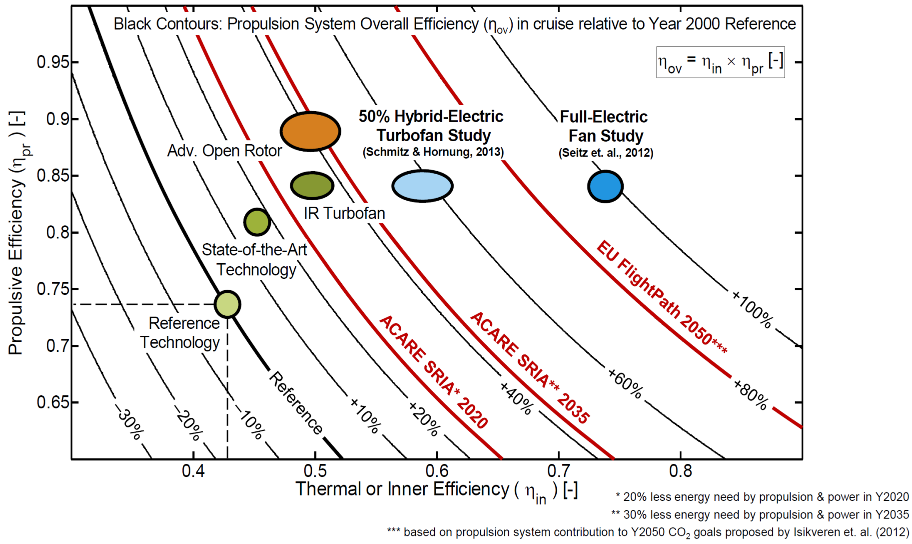

Figure 1.1. Efficiency targets for next-generation aircraft

As can be seen, state-of-the-art technology achieves an overall efficiency $\eta_o \simeq 0.4$, which is not sufficient to join the aforementioned objectives.
Even the National Aeronautics and Space Administration (NASA) set goals to fulfil emissions' requirements, both in terms of noise and pollution [2].
More precisely, the N+ programme is broken down as follows:

- N+1: 32 dB noise reduction, -60% NOx emissions and 33% fuel saving.
- N+2 (2020): 42 dB noise suppression, -75% NOx production and -40% fuel consumption.
- N+3 (2025): -55 dB noise improvement, more than -75% NOx and better than -70% fuel burnt.

In order to reach these targets and overcome present limitations, it is necessary to put aside Brayton thermodynamic cycle, or at least reducing its role (for example building a configuration in which main engines are assisted by power electrical components), and think to new propulsion systems concepts.
In other words, next generation aircraft must have high efficiency, low fuel consumption and low noise emissions.

1.2 Technology level

State of the art technology is still a long way for the implementation of a full electric airplane, the main limitation being the ability of delivering high power with

low weight and low volume components.
Conventional gas-turbine engines have higher specific power in comparison to actual electric motors, limited to about 5 $\frac{kW}{kg}$ (skipping some exception). If the stator or the rotor armature was to be substituted by HTS coils, specific power would reach 10 $\frac{kW}{kg}$, whereas if full superconducting, it would attain even 30 $\frac{kW}{kg}$. Same trends apply to generators. However, such equipment requires a working temperature of 60÷80 K, and the need of cryo-cooling devices is mandatory.
Giving to speak of batteries, 200÷250 $\frac{Wh}{kg}$ is the best energy density storage actually achievable by Li-ion type, while 150÷180 $\frac{W}{kg}$ are power density common values. Other accumulators are characterized by lower performance, indeed; Lead-acid batteries have a specific power of 180 $\frac{W}{kg}$ and Nichel-Cadmium one achieve only 150 $\frac{W}{kg}$. This energy constraints can largely undermine any high-power demanding configuration, as those proposed for aircraft propulsion systems' electrification. If future developments will raise actual values up to 1 $\frac{kW}{kg}$ and more, kerosene based engines would let the place to electric driven fans.
Concerning cables, instead, their mass per unit length is dictated by the amount of current drawn and by the material, usually copper for the conducting core and PVC for the coating; typical values for a single core wire can range from 3 to 30 $\frac{g}{m}$ [27]. Again, the use of superconducting elements, being characterized by near zero resistance to electricity flow, can dramatically reduce components' weight up to 30%.
Another big problem concerns power converters. These modules are dramatically heavy due to their low power to weight ratio (about 1 $\frac{kW}{kg}$). Recent development lead to the introduction of SiC components, which raises this number till about 7 $\frac{kW}{kg}$. Further improvements, should be done with superconducting technology, as can be expected.

1.3 Aims and objectives

The work that is going to be outlined in next chapters focus on turbo-electric propulsion. Emissions targets imposed by relevant authorities led aviation industry to look for new types of propulsive systems, in such a way to reduce fuel burn, and this is how electric propulsion comes into play. Couple a conventional gas-turbine engine with an electric drive-train is one of the actual challenges facing aircraft world, and this is also the main subject of this thesis. The objective is that of analyse the feasibility coming from a partial electrification of a passengers liner aircraft. In order to do so, a conventional turbofan engine is hybridized, i.e a certain amount of power is fed by an electrical motor instead of by the gas-turbine itself. Possible advantages and disadvantages coming from this new architecture are going to be highlighted, putting emphasis on particular variables, such as weight and fuel consumption, along with their mutual interaction during flight phases,

especially the ones related to take-off and climb. A great look upon efficiency and benefits coming from this advanced propulsion concept is made too.
A preliminary investigation of an all-electric architecture is also carried out, in which attention will be given to the impossibility of building a near zero emission aircraft with actual state-of-the-art technology level. The difficulties facing such kind of project will be exposed, other than touching upon possible remedies; in light of this, an unusual type of technology is introduced, i.e that of superconduction. Comparisons will be made between "present" and "future" configurations, along with a general overview on pros and cons.
Finally, conclusions will be drawn and the novelties coming from the present study will be underlined and brought to the attentions of the reader.

Chapter 2

Literature review

Turbo-Electric or Turbo-Hybrid systems are propulsion technologies in which a certain amount of power, needed for propulsion purposes, is produced by an electrical train. Electricity is supplied either by extracting power from conventional gas-turbine engines either by accumulators, such as batteries or fuel cells. The upper level extension of this apparatus results in the so-called Turbo-electric-Distributed-Propulsion (TeDP) configuration, in which thrust is spread all over the span-wise using many small propulsor units. Actually, to achieve better performance, this last is integrated in a blended wing-body (BWB) aircraft, and thrust-units are partially embedded along its trailing edge.

2.1 Historical overview

The use of electricity in the field of aeronautics was first experimented at the end of the nineteenth century, during airship development. By 1883, several dirigible balloons took the flight, but despite their lifting capacity, accumulators' mass seriously limited their speed and range.
Full-sized aircraft prototypes were conceived only in 1973, with the introduction of Nickel-Cadmium batteries, having higher storage to weight ratio in comparison to older technologies. Anyway, current powered-electric aircraft [1] continue suffering from limited payload capacity and endurance, mainly because of the low power-to-weight ratio of electrical staffs. A suitable solution would be the introduction of superconductive elements, as is going to be outlined in next sections, even thought it has its shortcomings, for example hydrogen storage tank volume and cryo-cooler mass, to name a few.
On what concerning TeDP, the first signs dating back to 1954, when Griffith [26]

[1]General aviation class

substituted propellers with a main jet-engine unit located in the body plus a certain number of small gas-turbines installed along the entire wing span (fig.2.1). The idea behind this configuration was that of reducing take-off phases through thrust vectoring.

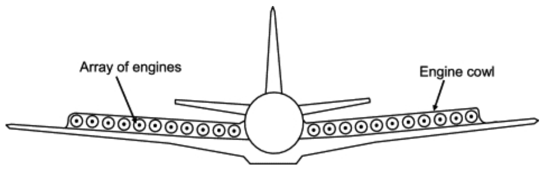

Figure 2.1. Griffith DP model.

From mid-70s, oil crises and the sudden raising of fuel cost gave a strong boost to the study of new architectures, and DP-systems got more attention. During this period, NASA developed several projects on the topic, focusing especially on engine and airframe integration. One of these consisted of a four gas-turbine engines Convair-plane driving sixteen fans arranged along the wing's trailing edge. Furthermore, the sucking effect produced by the propulsors delayed boundary layer transition on the lifting upper surfaces.
A second challenging preliminary design was a 150 seats liner with STOL capability. In this configuration, hybrid fans are completely embedded in the wing, and are driven by superconducting electric motors. In order to cool the system, liquid hydrogen (LH_2) is stored in tanks located along the fusolage and the same substance is also used as fuel (in combination with kerosene) for two turbo-shaft engines wing tip podded. The aim was to dramatically reduce fuel consumption and to improve efficiency raising bypass ratio.
The latest revolutionary idea born in 2006, with the blended wing body concept [29]. This is a hybrid wing-body (HWB) aircraft propelled by 12 small bypass-ratio turbofans partially embedded on the rear-upper surface of the airframe and driven by two turbo-shaft engines fitted at the wing tip.

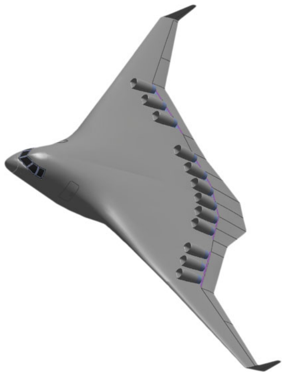

Figure 2.2. Blended wing-body hybrid configuration.

The key characteristics of this new generation aircraft are low noise (thanking to airframe shielding effect), high subsonic cruise efficiency, wider interior volume and STOL operations. In addition, there is a decoupling between power production and propulsive devices, which enable an indipendent optimization of both components, either from the performance point of view either from the operational one (propulsors and core-engines can not necessarily being located close one another).
It is expected that the NASA N3-X could host on board 1000 passengers, but there are some issues related to certification, among them the number of safety emergency exits compared to the amount of seats.
It is important to appreciate that the feasibility of all these projects relies on future technology improvement. Figure 2.3 highlight a projected time-frame with forseeable future technical knowledge level development [34].

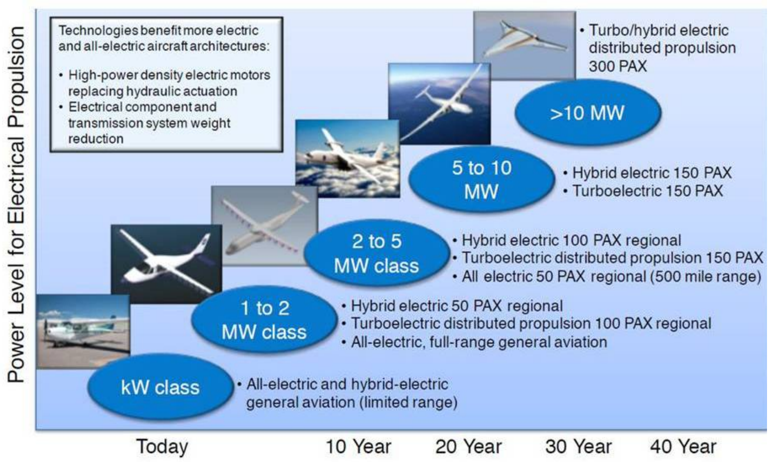

Figure 2.3. Hybrid/electric aircraft's future trends.

Summing up, the concepts on what hybrid/electric propulsion is focusing on are listed hereafter:

- Reduce fuel consumption.
- Cut down CO_2 and NO_x emissions.
- Reduce engine size and improve energy efficiency and management.
- Improve reliability and safety.

2.2 Design options

Over the last few decades, in order to achieve better performance, aircraft engine manufacturers focused on turbofan concept; born from turbojets, these systems split the overall air mass entering the inlet into two flows, namely "hot" and "cold". The first one takes part in the thermodynamic cycle, i.e compression, combustion and expansion, whereas the second one, responsible for most of the thrust produced, bypasses the gas generator and expands in a nozzle. High bypass ratio means lower fuel burn and higher efficiency, but at the expense of a greater fan frontal area.
Drag and weight penalties of such configuration led aviation industry to the definition of new and unconventional design strategies, as described in the following lines.

2.2.1 Propfan concept

The aim is to increase BPR and reduce TSFC by unducting fans. NASA's studies showed 30% saving in fuel consumption at cruise level, at the expense of 20% or more decreasing in thrust to weight ratio. However, there are other penalties that affect this kind of project, two of them are noise and vibrations, which can severely influence structure and passengers' comfort.

Figure 2.4. NASA-Ge propfan.

2.2.2 E-fan X project

Airbus, Rolls-Royce and Siemens have formed a partnership aimed at building a hybrid-electric demonstrator, which is expected to take flight in 2020 [30]. The plan consists of substituting one of the four gas-turbine engines of a BAe 146 by a 2 MW electric motor driven fan. This will pave the way to high-power alternative propulsion systems, other than creating the basis for future electrical drive certification for a clean-sky plane.

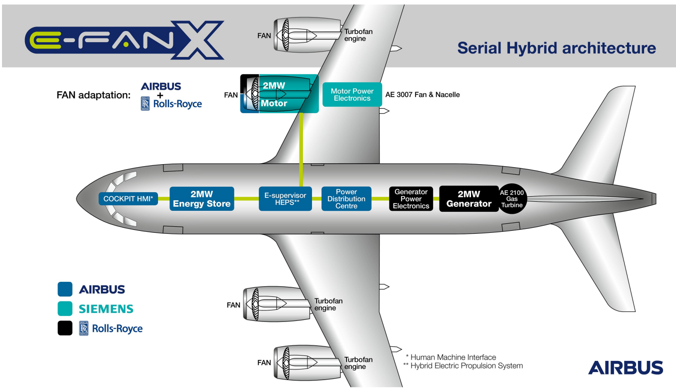

Figure 2.5. E-Fan X architecture.

2.2.3 Bauhaus Luftfahrt project

Conceptual design for future transports reaches its apex with the full electrification of the aircraft; not only subsystems, but also the propulsion system itself is embedded within the electrical architecture. The Ce-liner study [31] aimed at building a zero emission mid-range airplane with about 190 seats. Two 22.2 MW superconducting motors at 3000 V are driven by high specific power Li-ion batteries housed in fourteen LD3 containers, for an overall energy storage mass of 30 tonnes. In order to achieve the target, aggressive improvements need to be made concerning electrical equipment, such as batteries, inverters and motors, due to their low state-of-the-art power density. HTS technology seems to be the most promising road for saving weight and having a competing product.

2.2.4 SUGAR project

Boeing Subsonic Ultra Green Aircraft Research [32] is a prototype powered by hybrid-electric gas-turbine engines, these last conceived by General Electric. The plane is expected to use batteries during take-off and landing phases. This kind of technology could achieve even 70% emissions reduction, but greater advances should be done to reduce electrical components weight, especially that related to energy storage system.

2.2.5 NASA N3-X project

The configuration witch seems to have the greater potential of achieving the imposed restrictions is named Turbo-Electric-Distributed-Propulsion. It consists of two turboshaft engines wing tips mounted, whose primary purpose is to produce mechanical power to drive superconducting generators. The electrical power produced by the latter is than conveyed through a suitable superconducting power grid to many HTS motors, connected to an array of propulsors, partially embedded in the upper rear part of the body, close to the trailing edge. In this case, there are fourteen motors driving as many ducted fans, as shown in the following figure [21].

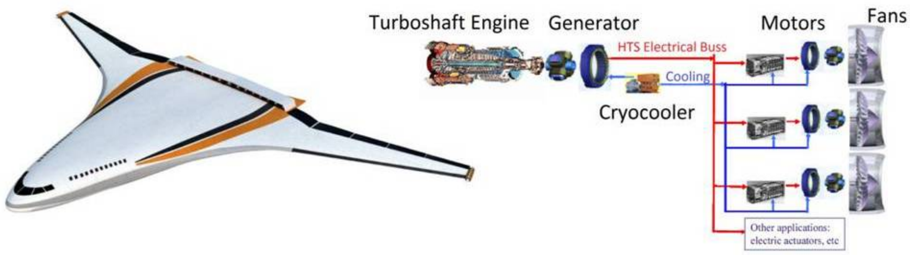

Figure 2.6. NASA N3-X aircraft and propulsion system.

Preliminary analysis showed 70% fuel savings compared to present liner aircraft, and higher efficiency, thanks to the blended wing body configuration and boundary layer ingestion too.

2.3 Power plant architectures

Electric propulsion systems can be characterized by different power plant configurations. In any case, all the drive-trains include some of these components: an energy storage unit, at least two electric drives (motor and generator), a power converter or PMAD, a transmission to route mechanical power from the motor to the fan or the propeller and a bus to carry electrical power, plus others ancillary elements. The connection among these is very similar to that found in car industry, even thought in this area weights and sizes are less significant compared to aviation field.
Among all, three types are of practical interest and are actually taken into account:

- all-electric
- turbo-electric
- hybrid-electric

Each of these can be further divided in sub-architectures.

2.3.1 All-electric

All electric scheme bases the overall energy requirements on accumulators (fig.2.7). In this way, no conventional combustion engines are needed and carbon emissions are almost reduced to zero. As a consequence, being compression, combustion and hot ejection flows processes absent, noise pollution is greatly decreased too.

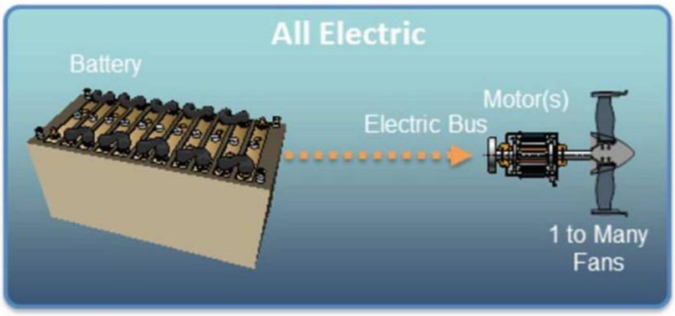

Figure 2.7. All-electric architecture.

2.3.2 Turbo-electric

Turbo-electric scheme do not use any form of electrical storage energy system. In the full turbo-electric arrangement, a turboshaft engine drives a generator, which subsequently powers electric motors; these, in turn, are directly connected to multiple fans (fig.2.8a). Moreover, in the partial configuration, thrust is provided both by a turbofan engine and by motor-driven fans. Electric components provide only a small percentage of the power required and can be sized accordingly (fig.2.8b).

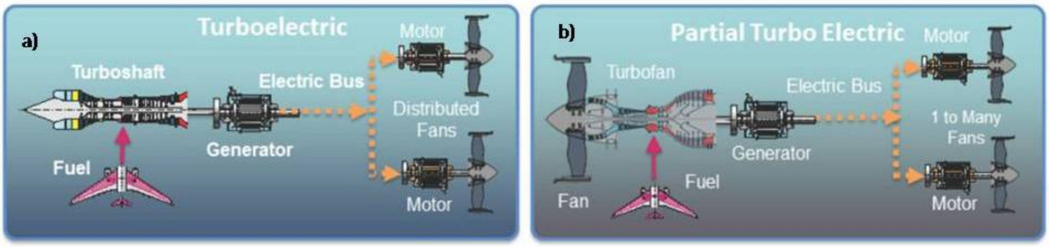

Figure 2.8. Turbo-electric architectures.

2.3.3 Hybrid-electric

Hybrid-electric architectures combine a gas-turbine engine and batteries. The first is used both as for propulsion purposes as for power production, and can also be utilized as a charger. Accumulators, on the other hand, can provide energy over one or more flight phases (for example during taxi-manoeuvres and take-off), depending on design choices.
In this case, two configurations are possible [35]. The series arrangement displayed in figure 2.9 consists of a turbo-shaft connected to a generator, whose purpose is to produce electric energy. This, in turn, drives electrical motors, which are mechanically connected to fans. In some cases, a speed reducing transmission is added between the last two elements, unless changing rotational speed modulating frequency, by adding a power management unit. On the other hand, batteries supply energy to the system through an electrical bus and can be recharged during low-power requirements phases, such as cruise.
One of the advantages of such a drive-train is that the combustion engine, being indirectly connected to the "user", can always operate at its maximum efficiency, thus cutting down fuel consumption. Furthermore, since peak power demands are managed by batteries, the gas-turbine can be sized smaller. This weight reduction, however, is only apparent, as it is balanced by the presence of the generator.

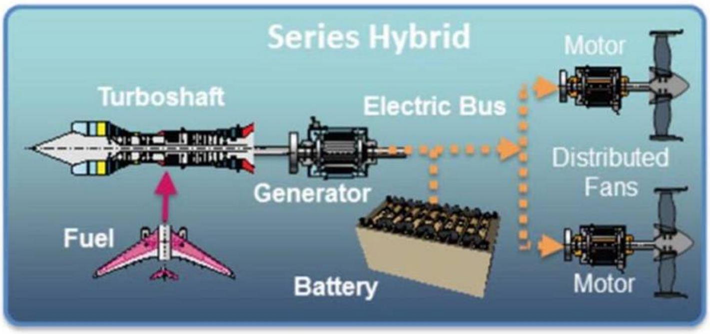

Figure 2.9. Series-hybrid architecture.

In the parallel configuration (fig.2.10), either the battery-powered motor or the turbo-engine are mounted on a shaft-driven fan, and both can provide thrust at any time. Strictly speaking, power is fed in through the low pressure spool. Also here battery packs can be recharged by the conventional engine. Compared to the series arrangements, the parallel one benefits for weight reduction due to the absence of the generator and for a higher safety redundancy level, thanks to two indipendent power-trains. The biggest drawback is the increased mechanical complexity in coupling the two lines and the significant difficulty in controlling the system, because power flow has to be regulated and blended from two different sources. Again, due to the fact that these motors are usually fed by AC-current, a power converter has to be introduced, and its weight is anything but negligible.

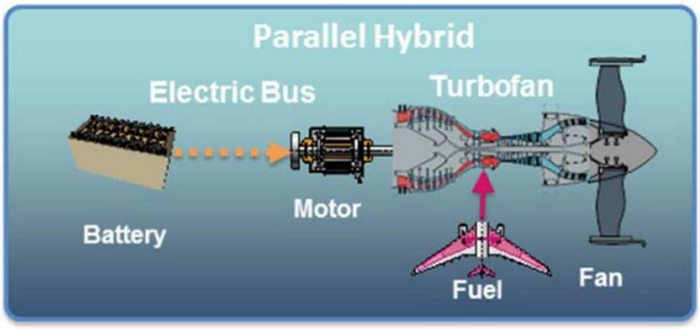

Figure 2.10. Parallel-hybrid architecture.

There are other architectures, such as the series-parallel one, which is a mixed between the twos described above, but due to their higher complexity, they are not taken into account in aircraft applications.

2.4 Degree of hybridization

Dealing with unconventional propulsion systems, with more than one power source, adds extra degrees of freedom. More specifically, it is necessary to define the amount of energy supplied by the electrical branch with respect to the one provided by the thermal plant. In order to link these with those customary used and to keep the overall number as low as possible, new design variables are introduced [7].
One key coefficient is the degree of hybridization, defined as the electric to total energy ratio.

$$H_E = \frac{E_{bat}}{E_{tot}} = \frac{E_{bat}}{E_{bat} + E_f}$$

where E_{bat} is the electrical energy and E_f is the fuel chemical energy.
The second complementary parameter is the power degree of hybridization, defined as the ratio of the electrical power to the total power supplied (electrical and thermal).

$$H_P = \frac{P_{el}}{P_{el} + P_{th}}$$

For conventional aircraft, both degrees of hybridization are zero, as all the energy/power is generated by burning kerosene: $H_E = 0$, $H_P = 0$.
For full turbo-electric architectures, all the power is provided by electric motors, driven by gas-turbine engines: $H_E = 0$, $H_P = 1$.
In the case of all-electric airplanes, $H_E = 1$ and $H_P = 1$; this means that all the energy is produced by batteries and all the power is generated by e-motors.
H_P is not a good parameter to evaluate the degree of hybridization of a predefined design. In fact, if there is a big e-motor installed, working only for a short while during the entire mission, this would result in a high degree of hybridization for power, even though only a small part of the flight envelope is "hybridized". On the other hand, also H_E can lead to oversight, because of the huge gap between the specific energy of fuel and that of batteries, other than the efficiency drop between electric systems and fuel-based turbo-machinery. This leads to low H_E values (less than 0.25), even though the total electric motor energy is higher than the total one provided by the gas-turbine.
To solve this hiccough, the supplied power ratio coefficient is added. This is defined as the ratio of the total e-motor power to the total shaft power all over the entire mission.

$$\Phi = \frac{P_{el}}{P_{shaft}}$$

$\Phi = 0$ stands for a conventional aircraft, while $\Phi = 1$ refers to an all-electric configuration.
Another variable, introduced as a power ratio, is called the split-ratio; this parameter can vary along each mission phase from zero to one, and it represents the

electric motor use in comparison to the use of the gas-turbine.

$$SR = \frac{P_{el}}{P_{shaft}}$$

As an example, a split ratio equals to 0.4 means that 40% of the power delivered to the fan comes from the electric line, whilst the remaining 60% is fed by the engine. Φ and SR actually mean the same thing; the difference is only that one takes into account the mission profile as a all, whereas the last refers to a specific phase.

In order to compare various architectures powered by different types of energy sources, a new meaningful coefficient has to be found, since the classical thrust specific fuel consuption (TSFC) is invalid. Therefore, the thrust specific power consumption [36] is introduced:

$$TSPC = \frac{P_{supply}}{T_{net}} = \frac{V_0}{\eta_g}$$

where P_{supply} is the power added to the system, T_{net} is the net thrust, V_0 is the free stream velocity and η_g the overall system efficiency.
There are other figures of merit associated with hybrid-electric propulsion, but the last one introduced in this section is the energy specific air range (ESAR) [37]. This parameter replaces the well known specific air range (SAR) and represents the change of aircraft range per change of energy in the system.

$$ESAR = \frac{dR}{dE} = \frac{V_0 \cdot \frac{L}{D}}{TSPC \cdot m_{ac} \cdot g}$$

V_0 is the air speed, $\frac{L}{D}$ is the lift-to-drag ratio, TSPC the thrust specific power consumption, m_{ac} the aircraft mass and $g = 9.805\ \frac{m}{s^2}$.

Chapter 3

Batteries

Hybrid and electric vehicles are well established in the market and are growing in popularity. Future power-trains are likely to be strongly hybridized, increasingly electrified and strictly dependent on high quality energy accumulator devices.
Same trends are kind of being taken ahold in aviation industry, focused on fuel saving and emissions' reduction. However, in this field the weight of each element is very important and can affect the entire design process. For this reason, the electrification of an aircraft is feasible if high energy density and low volume energy storage systems are available. That is why the development of batteries technology is at the hearth of this process.
Historically, only few types of accumulators were suitable for aircraft applications. Until 1950s, only vented lead-acid (VLA) one were used [38]; then, almost a decade later, they were replaced by vented nichel-cadmium (VNC) batteries, which had better performance. The silver-zink was the only other type installed on-board; having an energy density three times higher than of its "competitors", this storage unit was also attractive because of its smaller size and weight. Nevertheless, it was expensive and was characterized by poor reliability. It must be emphasized that all these elements supplied energy to aircraft systems or were used in emergency as a backup, but none of them provided traction power.
Recent technology advances have led to the development of new storage systems with higher energy density ($\simeq 200\ \frac{Wh}{Kg}$) and a relative low mass, but it seems that for aeronautical propulsive applications this is not enough ($1000\ \frac{Wh}{Kg}$ and more should be needed).

3.1 General principles

A battery is usually made of electrochemical cells connected in series, called modules; each module is, in turn, connected in parallel to form a stack. Typically a cell consists of a cathode, an anode and an electrolyte, which separates the two electrodes. Inside, an electrochemical reaction takes place, in which chemical energy is converted into electricity.

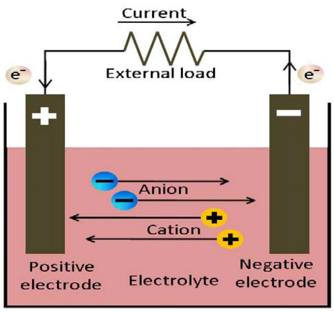

Figure 3.1. Battery working scheme [40].

During the discharge process, an oxidation reaction takes place at the anode and a reductant donates some electrons. On the other hand, i.e at the cathode, there is a reduction reaction and electrons are accepted by the oxidant element [41].

$$\begin{cases} R_1 \longrightarrow O_1 + me^- & anode \\ O_2 + ne^- \longrightarrow R_2 & cathode \end{cases}$$

Normally, the most important figures of merit for batteries are nominal voltage,

based on the number of cells connected in series, and capacity, the last depending on the number of modules in parallel, other than on operating temperature, age and rate of discharge (C-rate). 24 V is the most common voltage for lead-acid aircraft batteries as well as for nickel-cadmium one, with the difference that the first are made of 12 cells, while the second contain 19 or 20 of them.
Another key parameter is called the state of charge (SOC) and it represents the available capacity of the unit in comparison to the total one when fully charged. In dealing with aged batteries, the state-of-health is introduced to take into account the loss of capacity as time goes by. More specifically, this coefficient is defined as the percentage of the actual capacity when fully charged with respect to the rated one.

3.2 Performance comparison

There is a multitude of batteries on the market, each one suitable for a certain application and with its own limits. A way to compare the performance of such different storage systems is the Ragone plot [1], as highlighted in figure 3.2; in this chart, specific energy ($\frac{Wh}{kg}$) is plotted versus specific power ($\frac{W}{kg}$) in logarithmic scale. Simply put, the x-axis shows how much energy is available, whereas the y-axis exemplifies how much quickly energy can be delivered.

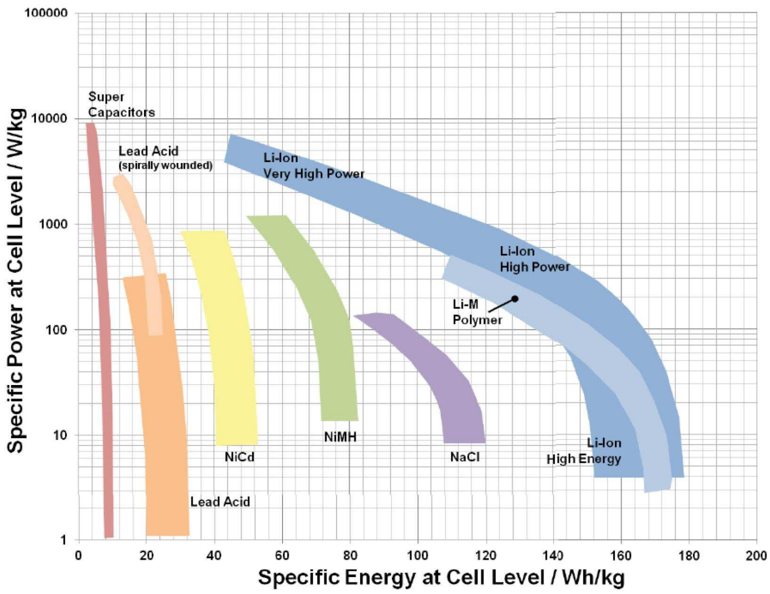

Figure 3.2. Ragone plot.

Although it can not include all the devices, such as solar cells and wind turbines, due to the difficulty in measuring energy density, and although it does not consider other important variables, like temperature operating range, cycles lifetime, self discharge and energy efficiency, this diagram is still widely adopted to develop, compare and predict batteries performance.
Looking at the figure above, it is clear that Li-ion and Li-polymer units are characterized by the highest ratios among all the technologies available on the shelf. Especially Li-ion accumulators are very "flexible", in the sense that they can both work as capacitors, in a low energy-high power mode, and as batteries, in a high energy-medium power mode. This is also due to the material utilized for the electrodes, which determines device's goodness. Actually, the anode is made of Lithium metal oxides (Manganese and Cobalt), while the cathode consists of graphite. This

combination leads to a maximum energy density of 200 $\frac{Wh}{kg}$ and specific power below 200 $\frac{W}{kg}$. Of course, these values are not adequate for aviation purposes; in order to incorporate an electric power system on-board, specific energy might raises up to 500÷600 $\frac{Wh}{kg}$ for commuter aircraft and, as stated by Boeing, up to 1000÷2000 $\frac{Wh}{kg}$ for liners.
At this point, two are the paths to undertake: try to improve actual Li-ion devices or explore new solutions, combining other materials.

3.2.1 Li-air batteries

Li-air batteries have the potential of surpass today technology, as 1000 $\frac{Wh}{kg}$ and even more can be attainable. Such a high theoretical specific energy could make long range electric vehicles widely affordable.
Between Lithium and air many possible reactions can occur, depending on the chemical environment (aqueous or non-aqueous) and mode of operation. In any case, full oxygen reduction is desired because of its greater energy density. In this way it is possible to achieve one order of magnitude higher specific energy values. For example, 3.86 $\frac{kWh}{kg}$ are reached with LiOH anode's and 5.22 $\frac{kWh}{kg}$ with Li_2O active electrode material [42]. Moreover, the advantage of Li-air cells from a specific energy point of view is more dramatic than from an energy density point of view, because of the relatively low density of Li-air cathode active material.
However, there are many issues applicable to these systems, like partially irreversible reactions, Li stabilization at the cathode, precipitation and dissolution of the discharge products (this is the case of aqueous electrolyte) and Oxygen contaminants.
Apart from these points, Li-air storage units remain one of the few and most promising solutions to the daunting challenge of low-cost and high-range electro-mobility.

3.2.2 Li-O_2 and Li-S batteries

These are two formidable challenges to go beyond Li-ion batteries. Both has been investigated since 1940s; significant advances have been made in the last 70 years, but the main factor limiting practical energy storage is the need of excess Lithium in the anode. To overcome this boundary, replacing the electrode or improving its efficiency are some ideas to consider [43].
In great detail, $Li-O_2$ batteries can have a aqueous or non-aqueous electrolyte. In both cases, the anode is oxidized and releases Li^+ ions. At the positive electrode, O_2 from the atmosphere dissolves into the electrolyte and it is reduced. As the cathode is exposed to ambient air, it is tainted by carbon dioxide and water, which severely affect chemical reactions. For this reason, it is mandatory to remove these gases, for example by adding a membrane. Another aspect that deserves attention is the type of electrolyte in play: this is a key component as it has to be stable with

Oxygen and Li compounds, having sufficient Li^+ conductivity and O_2 solubility. Suitable elements can be organic carbonate, or even better, ethers.
On the other hand, Li-S batteries operate by reduction of Sulphur at the cathode. This reaction results in the formation of poly-sulphides, that combine with Li to produce Li_2S. These cells are characterized by a high theoretical energy density and are attractive because of S abundance and low cost. However, they are affected by lots of problems, among them a limited rate capacity and a fast capacity fading due to the formation of many intermediate compounds.
Even if Li-O_2 and Li-S devices look like different, they have some points in common; one of them is the issue related to the positive electrode, which determines electrons transport, and thus efficiency. Another is their superiority in specific energy in comparison to Li-ion batteries, as reported in the following table [43]; to be more precise, Li-O_2 one show higher specific energy than Li-S.

Battery	Cell voltage (V)	Theoretical specific energy $\left(\frac{Wh}{kg}\right)$
Li-ion	3.8	387
Li-S	2.2	2567
Li-O_2 (non aqueous)	3	3505
Li-O_2 (aqueous)	3.2	3582

Table 3.2. Batteries data.

The third point is related to cost-effectiveness: Sulfur is cheap and Oxygen is free and, as a consequence, the price per cell is lower than the Li-ion one.
No one knows if these storage systems will become commercially usable; the only guaranty is that our society needs higher energy level accumulators, and Li-O_2 and Li-S are among the two major contenders.
There are also many studies on this topic involving the use of new materials, in order to combine different positive and negative electrodes in such a way as to increase both energy and power density (fig.3.3).

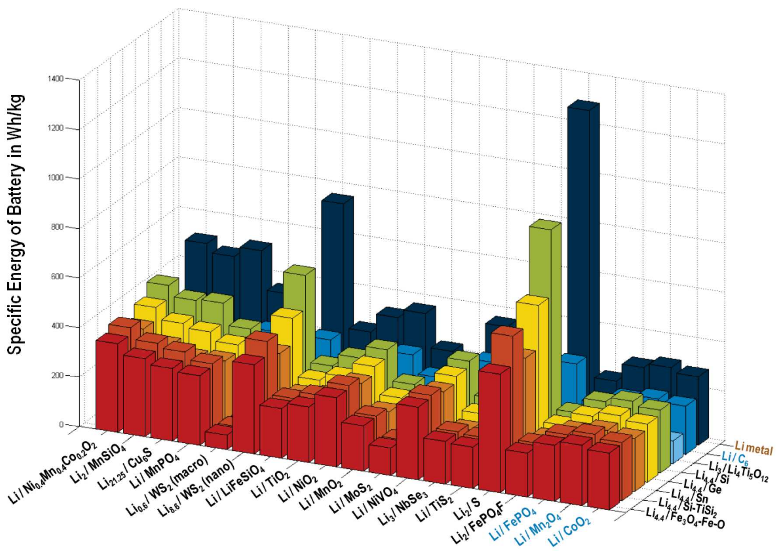

Figure 3.3. Batteries specific-energy with different electrode materials [2].

3.3 Modelling approaches

There are different strategies to modelling energy storage systems and their non-linearities. All the methods can be grouped in three main categories: electrochemical models, electrical equivalent circuit methods and mathematical approaches. In literature it is also possible to find a mixture of the aforesaid ones, in combination with thermal models.

3.3.1 Electrochemical models

These models are based on the electrochemical processes that take place inside the battery and can provide full information of the internal chemistry. Thanks to this peculiarity, they are considered the most detailed one. However, such a degree of accuracy lead to a higher complexity and difficulty in implementation.
Usually, they are based on a set of partial differential equations, which try to describe potential generation's and how this is affected by chemical reactions. Ohm's law is used to calculate the potential, while Fick's law predicts elements' concentration at the electrodes.
Electrochemical methods can be coupled with thermal one to give high order details, but at this point, without any simplification, the solution is obtained only by means of computational tools [41].

3.3.2 Electrical circuit models

The intricacy of the aforementioned approach and past computing limitations led researchers to find another way to predict storage systems behaviour, so as to balance complexity and accuracy. As the name allows to think, these new models represent accumulators' dynamic and non-linear attitudes with an equivalent electrical circuit. Whatever the battery, the core elements, in broad terms, are the same:

- one or more resistors representing battery losses.
- a capacitor, simulating the capacity of storing energy.
- a voltage source, representing the open-circuit voltage.

IR model

The simplest equivalent circuit model is reported in the figure below. It consists of a voltage source, representing the open-circuit voltage of the battery (or ideal voltage) and a resistance, which symbolizes internal ohmic losses. Both variables are function of the state of charge (SOC) of the device, other than of the operating temperature. The actual voltage is given by:

$$V = V_0 - R \cdot i$$

where V is the voltage and "i" is the current flowing out of the system.

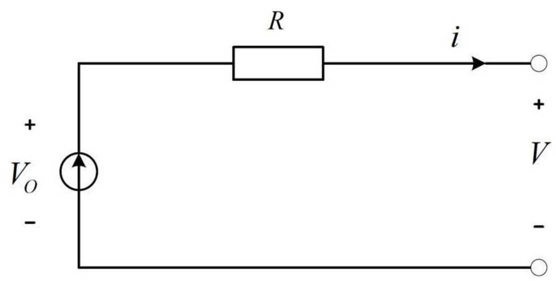

Figure 3.4. RC-circuit battery model [44].

Being a steady-state model, it is not able either to represent transients either to give a dynamical evaluation of the SOC trend.

OTC model

A more detailed model (fig.3.5) can be built up adding a RC network in series to the internal resistance. The capacitor acts like a "plenum volume" and it takes

into account battery transients. In addition, the parallel configuration between the resistance and the capacitor allows a more detailed description of the discharge process.
The following equation describes circuit behaviour:

$$V = V_0 - V_{RC} - R \cdot i$$

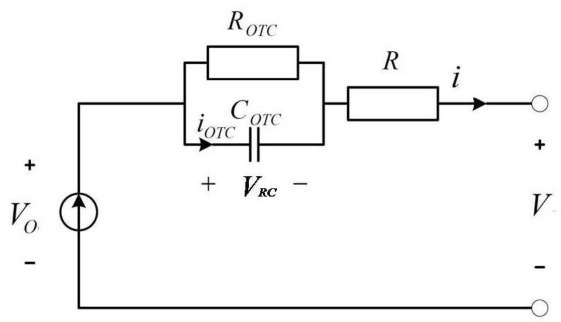

Figure 3.5. OTC-circuit battery model [44].

TTC model

Experiments showed that batteries behave differently during short and long transients. Because of this, an additional RC network is added in series to the OTC model; in this way, the first parallel group, made of a resistance plus a capacitance, tries to reproduce short-term characteristics, whereas the second is associated with the long-term dynamics.
Figure 3.6 depicts TTC's circuit network, which can be described by the following relation:

$$V = V_0 - V_{RC_1} - V_{RC_2} - R \cdot i$$

V_0 is the ideal voltage, V_{RC_1} and V_{RC_2} are the voltages across the capacitors, R the ohmic internal resistance and "i" the battery output current.

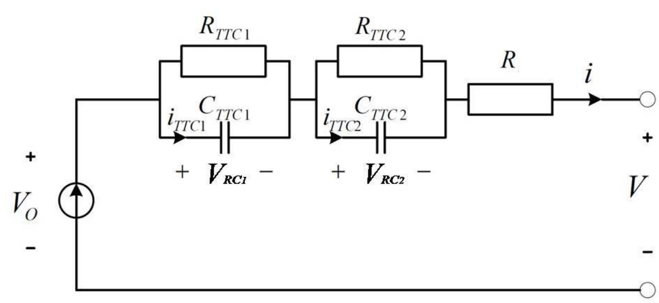

Figure 3.6. TTC-circuit battery model [44].

3.3.3 Mathematical models

This group can still be split in analytical and stochastic methods. Different physical concepts are used, concurrently with an higher level of abstraction, if compared to the previous models. In general, few equations are introduced to describe battery properties.

Analytical model

The kinetic battery model is an example of such approach and is the most used. Storage systems are modelled as two tanks: the "available-charge well", which supplies electrons directly to the load, and the "bound-charge well", which provides charge to the previous one. The electrical flow rate depends upon the different liquid level in both tanks and the valve installed in between.

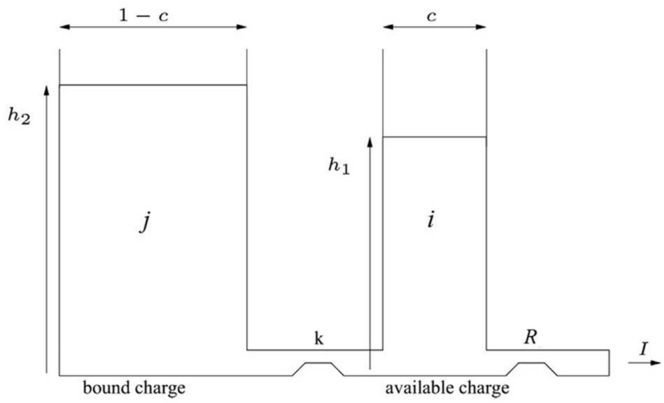

Figure 3.7. Kinetic battery model [45].

All the parameters needed to completely define the model are given in the figure above and are listed hereafter.

- c gives the fraction of total charge.
- h_i represents the battery SOC.
- R is the internal resistance.
- k is the valve coefficient.
- I is the output current flow.

The following system of differential equations describes the change of charge in each well.

$$\begin{cases} i = h_1 \cdot c \\ j = h_2 \cdot (1-c) \\ \frac{di}{dt} = -I + k\,(h_2 - h_1) \\ \frac{dj}{dt} = -k\,(h_2 - h_1) \end{cases}$$

When a load is applied, the "available-charge tank" begins to loosen up (h_1 decreases), and the difference in height between the two wells causes a flow until $h_2 = h_1$ (principle of communicating vessels). In this way, the recovery effect is considered too.
The KiBaM was developed for large lead-acid storage devices, which have a quite flat discharge profile and, as a consequence, it does not hold for modern Li-ion units, unless than for lifetime behaviour inspections.

Stochastic models

They describe batteries in an abstracted manner and are based on Markov chain, i.e a memoryless process in which one can predict future evolutions without knowing the full history. In other words, starting from the present state, it is possible to model a random system able to foresee incoming events.
The first stochastic model was developed by Chiasserini and Rao (see fig.3.8) [41]. In this, batteries are described by a discrete time Markov chain with N+1 states, ranging from 0 to N. Each state number corresponds to a charge unit included in the storage system. Every time step, a charge unit can be consumed, with a probability $a_1 = q$, or recovered, with a probability of $a_0 = 1 - q$. The battery is emptied when the 0 state is reached or when a maximum of T charge units have been utilized. One aspect that deserves attention is that there is a non-zero probability of staying in the same state; this means that no consumption or recovery takes place at each time step, and this leads to a more suitable representation of "idle periods".

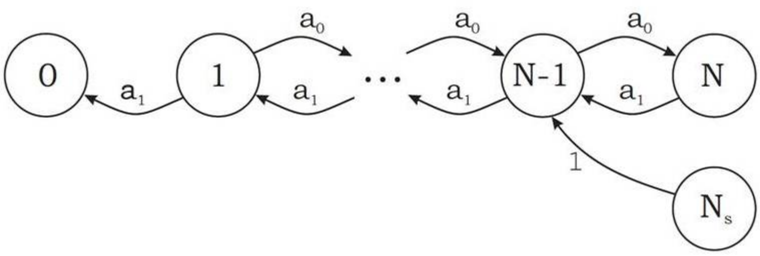

Figure 3.8. Basic stochastic battery model.

Chapter 4

Power converter

Also known as inverter, this electrical device aims at changing direct current (DC) into alternating current (AC), or vice-versa, depending on the application. It should be noted that it does not produce any power, which is typically supplied by a source placed upstream, like a battery pack or a generator.
The earliest AC power converters were electro-mechanical devices. Direct current flew from one end of the circuit to an electromagnet. This activated itself, and in turn pulled a wire attached to a spring arm, forcing it to contact the circuit. This changed the current flow to the other side of the circuit, cutting power from the electromagnet. As soon as the magnet was released, the spring snapped the wire back, allowing the current to flow backward, once again activating the magnet.
An example of this early technology is the rotary converter (fig.4.1), an electrical machine which acts as a rectifier, an inverter and as a frequency converter too. It can be think as a motor-generator combination, sharing the same rotating armature, and it can work in a direct or reversed mode, depending on the output needed (DC or AC respectively).

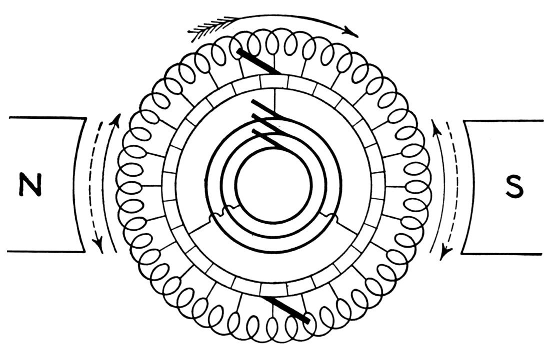

Figure 4.1. Rotary converter sketch.

However, modern solid-state inverters use oscillator circuits to accomplish the same process, so there is no longer the need for a spring arm flipping back and forth to alternate the current. The main elements embedded in are transistors (IGBT) and diodes, which can be grouped and connected in series and/or in parallel, according to operating voltage, current and redundancy aspects. In reality, things are more complicated. Alternating current forms a sine wave, while power converter output is a square one. Thus, to cleaning up the wave requires a series of filters, inductors and capacitors. In addition, when connected to an electric motor, inverter circuitry can be designed to produce a variable output frequency range, in order to control its speed.

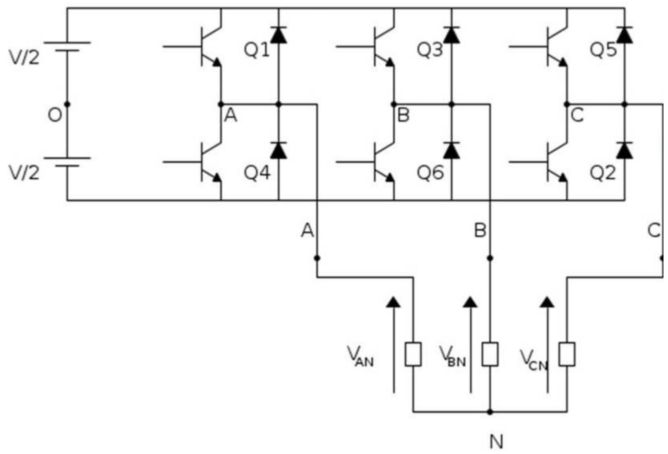

Figure 4.2. Generic three-phase DC-AC inverter sketch.

Going back to the electrical components, there is to say that there are different types of switching elements available on the market, each with its own characteristics (table 4.2). For example, Metal-Oxide Semiconductor Field Effect Transistors (MOSFET) have an high frequency switching mode, but at relative low power, while thyristors are able to switch at low frequency, but at higher power. Finally, Insulated Gate Bipolar Transistors (IGBT) are somewhere between the twos and for aircraft power and frequency range they seem to be the best choice.

	Current	Max. voltage	Frequency
MOSFET	0-250 A	1 kV	0-1 MHz
Trystors	0-2500 A	5 kV	<1 kHz
IGBT	0-2000 A	4 kV	1-10 kHz

Table 4.2. Switching components [5].

During the conversion process, there are usually two type of losses, relating both to IGBTs and diodes: switching and conduction one. Because of these phenomena, one must keep in mind that power converter generates a great amount of heat and therefore, to conduct it away, heat-sinks, like a metal "fin-casing" or a coolant fan, are essentials.
Looking to aviation purposes, inverters are usually set among a battery pack or a generator, and a motor. This last can even be directly connected to its power source by an AC or DC transmission line. This configuration forces both components to be locked in the same shaft speed ratio, thing that took the number of poles of each machine to be carefully chosen. On the other hand, interposing a power converter to drive the motor, disables all these restrictions; both are untied and can operate at whatever speed (always remaining within physical limits) [21].
Including this device in the power line does not raise losses significantly, unless managing very high power. A commercial solid-state inverter has more or less a power density of 0.2÷0.5 $\frac{kW}{kg}$, but some types can reach 0.9÷1.05 $\frac{kW}{kg}$ [76] and 95% efficiency, which can be improved by paralleling more transistors, at the expense of a higher weight. Recent technology based on Silicum-Carbide (SiC) raised these values up to 5,79÷6.45 $\frac{kW}{kg}$. 98% efficiency and 8÷10 $\frac{kW}{kg}$ power density can be achieved by means of superconducting materials working at cryogenic temperatures.

Chapter 5

Motors

This section deals with electrical machines, i.e devices able to convert electric energy into mechanical one and vice-versa. The first function is performed by motors, the second by generators. Anyway, most of these apparatus can perform both operations by reversing energy flow, i.e a motor can be used as a generator an the other way around.

5.1 General aspects

An electric motor is made of a fixed part, called stator, and a rotating one, the rotor, through which is possible to connect the machine to an external load. Torque is transmitted by a shaft, which is sustained by bearings, in order to rotate freely. Between the stator and the rotor there is a mechanically imposed air gap, necessary for the rotating parts to move. However, this small empty-space has some impacts on electromagnetic performance.

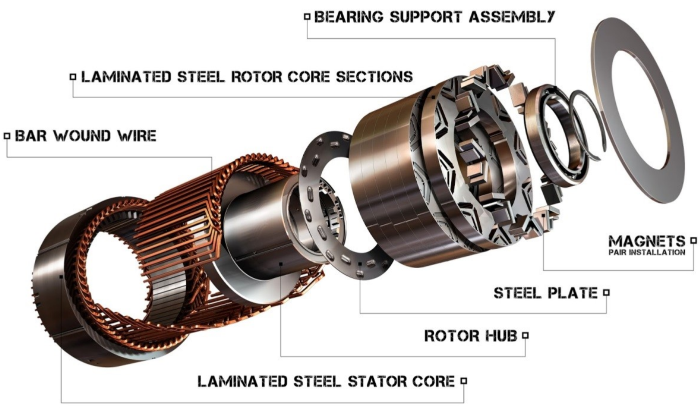

Figure 5.1. Electric motor breakdown [66].

Depending on the type of system, lighting conductors are housed in the stator or in the rotor (or in both parts), inside grooves, whose purpose is to hold coils and their insulating stuff. Current is fed inside these conductors, magnetic fields are generated and interact with each other to produce the required torque. In order to intensify the effect, rotor and stator are usually made of iron.
Talking about coils, it is appropriate to distinguished of two types: the drive coils (or excitation coils), which main purpose is to generate a magnetic field, and the armature coil [14]. The current amplitude on this is strictly related to the external load, and it increases in line with the power needed. In permanent magnet machines, on the other hand, there is no need of excitation coils as magnetic field is developed by magnets (hence the name).
Electric motors can be fed from direct or alternating current sources. AC-motors can be single-phase, three-phases or even more and can be catalogued as synchronous and asynchronous. For aviation purposes, permanent magnet synchronous machines seems to be the most suitable, as they combine good performance, reliability, low mass and high efficiency. The only drawback is magnets' cost, as they are made of rare-earth material, such as Neodymium-Iron-Boron (NdFeB).
In addition, if dealing with turbo-electric propulsion, the choice of AC rely on its availability: in fact, it is directly produced by engine-driven generators. There are other advantages in using AC machines instead of DC ones. The first are very rugged and have high expectancy life, but the main difference is the speed control: a D.C. motor speed is controlled by varying armature current while the A.C. one is controlled by changing frequency, which is commonly performed by a PMAD unit. Now, if the current to hand in a DC system is quite high, a further increment in it would result in additional losses and electro-mechanical stresses. These are some of the main reasons why AC motors are preferred, even if the power source is in DC, and so a power converter is mandatory.

5.1.1 Types of losses

Converting electrical energy into mechanical one inevitably results in some kind of losses, as the process that takes place is not 100% efficient. Depending on powers into play, a certain amount of heat is produced, thus the need to cooling the system with forced air or liquid hydrogen, the last if dealing with superconducting technologies.
There are two main group of losses in electric motors: iron losses and copper losses [14]. Concerning the first, these can be further divided in two classes, namely eddy-current and hysteresis losses. The latter occur when switching the electromagnets on and off and are function of the material's magnetic properties. Special materials have been developed to limit them, such as some steels with a high silicon content, but they are disadvantaged by having a low saturation flux density. This essentially means that a big, heavy stator is needed to achieve the same magnetic field.

Moreover, eddy current losses depend on many variables, like the stator's lamination thickness, the operational frequency, the flux density and material's resistivity. On the other hand, copper losses are generally the most significant. Being proportional to Ri^2, these losses are primarily due to the resistance of copper conductors when carrying tide. Of course, because copper is heavy, it is desirable to use as few as possible, minimising cross-sectional area. Unfortunately, this increases resistance, therefore losses and heating.
Till now, the discussion focused on electrical losses, but it is appropriate to take into account also the mechanical ones. In this case, two are the categories: friction losses, caused by bearings and lubrication, and windage losses, which combine drag losses from the rotor spinning in air and those coming from the fans used to cool the unit.
The following figure highlight a losses breakdown for conventional electric motors.

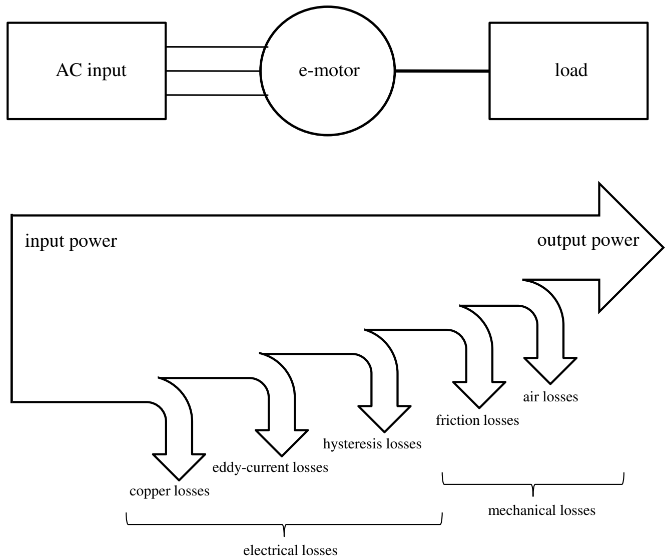

Figure 5.2. Electrical motor losses breakdown.

Furthermore, stray-load losses are also present and are an irritating parameter for designers, mainly because it is difficult to determine their impact accurately. They are generated by short circuit currents in coils under commutation, eddy currents in bolts and other solid parts of the armature, flux distorsions and pulsations caused by changes in magnetic reluctance. Someone encompasses in this category also the losses due to eddy currents in armature conductors.
Typical losses for a low power AC-machine are reported in the table below [49].

Stator resistance losses	30%
Rotor resistance losses	20%
Core losses	19%
Friction and windage losses	13%
Stray load losses	18%

Table 5.2. Typical losses for low power e-motors.

Applying this technology to an aircraft propulsive drive-train leads to cope with several challenges, among them those of weight and power density. Conventional motors have a power to weight ratio of about 3 $\frac{kW}{kg}$, unsuitable for the electrification of passenger transport airplanes. In addition, they might be reliable and safe, extremely efficient and light. The induction motor SP260D, made by Siemens, is such an example; having a power-density of 5 $\frac{kW}{kg}$, a maximum power of 260 kW and less than 50 kg weight, it is considered one of the strongest conventional system ever built. However, even if it is a good solution for general aviation and commuters, this is not for the "flying bisons", which power request overtakes the MW class.
Thus, to built more "eco-friendly" aircraft, in order to meet 2035 and 2050 emissions targets, a new technology is needed, i.e that of superconductors.

5.2 Superconduction

In 1911, in the course of very low temperature experiments, the Dutch physicist Heike Kamerlingh Onnes discovered that below 4.2 K Mercury resistance fell to zero. This is the quantum-mechanical phenomenon of superconductivity.
In general, when reaching the so-called "critical temperature" (T_c), materials undergo transition and become superconductors. This state is characterized by lack of resistance to current carriage and by magnetic field expulsion (it does not penetrate the material); this last is known as Meissner effect [16]. T_c is different for each material (see table 5.4) and strictly depends on its properties and its crystalline structure.

Element	T_c [K]	Element	T_c [K]
Al	1.19	Nb	9.2
Hg	4.15	Pb	7.2
Mo	0.92	Ta	4.39
Ti	0.39	U	0.2
Zn	0.9	V	5.3
Compound	T_c [K]	Compound	T_c [K]
MgB_2 [1]	39	Nb_3Sn [2]	18.1
YPd_2B_2C [3]	23	$PbMo_6S_8$ [4]	15

Table 5.4. Critical temperature for some superconductors [17].

The superconducting state is not completely stable, and can be disrupt by an abrupt change in temperature or by a magnetic field variation, which in turn penetrates inside the material, stopping Meissner effect. However, not all elements and compounds react in the same way when these modifications take place; for this reason it is custom to distinguish two groups of superconductors:

- Type I stand in superconduction only until the magnetic field applied is relatively weak. Above a specified threshold, they fall down to the normal resistive state.
- Type II, instead, preserve their superconductive state with strong magnetic fields and with local penetrations too. This behaviour enable them to work properly, even if mixed superconduction and non-supercondution areas exist in peripheral zones.

A big step forward has been made with the development of high-temperature superconducting compound (table 5.6). A discovery as significant as this is going to

[-3] Magnesium diboride

[-2] Triniobium-tin

[-1] Intermetallic Boron carbide

[0] Chevrel phase

[1] Magnesium diboride

[2] Triniobium-tin

[3] Intermetallic Boron carbide

[4] Chevrel phase

revolutionize transports, power transmission and storage systems. Although 135 K critical temperature has been reached, it does not yet bear any comparison with room temperature and a cryo-cooling system is still needed; liquid Nitrogen (boiling point at 77 K) or LH_2 (boiling point at 20 K) can be used instead of the expensive Helium.

High T_c superconductors	T_c [K]
$YBa_2Cu_3O_7$ [5]	93
$Tl_2Ba_2Ca_2Cu_3O_{10}$	125
$HgBa_2Ca_2Cu_3O_8$	135

Table 5.6. Some high-temperature superconductors [17].

Concerning aircraft applications, this is a big impediment, as cryo-coolers are bulky and heavy and can dramatically limit operative range and possible fuel saving coming from the introduction of hybrid or full-electric propulsion systems. Figure 5.3 gives an overview on state-of-the-art cooling technology; one can see that for high power demands, weight becomes a formidable challenge. One possible solution could be that of replacing these machines with something lighter; for this purpose, liquid Hydrogen could take the place and could be utilized as for cooling HTS components either as fuel, in addition to kerosene, since it has a lower heating value (LHV) of almost 120 $\frac{MJ}{kg}$.
However, there are obviously many drawbacks: storage tank volume and installation, insulation and safety.

[4] Yttrium-Barium-Copper-Oxide

[5] Yttrium-Barium-Copper-Oxide

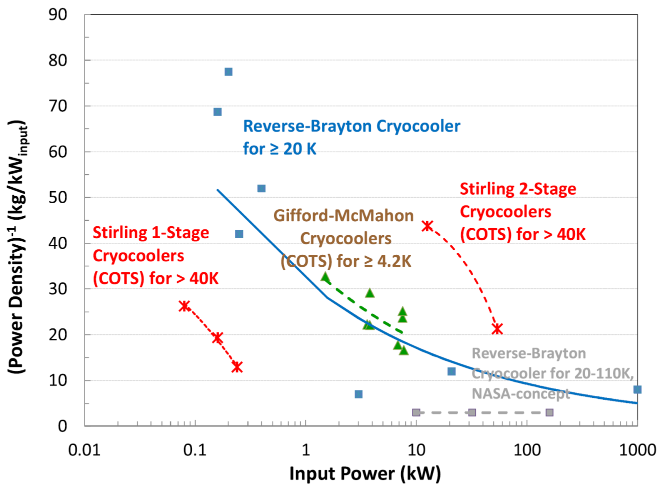

Figure 5.3. Cryo-coolers power density [18].

5.2.1 HTS conductors

Unlike their cylindrical copper counterpart, HTS conductors typically have a thin tape form, they are designed to carry high current density and to hold more than 2 T magnetic field intensity. This geometry allows them to be wrapped around small diameter rotor, forming a high density coil. Initially, BSCCO [6] compound was used, which consists of a set of multi-filaments enclosed in an Ag-allow matrix. Better performance can be achieved with recent development, such as the YBCO HTS conductor material. Its structure is reported in the figure below [18]. Starting from the bottom, a metal lamina is used as substrate, on which a buffer and a superconducting layer are deposited. Then, to protect the last from the environment, a thin silver shield is applied. In the end, another coating made of copper is added to provide tied isolation and minimize core contamination risks.

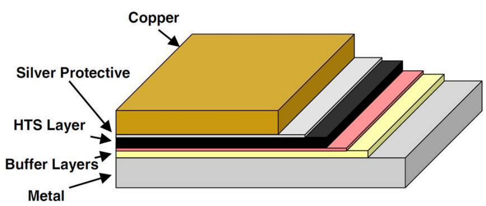

Figure 5.4. YBCO conductor architecture.

[6]Bismuth-Strontium-Calcium-Copper-Oxide

5.2.2 HTS motors

Power requirements for small to medium size passengers aircraft range from 2 MW to 50 MW. Delivering this amount of energy by conventional electrical systems seems prohibitive, since motors and generators would suffer from a sharply weight rising, along with losses associated to copper conductors. This would lead to wipe out any benefits in terms of efficiency and fuel consumption. HTS devices and distributed propulsion integration are the way out. A superconducting system would allow extremely low losses and thus higher efficiencies, theoretically beyond 99%. With respect to copper buses, higher currents can flow, decreasing voltage, which in turn lead to low insulating cables' material.
Superconducting motors and generators are characterized by having almost one third of the overall volume of their conventional equivalents and half of their mass; power density can be in the order of $20 \div 40 \frac{kW}{kg}$. Furthermore, because the magnetic field transported in wires is stronger, less or no iron is needed on the rotor; as a consequence, losses are reduced, and mass too.
In the following figure [62] a comparison between conventional and HTS generators is made. One can observe the substantial difference in weight, especially when moving to huge output torque, which is directly proportional to power through angular velocity.

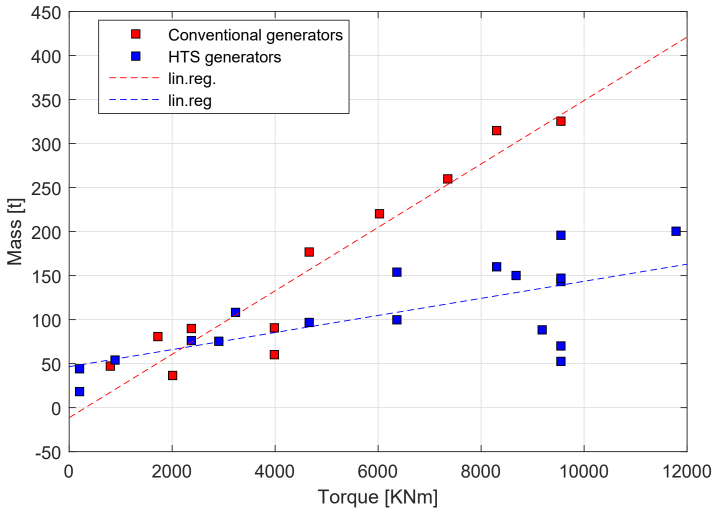

Figure 5.5. Weight vs. torque comparison between generators.

HTS motors can be divided in two classes: the hybrid configuration (fig.5.6) [59] and the all-cryogenic one. The first is a conventional design exploited up to date, in which only rotor windings are made of superconducting materials. Stator windings are made of copper, as conventional machines, except for iron, which has been removed. However, some issues arise in isolating the superconducting core from room temperature stator.

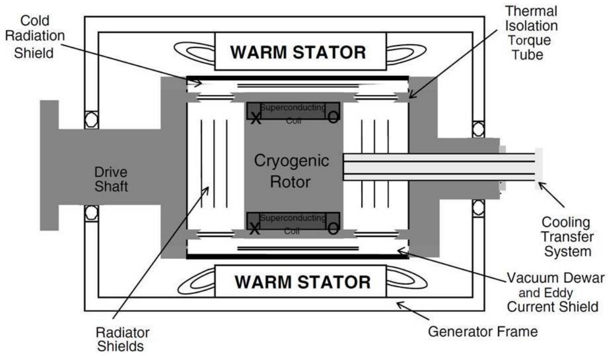

Figure 5.6. Partial-HTS motor scheme.

The other class refers to fully superconducting machines. Here, both rotor and stator coils are made of YBCO compound or alike and all the apparatus is enclosed in a cryogenic casing.
Due to the rotating magnetic field, a percentage of AC armature losses is still there, even if lower than their Cu-based counterpart. These inefficiencies include eddy-currents, coupling currents and metal effect losses, and can be minimized only with the development of AC-tolerant conductors. Until then, despite the fact that an all-cryogenic architecture is the lightest, simplest and most reliable design option, partial superconducting systems will be the workhorse for future power-trains.

Chapter 6

Electrical components design approach

After a brief discussion on state-of-the-art and future advanced technology aviation electrical tools, a design method to model the main components is outlined herein. By referencing to existing technical literature, a battery model is implemented, along with a power converter and a motor/generator ones.

6.1 Battery modelling

In this section, a Li-ion battery model taken from [8] is explained. Taking into account discharge characteristics, this model aims at determining storage system mass and capacity to fly a specified mission and it can be applied in preliminary design processes.
To predict these quantities, aircraft power profile, i.e subsystems and electric motor shaft power demand, is generally needed. Then, it is possible to proceed with batteries sizing, focusing the attention on the state-of-charge (SOC) parameter, a figure of merit indicating how much energy is still available. If it goes below a default value (typically 20%), electrodes can be permanently damaged, while if it is above a predefined threshold, the battery is oversized.
As stated in the previous chapters, a battery cell is characterized by its nominal capacity C_{nom} and voltage V_{nom}, and it is made of three main elements: an anode, a cathode and an electrolyte. Its discharge behaviour is strictly non-linear, as it depends on the actual SOC and on the C-rate coefficient, which is a measure of the discharge velocity of the battery with respect to its maximum capacity [67]. Batteries performance are also influenced by temperature, but this effect is not considered here; the assumption of constant working temperature is made.

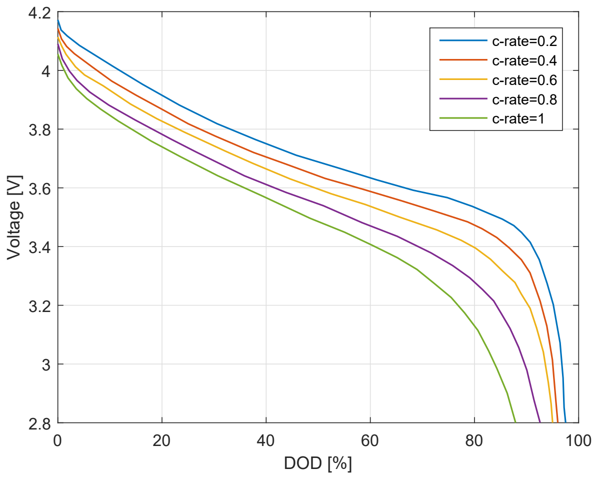

Figure 6.1. Li-ion discharge curve at different C-rate [69].

One more digit that needs to be considered is the cut-off voltage, which represents the minimum cell voltage below which the device is considered empty. Usually this value is given by the manufacturer. Again, given the C-rate, this threshold value defines the maximum discharge capacity of the battery, also known as depth of discharge (DOD) (fig.6.1).

6.1.1 Equivalent electric circuit

In order to model battery cells' discharge behaviour, an equivalent electric circuit is considered (fig.6.2).

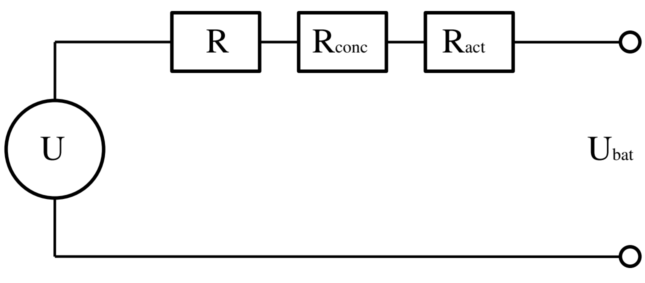

Figure 6.2. Battery equivalent electric circuit.

Each impedance is a function of the state-of-charge and symbolizes losses associated to an electrochemical process. Starting from the left hand side, the first resistance represents ohmic losses (R), the second concentration losses (R_{conc}) and the third activation ones (R_{act}). U is the open-circuit voltage, whereas U_{bat} is the effective battery cell output voltage, which is obtained as follows.

$$U_{bat} = U - (R + R_{conc} + R_{act}) \cdot i \tag{6.1}$$

where, in accordance with [68]:

$$U = -1.031 \cdot e^{-35 \cdot SOC} + 0.321 \cdot SOC^3 - 0.1178 \cdot SOC^2 + 0.2156 \cdot SOC + 3.685 \tag{6.2}$$

$$R = 0.1562 \cdot e^{-24.37 \cdot SOC} + 0.07446 \tag{6.3}$$

$$R_{conc} = 6.6030 \cdot e^{-155.2 \cdot SOC} + 0.04984 \tag{6.4}$$

$$R_{act} = 0.3208 \cdot e^{-29.14 \cdot SOC} + 0.04669 \tag{6.5}$$

When discharging a battery, voltage decreases with time, as well as the output power. From Ohm's law, current is calculated.

$$i = \frac{P_{bat}}{U_{bat}} \tag{6.6}$$

Given the nominal capacity of the battery C_{nom}, which is usually defined at a discharge rate of $\frac{C}{5} = 0.2$, the instantaneous C_{rate} can be determined:

$$C_{rate} = \frac{i}{C_{nom}} \tag{6.7}$$

Now, since the capacity is influenced by this parameter, the same can be used in conjunction with diagram 6.3 to obtain the relative available capacity r_c of the storage system. As fast the discharge rate, as fast the capacity decreases.

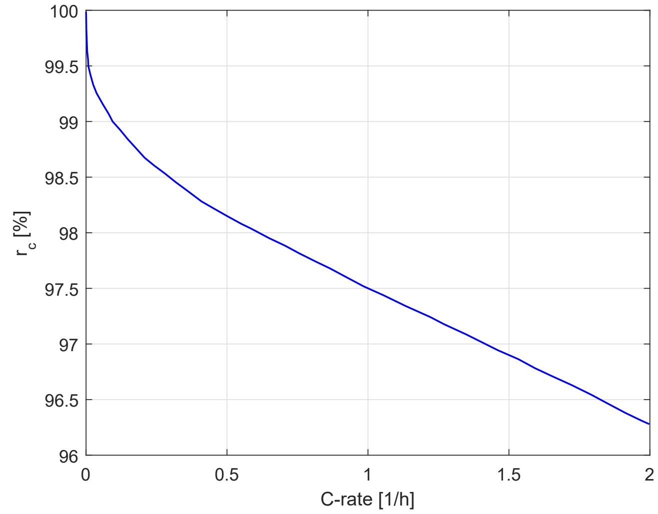

Figure 6.3. Available battery capacity [8].

As a consequence, the actual available capacity diminishes:

$$C_{act} = r_c \cdot C_{nom} \tag{6.8}$$

With time running out, all the coefficients calculated till now varies, and the battery drains, thereby dropping SOC for each time step dt.

$$SOC = SOC_{t=0} - \int_0^{t_{max}} \frac{i(t)}{C_{act}(t)} dt \tag{6.9}$$

$SOC_{t=0}$ is the state-of-charge at the beginning of the mission, and if the unit is fully charged, it equals 1.
The depth-of-discharge (DOD), i.e the percentage of battery capacity that has been discharged, can also be introduced. Basically, it is defined as the one's complement of the SOC.

$$DOD = 1 - SOC \tag{6.10}$$

Finally, the cell efficiency can be calculated with the following equation:

$$\eta_{bat} = 1 - \frac{R_{tot} \cdot i^2}{U \cdot i} \tag{6.11}$$

In the expression, R_{tot} refers to the sum of all the equivalent circuit losses $(R + R_{conc} + R_{act})$.

6.1.2 Battery pack

More cells can be connected in series and in parallel to build a battery pack (fig.6.4). The number of cells in series form a module and determine the total voltage, while the number of modules connected in parallel define the device's capacity. In this way, a module has to handle only a fraction of the total power required to the battery pack, as spelt out in the following relation.

$$P_{bat} = \frac{P_{req}}{n_{pack} \cdot m \cdot \eta_{sys}} \tag{6.12}$$

P_{bat} is the power a module has to handle, P_{req} is the total power demand and is the sum of the shaft power P_{shaft} plus the power off-takes $P_{off-takes}$ absorbed by secondary electrical systems. n_{pack} is the number of battery packs installed, m is the amount of modules per pack and η_{sys} the overall transmission efficiency, from the source to the final load.
Furthermore, once the total capacity is known from the power profile, battery weight can be calculated with reference to next equation.

$$W_{tot} = \frac{C_{tot}}{\rho_{bat}} \cdot k_{add} \tag{6.13}$$

C_{tot} is the overall capacity required, ρ_{bat} is the specific energy $\left(\frac{Wh}{kg}\right)$ and $k_{add} = 1.15$ a factor taking into account casing and cables' mass.

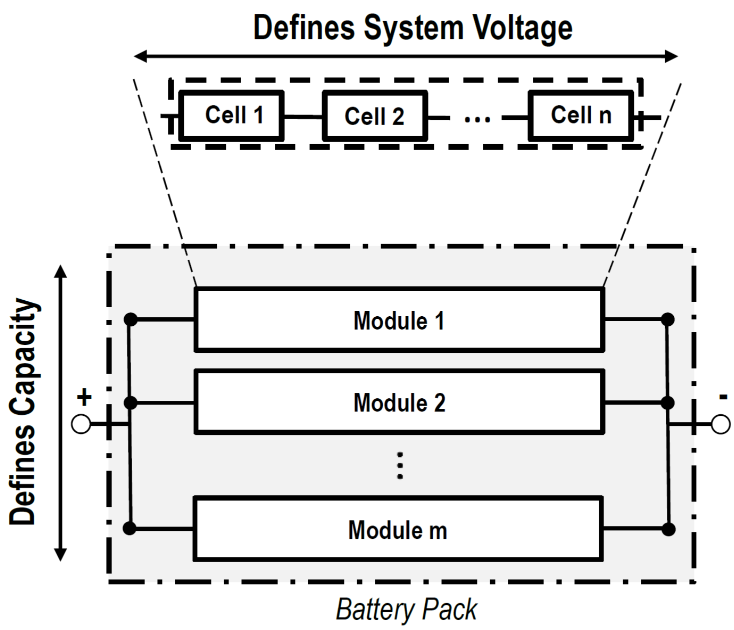

Figure 6.4. Battery pack sketch [8].

6.1.3 Flowchart

The sizing procedure is set up in the block diagram of figure 6.5 [8]. In order to determine the battery SOC and other useful parameters, an iteration process is needed.
Above all, the power requirements for each time step $P_{req}(t)$, the cell nominal capacity C_{nom} and voltage U_{nom}, and the initial state of charge have to be known. After that, a first voltage estimation of a battery module can be done by multiplying the nominal cell voltage times the number of elements n connected in series. Being the modules arranged in parallel, this is also the overall system voltage.

$$U_{mod} = U_{sys} = U_{nom} \cdot n \tag{6.14}$$

At this point, module discharge current and C-rate can be calculated with equations 6.6 and 6.7.

$$I = \frac{P_{bat}(t)}{U_{mod}} \tag{6.15}$$

where P_{bat} is determined according to equation 6.12.

$$C_{rate} = \frac{I}{C_{nom}} \tag{6.16}$$

As modules are connected in parallel, the pack total output current is given by the summation among all the modules $\sum_{i=1}^{m} I(m)$.
With these values at hand, the actual cell voltage is determined through the equivalent circuit equations 6.1. After that, a new estimation of the system voltage is performed (eq.6.14), along with the calculation of the new output power.

$$P_{bat_{new}} = U_{sys} \cdot I \tag{6.17}$$

The process can now restart from the beginning and the iteration ends when the battery output power convergence is reached. From equation 6.11, efficiency is determined.
The sizing process proceeds with the comparison between the cell voltage and the cut-off voltage. If the first is smaller, the iteration stops because the capacity is too low, and it is necessary to increment it adding new modules. On the other hand, if the cut-off voltage is not reach, the time step is increased and the available capacity and the SOC is determined. A last check should be done in order to avoid SOC to fall below 20%, so as not to damage the storage system.

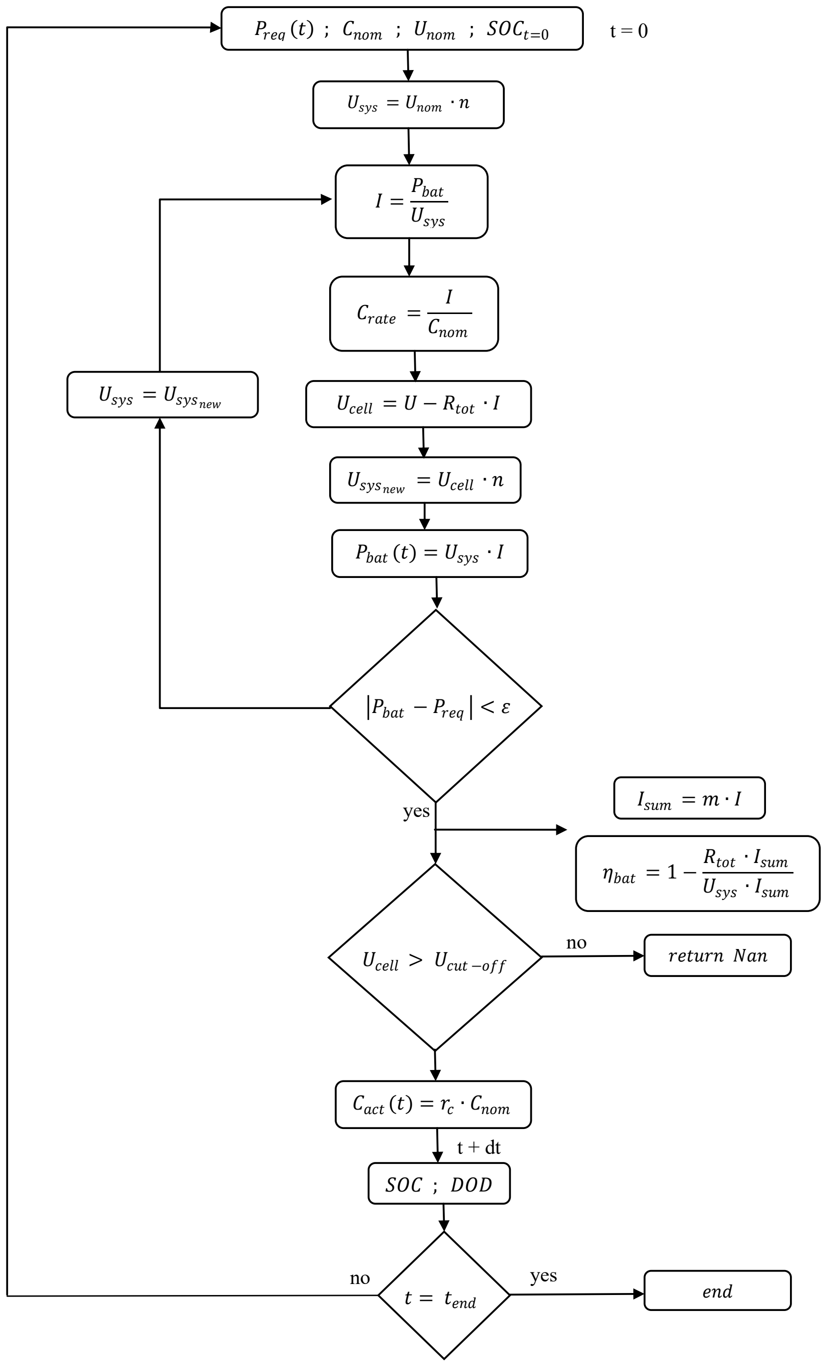

Figure 6.5. Battery model flow chart.

6.2 Power converter modelling

DC is the common output for batteries, while electrical motors are usually fed by AC current. Thus the need of an inverter to switch tide type. In addition, a change in frequency and voltage is mandatory in order to control motor rotational speed.

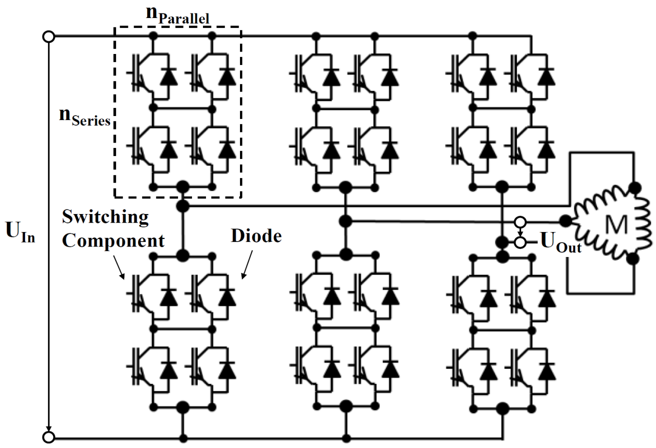

Figure 6.6. DC-AC inverter scheme.

The following model [5] aimed at describing power-converter efficiency and mass. Losses are calculated according to state-of-the-art technology, by scaling variables [70]. Few assumptions are also made, such that of constant working temperature, as for battery model. Furthermore, switching time is overlooked, switching frequency is much larger than the output frequency and ripples caused by AC are neglected. A switching component, i.e an IGBT, has current and voltage limitations (I_{ref} and U_{ref} respectively), which are reported in manufacturers data-sheet. If the electric drive-train is designed such that either current or voltage exceeds its maximum value, additional modules are added in series (n_{series}) and/or in parallel ($n_{parallel}$) so as to redistribute the "overload" which is burdening a single element.

$$n_{series} = \frac{U}{U_{ref}} \tag{6.18}$$

$$n_{parallel} = \left(\frac{I}{I_{ref}}\right) \cdot k_r \tag{6.19}$$

U is the input voltage and $k_r = 1.2 \div 1.3$ is an additional safety factor. Both parameter are rounded up to the next integer. I is the current, which can be calculated with the following ratio:

$$I = \frac{\sqrt{2} \cdot P_m}{\eta_m \cdot U_m \cdot \sqrt{3} \cos\varphi} \tag{6.20}$$

P_m is the motor input power, η_m and U_m its efficiency and voltage and $\cos\varphi$ is the inverter power factor (PF). This last is defined as the ratio between the real output power fed to the load and the apparent power supplied to the circuit. A PF less than one means that voltage and current waves are not in phase. In this analysis, a power factor equal to 1 is assumed.
Given the number of switches in parallel and in series, and the mass of a single switch $m_s \simeq 330\,g$, the power converter weight can be computed, remembering that for each phase two modules are needed. An additional constant $k_{services} = 2.5$ is introduced to take into account casing and mountings mass.

$$m_{s_{tot}} = m_s \cdot 6 \cdot (n_{series} \cdot n_{parallel}) \cdot k_{services} \tag{6.21}$$

Finally, the total mass can be obtained by multiplying equation 6.21 by the cable mass factor $k_{cable} = 1.4$, according to [71].

$$m_{inverter} = m_{s_{tot}} \cdot k_{cables} \tag{6.22}$$

A more straightforward way to calculate inverter mass is passing through its power density ρ_{inv}.

$$m_{inverter} = \frac{P_m}{\rho_{inv}} \cdot k_{cables} \tag{6.23}$$

Turning to losses, these are generally subdivided in conducting and switching ones. IGBT conduction losses can be considered as proportional to current, an can be expressed with next equation [70].

$$\begin{aligned} P_{c_{IGBT}} = & \left(\frac{1}{8} + \frac{\theta \cdot \cos\varphi}{3\pi}\right) \cdot \left(\frac{I}{n_{parallel}}\right)^2 \cdot R_{CE} + \\ & + \left(\frac{1}{2\pi} + \frac{\theta \cdot \cos\varphi}{8}\right) \cdot \frac{I}{n_{parallel}} \cdot U_{CE0} \end{aligned} \tag{6.24}$$

U_{CE0} is the threshold voltage, i.e the minimum voltage required to create a conducting path, R_{CE} is the IGBT internal resistance and θ is the modulation index [73], which takes into account signal variations.

$$\theta = 2 \cdot \frac{\sqrt{3}}{3} \frac{U_{motor}}{U_{in}} \tag{6.25}$$

In the above expression, the input voltage U_{in} can be approximately evaluated as $1.33 \cdot U_{motor}$ [72].

Transistors switching losses, furthermore, can be thought as function of both current and voltage; according to [70], they take the following form:

$$P_{s_{IGBT}} = E_{IGBT} \cdot f_{sw} \cdot \frac{I}{I_{ref}} \cdot \left(\frac{U_{in}}{U_{CE_{ref}}}\right)^{1.4} \tag{6.26}$$

The first term refers to the energy dissipated during transistor's on/off switching [74], $U_{CE_{ref}}$ indicates the maximum collector-emitter voltage, while f_{sw} is the switching frequency. Both are function of the environment which surround them and of the type of semiconductor. The number of commutations per second can be obtained with equation 6.27 [70].

$$f_{sw} = n_M \cdot p \cdot k_p \tag{6.27}$$

Going for order, n_M is the motor rotational speed, p the number of its pole-pairs and k_p is the IGBT's number of pulses per period. Now, since the switching frequency is orders of magnitude higher than n_M, and because the above expression is valid only if this happens, the coefficient k_p is taken approximately equal to 100.
On the other hand, giving to speak of diodes, losses trend governing equations' are quite similar to that for IGBTs and are reported hereafter. Again, conduction losses are function of current, whilst switching one are related either to current either to voltage [70].

$$\begin{aligned} P_{c_{diode}} = & \left(\frac{1}{8} - \frac{\theta \cdot \cos\varphi}{3\pi}\right) \cdot \left(\frac{I}{n_{parallel}}\right)^2 \cdot R_F + \\ & + \left(\frac{1}{2\pi} - \frac{\theta \cdot \cos\varphi}{8}\right) \cdot \frac{I}{n_{parallel}} \cdot U_{F0} \end{aligned} \tag{6.28}$$

$$P_{s_{diode}} = \frac{E_{diode}}{\pi} \cdot f_{sw} \left(\frac{I}{I_{F_{ref}}}\right)^{0.86} \cdot \left(\frac{U_{in}}{U_{F_{ref}}}\right)^{0.6} \tag{6.29}$$

R_F refers to the diode's resistance and U_{F0} is the associated threshold voltage. E_{diode} is the switching energy loss, whereas $I_{F_{ref}}$ and $U_{F_{ref}}$ are the forward current and voltage respectively, indicating that the diode is working in the "normal" conducting direction.
Finally, giving the output power and the sum of all losses times the number of switches, the inverter efficiency can be computed.

$$\eta_{inv} = \frac{P_{out}}{P_{out} + \sum P_{losses} \cdot n_{series} \cdot n_{parallel}} \tag{6.30}$$

The following tables collect all the reference values needed for modelling power converter performance [72].

IGBT		
switching energy	E_{IGBT}	195 mJ
threshold voltage	U_{CE0}	0.8 V
reference current	I_{ref}	900 A
resistance	R_{CE}	1.8 mΩ
collector-emitter voltage	$U_{CE_{ref}}$	1200 V

Table 6.2. IGBT reference values.

Diode		
switching energy	E_{diode}	53 mJ
forward voltage	$U_{F_{ref}}$	2.64 V
forward current	$I_{F_{ref}}$	900 A
resistance	R_F	1.71 mΩ
threshold voltage	U_{F0}	1.1 V

Table 6.4. Diode reference values.

6.3 Electric motor modelling

Electrical machines aimed at converting electrical energy into mechanical one in order to drive a load, in this case a propulsive fan. They are made of different parts: a core and an armature, which generates the electromagnetic field, a rotor, whose purpose is to transmit torque to a shaft, and a stator which surrounds it.
The parameters needed to conceive an e-motor are reported in the following design chart, in which the x-axis represents the rotational speed, while the y-axis refers to the torque.

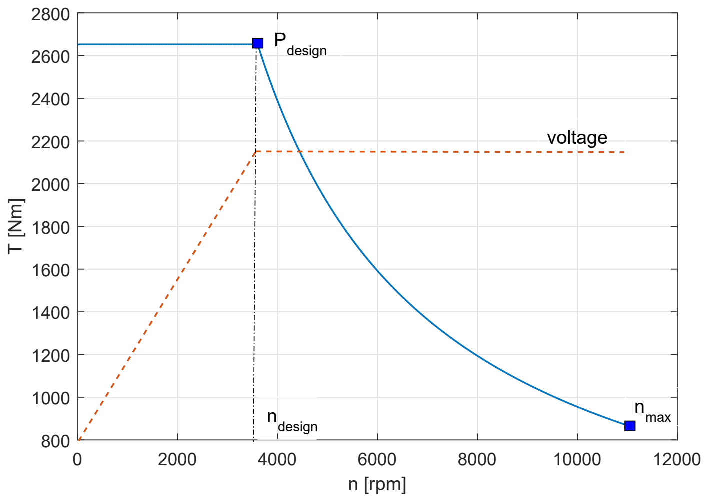

Figure 6.7. Electric machine chart.

The diagram is usually divided in two parts; the first is the constant torque zone, in which both power and speed increase, whereas the second is defined as the constant power region, where torque decreases as angular speed grows. If the voltage parameter is added on the same plot, its trend is going to be represented by the red line (fig.6.7). Being a power linear function ($V = \frac{P}{I}$), in the first zone it linearly increases until the maximum power is reached and then it remains constant all over the speed range (assuming constant current I).
With reference to applied mechanics equations, the design power can be simply determined by multiplying torque times the shaft speed.

$$P_{design} = T \cdot \omega \tag{6.31}$$

Torque can be expressed in terms of physical and electromagnetic quantities, as in the following equation [5].

$$T = N \cdot B \cdot A \cdot I \tag{6.32}$$

where N stands for the number of windings of one coil and B for the magnetic flux density; A represents the winding's conductor area, while I is the electric current. After that, B can be evaluated in terms of magnetic permeability and magnetizing field through the constitutive equation, and, in addition, further elaboration can lead to a formula relating flux density and coil length l.

$$B = \mu \cdot H = \frac{I \cdot N}{l} \tag{6.33}$$

Substituting equation 6.33 in 6.32, it is found that torque is a function of the electric current squared.

$$T = \frac{A}{l} \cdot N^2 \cdot I^2 \tag{6.34}$$

Again, power can be rewritten substituting the torque's relations already found in equation 6.30.

$$P = N \cdot B \cdot A \cdot I \cdot \omega = \frac{A}{l} \cdot N^2 \cdot I^2 \cdot \omega \tag{6.35}$$

On the other hand, voltage (V), or to be more precise, electromotive force (emf), can be related to the magnetic flux (φ) thanks to Faraday's law, which states that the emf induced is equal to the rate of change of φ.

$$V = -N \cdot \frac{d\varphi}{dt} \tag{6.36}$$

In practise, to generate strong magnetic fields, multiple coils are used, and for this reason an additional term N is added, in order to take into account the number of windings per coil. The minus sign introduced in the above formula is a consequence of the conservation of energy, more commonly known as Lenz's law. In fact, while Faraday's equation deals with the field magnitude, Lenz's one refers to current direction. It states that when an emf is generated due to a magnetic flux variation, the current produced and the associated magnetic field opposes the change which produces it.
The maximum voltage can be defined as:

$$V_{max} = N \cdot \varphi \cdot \omega \tag{6.37}$$

where $\varphi = B \cdot A$. Since the conductor area A is a fixed value, this formula states that when the peak voltage is reached, the motor rotational speed can be reduced only by weakening the magnetic flux, i.e decreasing the magnetic flux density B, which is a function of current flow. As a consequence, torque drops too.

At this point, combining all the equations given, it is possible to define scaling factors parameters' for the two regions highlighted in the T-n diagram. Proceeding this way, from equation 6.33 one can infer that, for both regions, current is proportional to the torque's square root, while voltage is linearly dependent with speed and $\sqrt{T}$ in the first zone, and constant in the second part of the chart. However, magnetic flux and flux density, being proportional to I^2, can be scaled with $\sqrt{T}$ and $\frac{1}{n}$ in the first and second zones respectively. n is the rotational speed in rpm, and can be related to the angular one, measured in $\frac{rad}{s}$, by the following expression:

$$n = \frac{60 \cdot \omega}{2\pi} \tag{6.38}$$

Scaling relations are summarized in the table below and permit to scale an electric motor for different power ranges.

	V	I	φ, B
Zone 1	n, $\sqrt{T}$	$\sqrt{T}$	$\sqrt{T}$
Zone 2	const.	$\sqrt{T}$	$\frac{1}{n}$

Table 6.6. Electric motors scaling factors.

Considering aircraft applications, the most common types of motors used are the reluctance motors, the asynchronous (ASM) and the permanent magnets (PSM) ones. In the following, due to the high efficiency, high torque density and relatively low mass in comparison to the others, the PSM architecture will be considered, as it seems to be the most suitable for propulsive purposes.

6.3.1 Geometric sizing

Motor geometry and mass estimation are based on the method utilized by Rucker [49]. The following scheme represents the principal geometric design parameters to be sized; the sleeve is not taken into account herein.

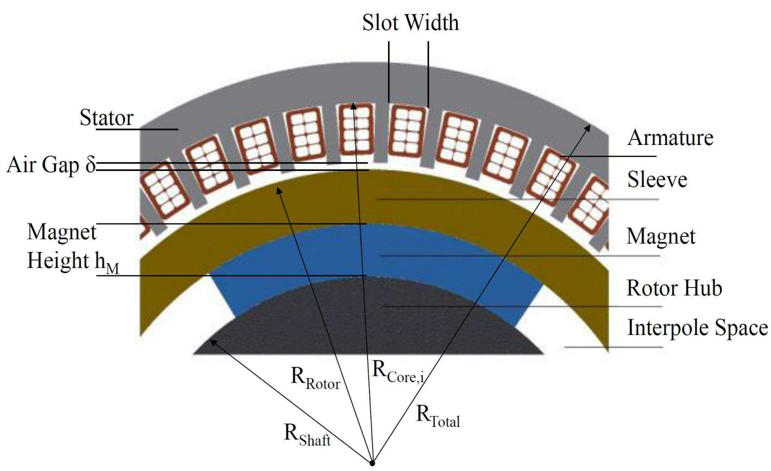

Figure 6.8. Motor geometry frontal section.

Starting with the rotor, its diameter can be computed according to the following equation:

$$D_{rotor} = D_{shaft} + 2 \cdot (h_m + \delta) \tag{6.39}$$

h_m is the magnets' heigh and can be estimated as 5 to 10 times the air gap or, assuming a maximum magnets thickness (t) equals to 20 mm, it can be estimated

as 0.35·t.
δ is the air gap expressed in meter, i.e the distance between stator and rotor necessary to permit relative motion, and it can be obtained using next relation [77].

$$\delta = \frac{C_1 + C_2 \cdot P_d^{0.4}}{1000} \tag{6.40}$$

The constants C_1 and C_2 are function of the number of poles n_p and are reported in the table below [77], whereas P_d is the design power.

	2 poles	> 2 poles
C_1	0.2	0.18
C_2	0.01	0.006

Table 6.8. Air gap constants.

D_{shaft}, on the other hand, is the shaft diameter; this parameter is a function and of the centrifugal force which is subjected to and of the material.

$$D_{shaft} = \sqrt{\frac{R_{p02}}{SF \cdot \rho_r \cdot \pi^2 \cdot n_{max}^2}} \tag{6.41}$$

R_{p02} refers to the maximum rotor yield strength, SF=1.5 is the safety factor, ρ_r the rotor density and n_{max} is the maximum allowable rotational speed. This last can be written in relation to frequency and poles number:

$$n_{max} = \frac{120 \cdot f}{n_p} \tag{6.42}$$

However, using power electronics it is possible to supply higher frequency and thus increment velocity, but there is a limit, usually specified by manufacturers, primarily caused by centrifugal forces and bearings temperature rise (the last can be avoid by using magnetic bearings).
Having these data at hand, the rotor length can be obtained with equation 6.43.

$$L_{rotor} = \frac{P_d}{D_{shaft}^2 \cdot \pi^2 \cdot n \cdot \sigma} \tag{6.43}$$

P_d is the design power, n the actual rotational speed and σ is the mean shear stress $\left(\frac{N}{m^2}\right)$ acting on the rotor.

$$\sigma = \frac{J \cdot B}{\sqrt{2}} \cdot \left(\frac{D_{shaft}}{D_{ref}}\right)^{0.25} \tag{6.44}$$

J is defined as the air gap current density $\left(\frac{A}{m}\right)$, while B is the magnetic flux density, measured in Tesla (T).
Next step is to calculate the total motor diameter with the formula reported hereafter.

$$D_{tot} = D_{core_i} + \frac{k_{s_{yoke}}}{n_{pp}} \cdot D_{rotor} + 0.1 \tag{6.45}$$

n_{pp} represents the number of pole pairs, whereas $k_{s_{yoke}}$ is the stator yoke coefficient, which is related to the stator thickness. D_{core_i} stands for core inner diameter and is given by summing up the rotor diameter and the slots depth.

$$D_{core_i} = D_{rotor} + 2 \cdot d_{slot} \tag{6.46}$$

Finally, the total machine length can be computed according to the following equation [77].

$$L_{total} = L_{rotor} + 2 \cdot \frac{L_{coil_{end}}}{2\pi} \tag{6.47}$$

The only unknown is the length of an end coil, which can be obtained taking reference to Rucker [49]. Here, the steps to undertake are mentioned. Firstly, few coefficients have to be defined:

$$\begin{cases} N_{s_{sp}} = 1 \\ N_{s_{fpct}} = \left\lfloor \frac{n_{slot}}{2 \cdot n_{pp}} \right\rfloor \\ N_{s_{sct}} = N_{s_{fpct}} - N_{s_{sp}} \end{cases} \tag{6.48}$$

The first term is the number of slot pole short pitch, the second is the full pitch coil throw rounded to the lowest integer and the last one is the actual coil throw.
The pole pitch is the distance between two adjacent poles centres, whereas the coil span is defined as the peripheral distance between two coil sides (fig.6.9). If the two quantities are equal, the armature is said to be full pitched, otherwise, if the coil span is less than the pole pitch, it is said to be short pitched. One reason to have this last configuration is to reduce harmonics, thus having as output a waveform which approximate at best the sinusoidal type.

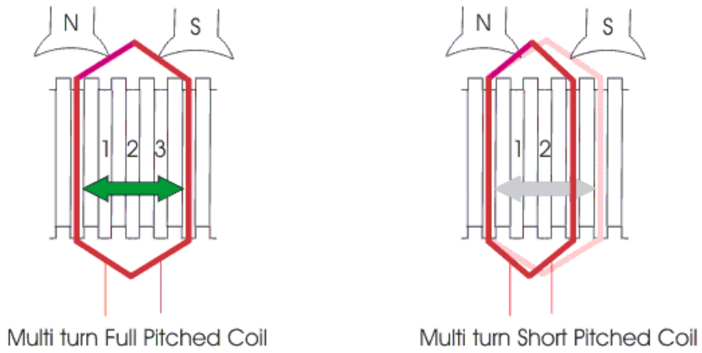

Figure 6.9. Pitch coil scheme.

To obtain the end coil length, it is also necessary to compute the end coil turn (l_{ect}) and the end length of half coil ($l_{e_{\frac{1}{2}}}$).

$$l_{ect} = \pi \cdot \left(\frac{D_{rotor}}{2} + \delta + h_m + d_{slot} + \frac{1}{2} \cdot d_{d_{slot}} \right) \cdot \frac{N_{s_{sct}}}{n_{slot}} \tag{6.49}$$

Looking at the relation $d_{d_{slot}}$ is the slot depression depth.

$$l_{e_{\frac{1}{2}}} = \pi \cdot l_{ect} \tag{6.50}$$

In the end, the following formula is set out and a geometrical approximation of motor's dimensions is finally obtain.

$$L_{coil_{end}} = 2 \cdot \frac{l_{e_{\frac{1}{2}}}}{2\pi} \tag{6.51}$$

Figure 6.10 shows the conductors' end turn and how they are fitted into the armature.

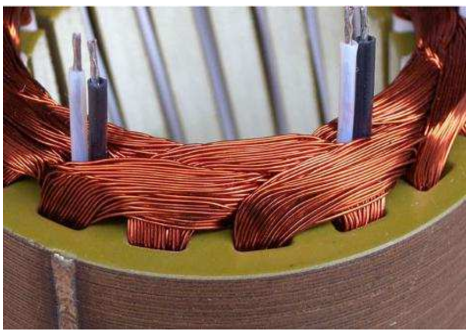

Figure 6.10. Conductors end turn.

The following table includes some reference parameters utilized during the sizing procedure of conventional electric motors.

number of phases	3
number of poles	2
safety factor (SF)	1.5
stator yoke ratio $k_{s_{yoke}}$	0.6
rotor tensile strength R_{p02}	$250 \cdot 10^6\ \frac{N}{m^2}$
magnet angle	50°
mass service factor k_m	0.13

Table 6.10. Motor design constant parameters [49].

6.3.2 Mass estimation

In this section, the mass of the main components is estimated.
To calculate the magnets mass, the number of pole pairs, the rotor diameter and length, the magnets' height and density (ρ_m) and the magnet angle (a_m) is needed [49].

$$m_{magnets} = n_{pp} \cdot a_m \cdot \left(\frac{D_{rotor}}{2} + h_m\right)^2 - \left(\frac{D_{rotor}}{2}\right)^2 \cdot L_{rotor} \cdot \rho_m. \tag{6.52}$$

Turning to the armature, its mass can be obtained multiplying volume per density, as in the following relation.

$$m_{arm} = A_{arm} \cdot L_{arm} \cdot \rho_{arm} \tag{6.53}$$

However, before joining to this final expression, some geometrical relations has to be set out. In great details:

$$L_{arm} = 1.42 \cdot n_a \cdot \left(L_{tot} + 2 \cdot l_{e_{\frac{1}{2}}}\right) \tag{6.54}$$

where n_a is the number of armature turns, defined as:

$$n_a = 2 \cdot n_p \cdot n_{turn} \cdot n_{tc} \tag{6.55}$$

n_p is the number of poles, n_{tc} is the number of turns per coil (assumed equal to 1), while n_{turn} is defined as the number of slots per pole per phase.

$$n_{turn} = \frac{n_{slot}}{n_p \cdot n_{phase}} \tag{6.56}$$

To define the armature area, instead, it is necessary to determine slots' geometry. In the case of an HTS motor, a slotless configuration is assumed and the slots' area is zero.
Giving reference to figure 6.11, the following relations take place.

$$\begin{cases} w_{st} = 2\pi \cdot \left(\frac{D_{rotor}}{2} + h_m + \delta + d_{d_{slot}}\right) \cdot \frac{1-p_{tf}}{n_{slot}} \\ w_{sb} = w_{st} \cdot \frac{\frac{D_{rotor}}{2} + d_{d_{slot}} + d_{slot} + \delta}{\frac{D_{rotor}}{2} + d_{d_{slot}} + h_m + \delta} \\ w_s = \frac{w_{st}+w_{sb}}{2} \\ A_{slot} = w_s \cdot d_{slot} \\ A_{slot_{tot}} = A_{slot} \cdot n_{slot} \end{cases} \tag{6.57}$$

Starting from the top, w_{st} is called the slot top width and the coefficient $p_{tf} = 0.5$ is the peripheral tooth fraction. w_{sb} is the slot bottom width, w_s is the average of the twos and A_{slot} is the slot area. In the hypothesis of a trapezoidal slot shape, this last term could also be obtained as: $A_{slot} = \frac{1}{2}(w_{st} + w_{sb}) \cdot d_{slot}$ Finally, once defined a slot fill fraction $s_{ff} = 0.5$ the armature conductor area can be calculated:

$$A_{arm} = \frac{A_{slot} \cdot s_{ff}}{n_{poles}} \tag{6.58}$$

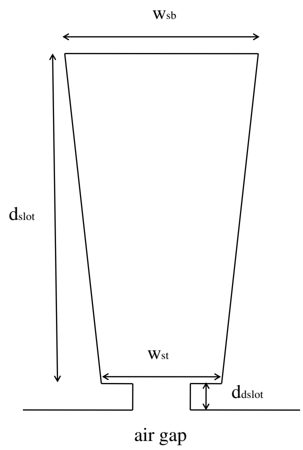

Figure 6.11. Stator slot geometry.

Moving on, having all these parameters known, the stator mass can be estimated. The assumption of equal length between rotor and stator has been done.

$$m_{stator} = \rho_{stator} \cdot L_{rotor} \cdot A_{stator} \tag{6.59}$$

where

$$A_{stator} = \pi \cdot \left[\left(\frac{D_{tot}}{2} \right)^2 - \left(\frac{D_{rotor} + 2 \cdot \delta}{2} \right)^2 \right] - A_{slot_{tot}} \tag{6.60}$$

In the same way, the quantities related to the rotor and to the shaft are determined.

$$A_{rotor} = \pi \cdot \left(\frac{D_{rotor} - D_{shaft}}{2} \right)^2 \tag{6.61}$$

$$m_{rotor} = \rho_{rotor} \cdot L_{rotor} \cdot A_{rotor} \tag{6.62}$$

$$m_{shaft} = \pi \cdot \left(\frac{D_{shaft}}{2} \right)^2 \cdot L_{tot} \cdot \rho_{shaft} \tag{6.63}$$

In order to take into account wires, frame and mounting masses, a service factor k_m equal to 13% of the total machine weight [60], is introduced.

$$m_{services} = k_m \cdot (m_{rotor} + m_{shaft} + m_{stator} + m_{arm} + m_{magnets}) \tag{6.64}$$

After that, the total motor mass is going to be available by summing up all components'.

$$m_{motor} = \sum_i m_i \tag{6.65}$$

The table below collects some parameters used in the design of standard motors' architectures and superconducting configurations. For the last one, the armature is not present any more.

	Conventional	Superconducting
air gap current density J $\left[\frac{A}{m}\right]$	65000	130000 [77]
magnetic flux density B $[T]$	1.05	2
ρ_{stator} $\left[\frac{kg}{m^3}\right]$	7860	7860
ρ_{rotor} $\left[\frac{kg}{m^3}\right]$	4800	4800
ρ_{shaft} $\left[\frac{kg}{m^3}\right]$	7700	7700
ρ_{magnet} $\left[\frac{kg}{m^3}\right]$	7400	6500
$\rho_{armature}$ $\left[\frac{kg}{m^3}\right]$	8900	6500
$n°$ of slots (n_{slot})	36	0
$n°$ of slots short pitch ($N_{s_{sp}}$)	1	0
slot depth (d_{slot}) $[m]$	0.025	0
slot depression depth ($d_{d_{slot}}$) $[m]$	0.0005	0
peripheral tooth fraction p_{tf}	0.5	0

Table 6.12. Convetional/HTS motor design parameters [49].

6.3.3 Losses and efficiency

Along this section, electric motor losses are going to be estimated [5]. The procedure outlined here traces step by step the one used for the inverter, in the sense that all quantities are obtain scaling them with reference values.
Basically five types of losses are considered.

- Core losses, due mainly to hysteresis effects in both stator and rotor, caused by iron an copper.
- Armature losses, related to Ohm's law.
- Friction and windage losses, due to rotor rotation and bearings.
- Air losses, caused by the air gap between rotor and stator.
- Stray losses, due to eddy-currents and flux variations.
- Miscellaneous losses, which take into account secondary effects.

Each loss category is suitable scaled to a reference power (1 MW): as a consequence, the following power ratio scale factor is introduced.

$$k_{sf} = \frac{P_{design}}{P_{ref}} \tag{6.66}$$

Starting from the core losses, these can be related to current, which in turn, is proportional to the torque square root and to the rotational speed, which is connected to the applied frequency too.

$$P_{l_{core}} = k_{sf} \cdot P_{l_{core_{ref}}} \cdot \left(\frac{T}{T_{design}}\right)^{\frac{1.353}{2}} \cdot \frac{n}{n_{design}} \tag{6.67}$$

Going on and dealing with armature losses, these are proportional to $R \cdot I^2$. Assuming that the resistance is constant for all speed's regimes, and remembering that torque can be related to current square, the subsequent equation follows.

$$P_{l_{arm}} = k_{sf} \cdot P_{l_{arm_{ref}}} \cdot \frac{T}{T_{design}} \tag{6.68}$$

Concerning friction losses, these are caused by mechanical parts' relative motion and are only function of the rotational speed of the machine.

$$P_{l_{fric}} = k_{sf} \cdot P_{l_{fric_{ref}}} \cdot \frac{n}{n_{design}} \tag{6.69}$$

On the other hand, air losses are function of many variables [78], such as rotor length, speed, air gap, air density (ρ_{air}) and viscosity (ν_{air}).

$$P_{l_{air}} = 1.7 \cdot \rho_{air} \cdot D_{shaft}^4 \cdot L_{rotor} \cdot \left(\frac{n}{n_{design}}\right)^3 \cdot \left(\frac{\pi^2 \cdot \delta \cdot D_{shaft}}{\nu_{air}}\right)^{-0.15} \tag{6.70}$$

The kinematic viscosity can be obtain dividing the dynamical one by the air density $\left(\nu_{air} = \frac{\mu_{air}}{\rho_{air}}\right)$. μ, in turn, is calculated through Sutherland formula or can be approximated by a power law.
There are only two types of losses to deal with: stray and miscellaneous ones. The first are function of the square of the rotational speed and of the square of the magnetic flux density [80]. This last can be linked to the torque, as outlined in table 6.6. With these considerations at hand, stray losses can be estimated with the expression reported hereafter.

$$P_{l_{stray}} = k_{sf} \cdot P_{l_{stray_{ref}}} \cdot \frac{T}{T_{design}} \cdot \left(\frac{n}{n_{design}}\right)^2 \tag{6.71}$$

The second and the last type of losses considered in this discussion, i.e those related to secondary effects, can be considered proportional to the rotational speed and to the current square.

$$P_{l_{misc}} = P_{l_{misc_{ref}}} \cdot \frac{T}{T_{design}} \cdot \left(\frac{n}{n_{design}}\right)^{1.25} \tag{6.72}$$

Reference values for 1 MW conventional and HTS machine are reported in the table below.

Type of loss	Conventional	Superconducting
$P_{l_{core_{ref}}}$	45860 W	11465 W
$P_{l_{arm_{ref}}}$	12429 W	0 W
$P_{l_{stray_{ref}}}$	1305 W	652.5 W
$P_{l_{fric_{ref}}}$	1027 W	1027 W
$P_{l_{misc_{ref}}}$	2953 W	2953 W

Table 6.14. Electric motor losses reference data.

Finally, motor efficiency can be obtained with the following expression, as the ratio of the power output to the power input.

$$\eta_m = \frac{P_{out}}{P_{in}} = \frac{P_{out}}{P_{out} + \sum_i P_{loss_i}} \tag{6.73}$$

Figure 6.12 and 6.13 show typical losses' trend for a conventional and a superconducting motor's architecture respectively.

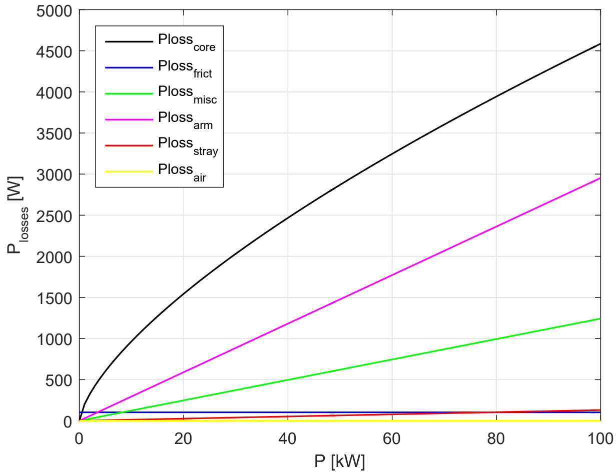

Figure 6.12. Losses for 100 KW - 3600 rpm conventional motor.

A great percentage of the total losses is given by the core ones. These are also due to stator and conductors materials' properties, and are related to their hysteresis characteristics too. Then there are miscellaneous and armature losses; these last are essentially in the form of heat, which is produced by ohmic effect as current flows into the windings. The other type of losses are very small compared against these three main categories and contribute only marginally.

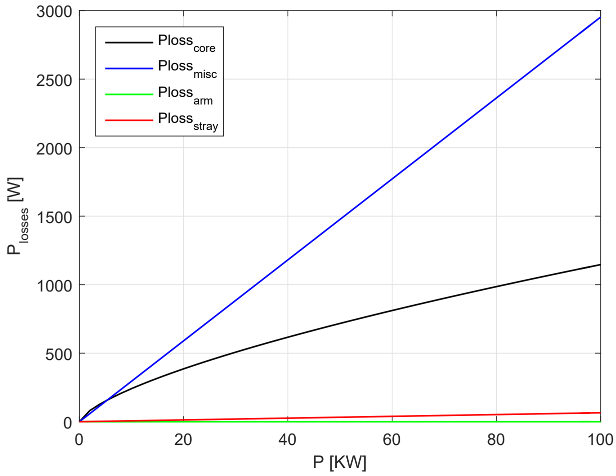

Figure 6.13. Losses for 100 KW - 3600 rpm HTS motor.

Losses associated to a superconducting machine are generally smaller in comparison to their ambient working temperature counterpart and this is a great advantage in

terms of efficiency. Core losses are approximately the fourth part of the preceding ones, while those associated to the armature are null. These great differences come from a different working ambient. In fact, cooling the motor to a cryogenic temperature results in zero (or almost zero) resistance to tide passage, other than a reduction in friction between mechanical components.
As with the non-HTS motor, air, stray and friction losses can be neglected.
In figure 6.14, total losses of both devices are plotted one against the other. At maximum power, the gap amounts to around 53%. At first glance, superconduction elements can halve losses, but when the component is added into a larger system, further considerations regarding weight, cooling liquid tanks or cryo-cooler system and global efficiencies, have to be done.

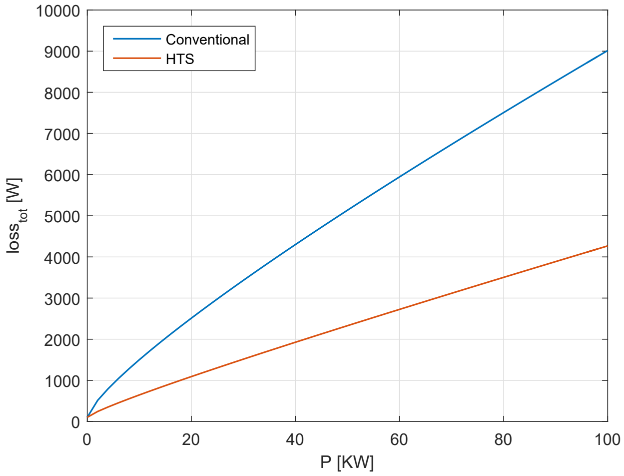

Figure 6.14. Motors total losses comparison.

In order to end the comparison, an efficiency plot is added (fig.6.15). The advantages of the HTS technology are in plain view. When providing 100 KW, +4.36% is achieved in the peak efficiency point. The difference between the two architectures is noticeable, and it is even amp up if power requirements raise over the megawatt class.

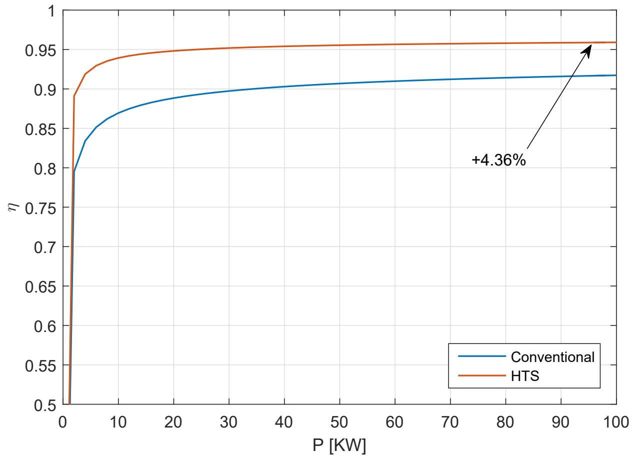

Figure 6.15. Motors efficiency comparison.

6.4 Cryo-cooler model

HTS technology requires an operating temperature of around 77 K. In order to satisfy this requirement, two possible solutions are available: to resort to liquid hydrogen or liquid nitrogen to cool the motor, or install a cryo-cooler. This system can be based on different thermodynamic cycles, such as the Gifford-Mc. Mahon, the Stirling or the regenerative one. Whatever the type, these equipments are bulky and heavy, and require a huge amount of power to fulfil their purpose.
In order to build a simple model [5], the required cooling power is needed.

$$P_{cooling} = P_m \cdot (1 - \eta_m) \cdot k_c \tag{6.74}$$

P_m is the motor power and η_m is the motor efficiency. k_c can be considered as the fraction of heat dissipated by the superconducting coils and can be approximated as 25% of core losses. From this, the cryo-cooler power can be estimated [1].

$$P_{cryo} = P_{cooling} \cdot \frac{T_{sink} - T_m}{T_m \cdot \eta_{cryo}} \tag{6.75}$$

In the above equation, T_m is the HTS motor working temperature, T_{sink} is the surrounding temperature (ISA + 10 K) and η_{cryo} is the cryo-cooler efficiency, which is quite low ($\simeq$30%).
In the end, the cryo-cooler mass can be computed assuming a specific power equal to 0.33 $\frac{kW}{kg}$ and multiplying it times the cooling power determined in equation 6.74.

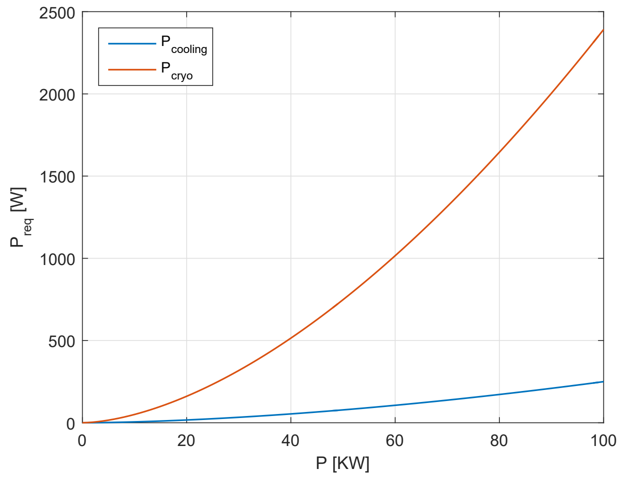

Figure 6.16. Cryo-cooler power for 100 KW HTS motor.

The figure above shows the power required for cooling a 100 kW HTS motor and the corresponding cryo-cooler power. The gap is due to the complexity of the aforementioned system and to the losses associated with its thermodynamic cycle. Raising motor power, the red curve of figure 6.16 grows more or less following a parabolic, near cubic trend; as a consequence, the apparatus, due to its low efficiency, becomes heavier and bulky, and it needs a huge quantity of energy to work properly.

Chapter 7

Validation

The models presented in the previous chapters are now compared against experimental data found in the open literature or taken from manufacturers' websites. Due to the lack or incompleteness of information concerning superconducting technology, motors' geometry and losses, it has not been possible to test some parameters against experimental ones.

7.1 Batteries

This section deals with battery validation. Values are compared against different cells' type, ranging from the common low voltage cylindrical models used every day to that installed on-board cars, planes and ships.

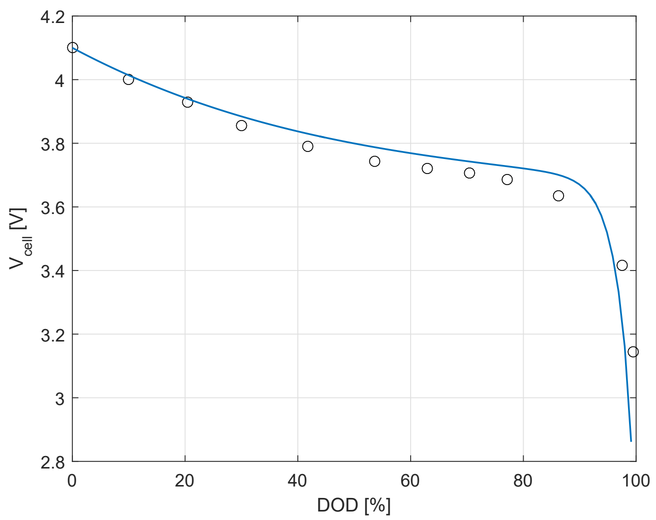

Figure 7.1. 3.7V cell depth of discharge.

err. [%]
0.066
0.283
0.165
0.665
0.947
1.124
1.007
0.896
1.040
1.688
6.253
6.185
mean err.
1.693 %

The figure above shows the discharge characteristics of a typical Li-ion cell operating at room temperature [33]. The trend obtained is in good accordance with experimental data till 80% DOD. When the curve turns and falls down up to the threshold voltage of 2.8 V, the model slightly deviate from experimental values, as it presents a steeper slope. Despite this, a mean error less than 2% is obtained.

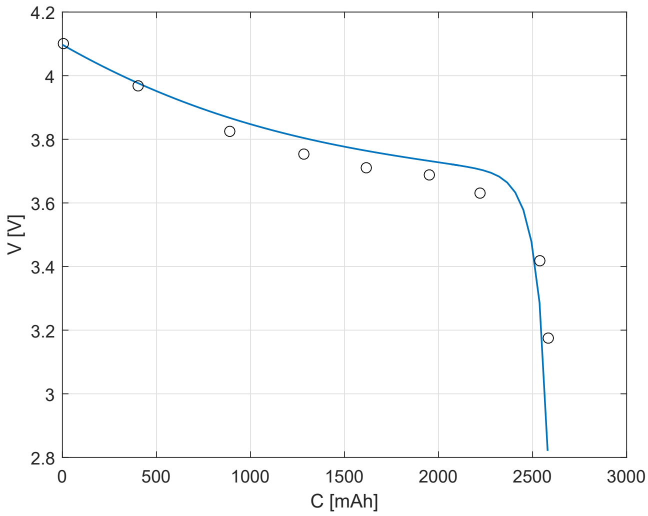

err. [%]
0.098
0.227
1.120
1.375
1.436
1.208
2.071
4.552
4.385
mean err.
1.83 %

Figure 7.2. 3.7V cell discharge capacity.

As in the previous figure, the decreasing trend which identifies a Li-ion battery from other storage systems (for example, lead-acid ones as a flatter characteristic) is measured with an error less than 1.5%. The curve plotted refers to an operating temperature of 25 $^{\circ}C$ and a discharge current of 490 mA. Again, the discrepancy raises up to 4% in the steepest zone, where the model is unable to completely catch electro-chemistry non-linear behaviour.

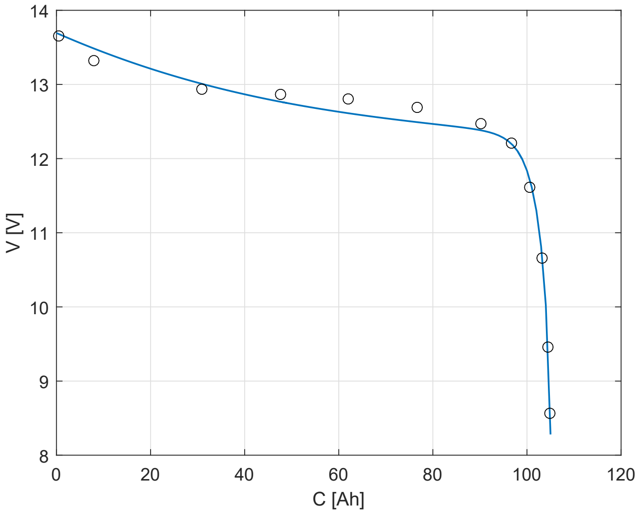

Figure 7.3. 12V battery voltage-capacity chart.

err. [%]
0.211
1.197
0.554
0.804
1.535
1.541
0.721
0.117
0.926
0.015
2.492
0.864
mean err.
0.915 %

This time, a 50Ah, 12.8 V nominal voltage battery is taken for the comparison [64]. The trend line seems in good agreement with the experimental data and the error is bound within 1.5%.

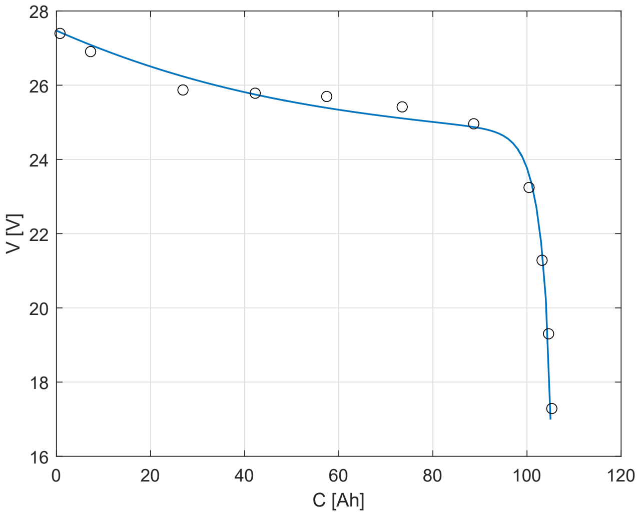

Figure 7.4. 24V battery voltage-capacity chart.

err. [%]
0.083
0.685
1.406
0.107
1.173
1.232
0.357
1.434
0.888
3.860
3.996
mean err.
1.384 %

Another validation has been made against a 25.6 V nominal voltage battery rated at 50 Ah [64]. The working temperature is kept constant at 25 $°C$. As already highlighted in the previous charts, the break in voltage from the nominal value till the threshold one has an error which is greater than that calculated among the "flat zone". Again, this can be seen as a limitation of the model in capturing all the non-linearities associated to the chemical and physical processes that take place inside the device during discharge.

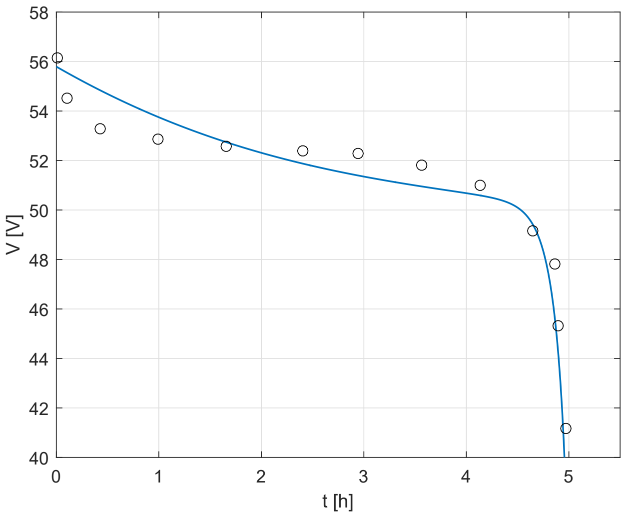

Figure 7.5. 48V battery voltage-time chart.

err. [%]
0.696
1.888
2.895
1.668
0.330
0.967
1.698
1.683
0.814
0.469
4.409
2.289
2.437
mean err.
1.711 %

The above chart represents the voltage-time behaviour of a 48 V nominal voltage, 25 Ah battery operating at ambient temperature [39]. The initial steep voltage drop is not completely traced and this is confirmed by an error of just shy of 3%. The second part of the slope, however, under estimates experimental data by more or less 1%. The slope ranging from 56 V to 50 V can thus be regarded as a mean-values line, capable of predicting the general trend.
The last part of the diagram, that referring to the highest discharge rate, has an error that amounts to $\simeq 2.3\%$, whereas the overall mean error decreases to 1.71%, providing that model predictions' are quite satisfactorily.

7.2 Power converter

The same procedure has been performed to validate the inverter model, as reported in the following.
The first comparison is made against a 220 V, 20 kW nominal power inverter [72]. The figure below shows diodes and IGBT's losses associated to this device for an extended power range too.

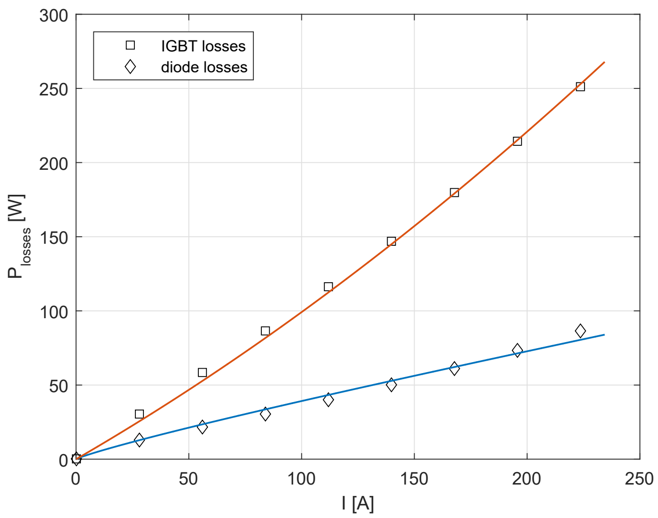

Figure 7.6. 20 kW inverter losses.

Table 7.2 and 7.4 collect experimental and model data, other than the percentage gap between them; a mean error value is also computed.
The low current zone has an error which is higher compared to the medium and high power areas, and can go beyond 10% (first reference data for IGBT). In the central part of the chart, the trend line fits better, with about 5% discrepancy, whereas the gap starts to raise again above 180 A. This region is outside the nominal inverter power range and some kind of error is to be expected. Anyway, for both types of losses, the average error lies under 5%.

diode losses		
exp. [W]	model [W]	error [%]
0	0	0
13.123	12.329	6.051
21.727	22.669	4.338
30.515	32.427	6.264
39.890	41.852	4.917
50.036	51.055	2.037
61.081	60.100	1.607
73.143	69.028	5.626
86.335	77.866	9.809
	mean err.	4.517 %

Table 7.2. 20 kW inverter diode losses.

IGBT losses		
exp. [W]	model [W]	error [%]
0	0	0
30.428	26.148	14.065
58.334	54.055	7.336
86.715	83.721	3.454
116.168	115.145	0.880
147.050	148.328	0.869
179.654	183.269	2.012
214.259	219.970	2.666
251.148	258.429	2.899
	mean err.	3.798 %

Table 7.4. 20 kW inverter IGBT losses

Next step through validation is the comparison with a more powerful inverter rated at 40 kW and with a nominal voltage of 220 V.

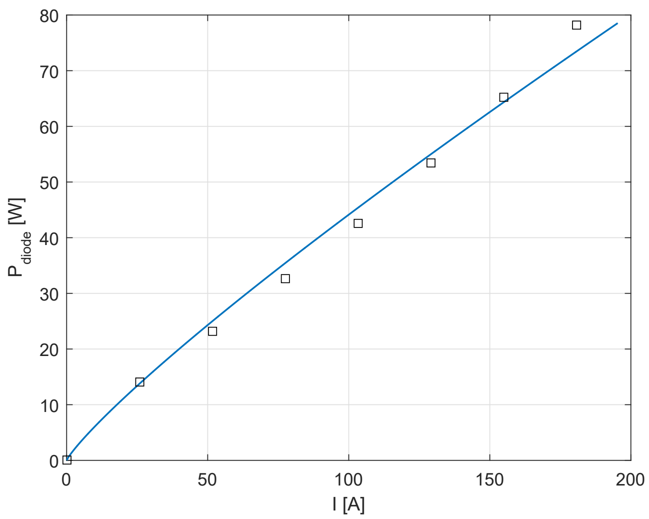

Figure 7.7. 40 kW inverter diode losses.

The approximation made by the model is quite good, despite the fact that it tends to underestimate the off-design peak power, as depicted in figure 7.7, on the upper-right-end-side corner. Around the area lying between 10 kW and 33 kW, experimental data are slightly overestimated; from a design point of view, this little losses' excess leads to a conservative approach.
From table 7.6, an average error has been determined, which takes into account the overall variation between model and manufacturer's data.

diode losses		
exp. [W]	model [W]	error [%]
0	0	0
14.022	13.766	1.829
23.212	24.994	7.677
32.604	35.431	8.673
42.625	45.386	6.479
53.471	54.997	2.855
65.278	64.343	1.431
78.165	73.475	6.000
	mean err.	4.368 %

Table 7.6. 40 kW inverter diode losses.

Figure 7.8, on the other hand, represents losses associated to the other inverter's main component, i.e, the IGBT. Usually these losses are greater than those associated to diodes, but the match with manufacturer's data is best, with a mean error equal to 2.3% (table 7.8).

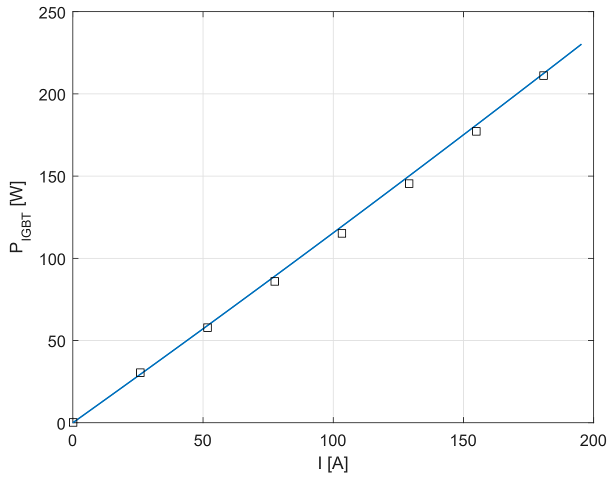

Figure 7.8. 40 kW inverter IGBT losses.

IGBT losses		
exp. [W]	model [W]	error [%]
0	0	0
30.379	29.345	3.402
58.024	59.024	1.724
86.039	89.037	3.485
115.027	119.384	3.787
145.345	150.063	3.246
177.277	181.076	2.143
211.087	212.424	0.633
	mean err.	2.303 %

Table 7.8. 40 kW inverter IGBT losses.

Dealing with efficiency, the two figures below (fig.7.9 and fig.7.10) represent the efficiency of a 385 kW inverter working at 455 V in function of the power output, in percentage [75]. At very low power 2% error is displayed; in what concerning the remaining part of the trend, the model is in great accordance with experimental results. For each datum, the error is less than 1% and the peak efficiency point is caught with a gap of only 0.18%, as reported in table 7.10.

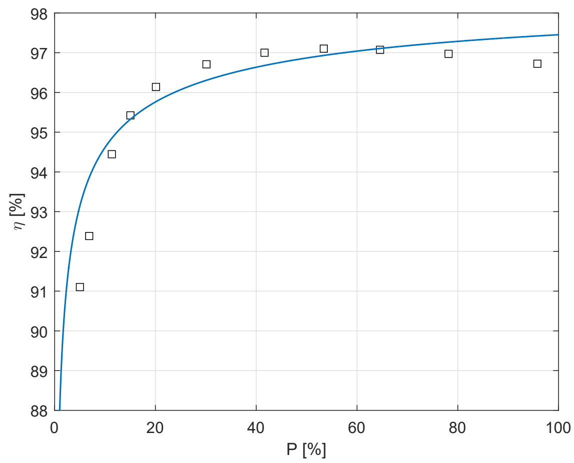

Figure 7.9. 285 kW - 455V inverter efficiency.

High-power converter efficiency @455V		
exp.	model	error [%]
91.099	93.160	2.262
92.390	93.876	1.609
94.443	94.851	0.432
95.431	95.328	0.108
96.135	95.768	0.382
96.713	96.307	0.42
97.007	96.678	0.339
97.106	96.932	0.179
97.078	97.106	0.029
96.971	97.267	0.304
96.729	97.422	0.716
	mean err.	0.616 %

Table 7.10. 285 kW - 455V inverter efficiency.

The following chart, on the other hand, represents the same power converter device working at a different input voltage (650 V instead of 455 V). The efficiency is slightly lower with respect to the low voltage operational configuration (table 7.12), and this is a consequence of the increasing losses ($P = V \cdot I = \frac{V^2}{R}$).
Other than that, the model agrees quite good with experimental data and a mean error of 0.594% is obtained. In the low power zone it falls in defect, however, the peak efficiency point predicted is underestimated by only 0.1%. Going beyond 70% power, the trend line prediction is going to overestimate reference's values; nevertheless, the error committed is acceptable, as it is far below 1%.

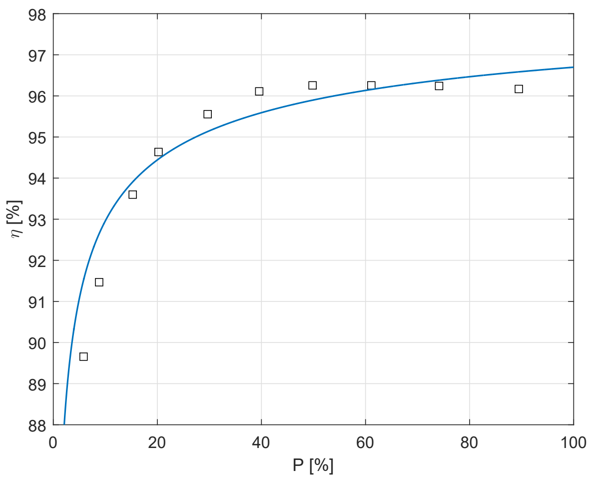

Figure 7.10. 285 kW - 650V inverter efficiency.

High-power converter efficiency @650V		
exp.	model	error [%]
89.653	91.513	2.075
91.461	92.641	1.290
93.593	93.904	0.333
94.630	94.458	0.182
95.559	95.130	0.450
96.107	95.576	0.553
96.255	95.896	0.373
96.256	96.156	0.104
96.238	96.382	0.150
96.171	96.585	0.430
	mean err.	0.594 %

Table 7.12. 285 kW - 650 V inverter efficiency.

As a last validation, a 250 kW power converter operating at 400 V is considered [5]. At very low power level, the model is not able to predict losses with sufficient accuracy; in fact, the error in this area is about 11%. As power raises, the gap between experimental data and model ones diminishes, and, as a consequence, the prediction becomes more accurate. Above 200 kW, total losses are underestimated by around 5%, and the same value is obtained for the average error.
In table 7.14, one can see that the main difference comes from the first line, where the inverter is working at off-design conditions. If this coefficient is not taken into account, the mean error would reduce to about 3.5%. In any case, the prediction seems quite satisfactorily in what concerning the high power region.

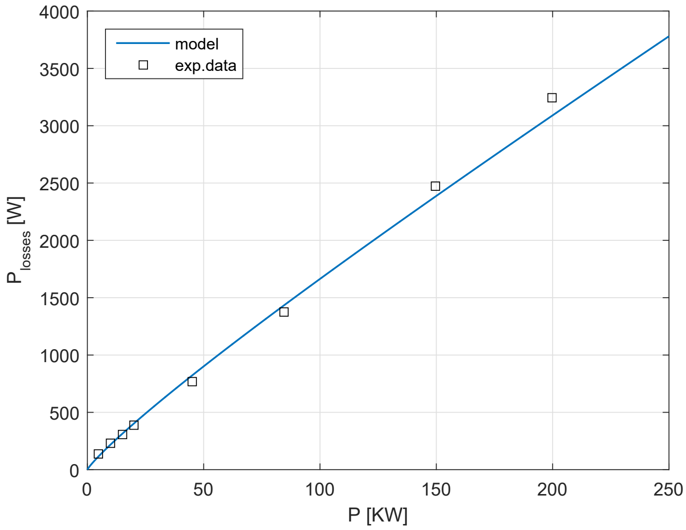

Figure 7.11. 250 kW - 400V power converter losses.

Power converter total losses		
exp. [W]	model [W]	error [%]
130.478	115.7	11.326
228.498	219.6	3.894
308.658	314.4	1.860
385.847	400.8	3.875
768.853	821.2	6.808
1377.497	1433.3	4.051
2475.876	2381.2	3.824
3245.284	3085.0	4.939
	mean err.	5.072 %

Table 7.14. 250 kW power converter losses.

7.3 E-motor

To end the chapter, only the electric motor validation has to be done. Comparisons between the model derived and manufacturers' data are going to be done primarily on what concerning total mass and overall losses. Due to the lack of information available, it was not possible to compare each single type of loss, and the same goes for geometric parameters. However, overall mass and total loss estimations, which are the main benchmarks needed for the implementation of test cases and preliminary design, have been done for conventional and HTS machines. Because of the recent developments of this kind of technology, data are very rare and the validation process has been made only with available values coming from the public domain.
The figure below shows the geometry and mass comparison for a 40 kW, 4 poles, permanent magnets synchronous motor [5]. Being the model calibrated on the megawatt class, this lead to some errors when applied to lower power machines. As a consequence, the mass of each constituent is not perfectly caught and a 9.5% mean error is present. None the less, the overall mass differs only by 1.37%, and this is the main value to take into account during preliminary drive-train design.

40 kW PMS motor @5832 rpm			
	data	model	error [%]
rotor diameter [m]	0.18	0.177	1.67
rotor length [m]	0.04	0.043	7.75
armature [kg]	5	5.494	9.88
magnets [kg]	0.7	0.665	5.00
stator [kg]	9	8.2	8.89
rotor+shaft [kg]	4.2	4.8	14.29
Total [kg]	18.9	19.159	1.37
		mean err. [%]	9.51

Table 7.16. 40 kW PMS motor mass comparison.

Table 7.3 shows other two electric motor comparisons' [49]. Due to the lack of information concerning material density, typical values has been used and this has lead to a certain amount of error in mass estimation, especially in the first case. For the less powerful machine, the error is smaller and it amounts to 7%.

20 MW motor @150 rpm			
	data	model	error [%]
pole pairs	6	6	0.00
n°phases	15	15	0.00
rotor radius [m]	0.425	0.421	0.88
mass [kg]	112.5	137.31	18.07
4.3 MW motor @150 rpm			
	data	model	error [%]
pole pairs	100	100	0
mass [kg]	65000	69887	6.99
length [m]	3.8	3.97	4.28

Table 7.18. Motors' comparison.

View that an electric motor can work also as a generator by inverting its power flow, some tests has been done also for this case, as reported in the table below [49].

100 kW generator @160 rpm			
	data	model	error [%]
mass [kg]	2205	2393.8	7.89
length [m]	0.222	0.204	8.66
400 kW generator @36 rpm			
	data	model	error[%]
rotor radius [m]	1.05	0.997	5.29
pole pairs	83	83	0
n°phases	3	3	0
length [m]	0.65	0.618	5.18
250 kW generator @1050 rpm			
	data	model	error [%]
pole pairs	14	14	0
n°phases	3	3	0
mass [kg]	283.3	293.04	3.32

Table 7.20. Generators' comparison.

Despite the fact that many information are missing, the estimation is quite in good agreement. For each case, the error is far below 10 %, and goes down till 3.3% for the 250 kW generator. Machine's length also falls in the same error range.
For preliminary design studies, in which each drive-train component's has to be sized, these models can give quite good results in terms of mass, losses and efficiency. Obviously, proceeding with the project and going further in detail, some refinements should be done, in order to take into account all possible aspects.
The validation procedure ends dealing with HTS machines, as reported in figure 7.3 [5] and 7.3 [82].

HTS motor @2000 rpm			
	data	model	error [%]
power [MW]	22.2	22.2	0
mass [kg]	1110	1254.7	11.53
efficiency	0.997	0.987	1.06
cryo-cooler mass [kg]	149	157	5.10
total losses [kW]	137.5	138.15	0.47
cooling power [kW]	34.30	33	3.94

Table 7.22. 22.2 MW HTS motor.

As for conventional machines, mass is slightly overestimated due to the absence of data regarding materials' density. Apart from this, efficiency is predicted with only 1% error and total losses with less than 0.5%.
Figure 7.12 represents the efficiency trend for a 1 MW HTS motor running at 1800 rpm and at an operational temperature of 70 K.

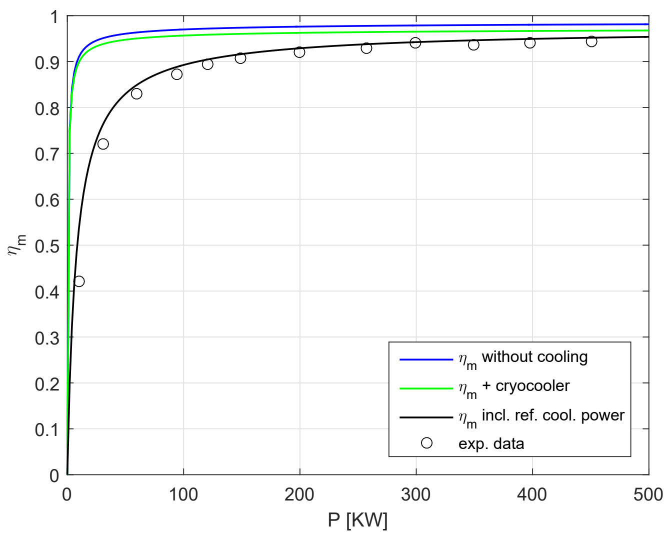

err. [%]
11.256
6.190
2.374
1.945
1.108
0.928
0.972
0.920
0.129
1.031
0.951
0.901
mean err. [%]
2.392

Figure 7.12. 1 MW HTS motor efficiency.

The motor gains its maximum efficiency without the cryo-cooler apparatus (blue line), but only apparently, because it needs it to work at cryogenic temperatures. Unfortunately, this kind of machines are characterized by a very low efficiency

($\eta_{cryo} \simeq 0.33$) and their introduction inevitably leads to additional losses. Taking into account the cooling power too, the lowest curve is reached (black line). Even if further decreased, the efficiency is still above 90% and this is one of the main characteristics of such devices.
A comparison against experimental data leads to a $\simeq$2.4% mean error, showing that the model derived is able to predict overall efficiency quite well. Of course, this also happens because the last is scaled on MW class power.
The HTS model developed was finally compared with the Boeing-Sugar one, as presented in the table below.

HTS motor @13000 rpm			
	data	model	error [%]
total mass [kg]	303.902	295.011	3.01
shaft+rotor weight [kg]	7.954	8.174	2.70
stator weight [kg]	124.743	131.15	4.89
total losses [W]	25349	23984	5.69

Table 7.24. 8 MW HTS motor.

3% error in total mass estimation and about 5.5% in total losses is committed. Even if this kind of systems are not completely developed today, this can be seen as a preview of future technology development.

Chapter 8

Hybridisation test case

In the following, the models outlined in previous chapters are going to be applied in order to run a test case. This consists in the partial electrification of a high bypass-ratio turbofan equipping a middle range passengers liner aircraft. To do that, an electric drive train, i.e batteries, power converter and motor has to be conceived, sized and coupled in series or in parallel, depending on the configuration adopted, with the conventional propulsion system. As these steps are accomplished, the all system is going to be "integrated" within an airplane model to fly a typical mission and to check its feasibility, both in terms of performance and efficiency.
More specifically, the study will focus only on take-off and climb segments (the idea here is that batteries will be recharged during cruise, where the engines are running at their peak efficiency point), which are the most critical phases concerning power requirements and fuel consumption. The aim is to highlight possible benefits coming from the introduction of an electric propulsion system, which should compensate the power burden of the gas-turbine engine. Since a percentage of the total power is going to be fed by an e-motor, the fuel consumption of the kerosene-based engine should reduce, an thus CO_2 and NO_x emissions. With this in mind, the turbine power requirements, in particular those for the low pressure one, will change, and depending on the power-split considered, they will reduce by a certain amount. As a consequence, the number of stages could be cut-down, and the component's weight, which typically accounts for 30% of that of the entire engine, will diminish. More in general, when a power-split is applied and an amount of energy is introduced by an external source, the whole turbo-engine should be resized, so that the full potentials of the hybridization process should be sufficiently appreciated. The core will shrink and some LP stages will be removed, along with their complex cooling system. Considering the external dimensions fixed, the bypass-ratio will increase, resulting in an efficiency increment, which in turn will lead to a fuel consumption reduction. In any case, one of the main points is that the turbofan can be sized smaller and more efficient, thus saving weight. However, in the following analysis the engine is kept fixed (same geometry, same number of stages and same

mass).
Till now, all the considerations done refers only to the propulsion system itself. Things changes if this is integrated within the aircraft; their mutual influence and complex interaction can lead to results which can partially erase the good aforementioned premises coming from the partial electrification of the gas-turbine engine. For example, even if the turbo-machinery burns less fuel, and, at a first glance, the tanks' volume can be reduced, this does not mean that the aircraft will continue performing the same mission in an efficient way. In fact, new variables come into play, such as the weight of the electrical components, and especially that of the energy storage system. Due to their low power density, the amount of batteries to be carried on-board can be very huge; as a consequence, the aircraft maximum take-off weight (MTOW) increments, along with fuel consumption during taxi and take-off manoeuvres. If the engines are sized smaller, in comparison to the non-electric case, they have to run at a higher speed and temperature (TIT) in order to produce the thrust required for lift-off and so they need more kerosene. In addition to this, despite the fact that during climb the electrical train can play a significant role, the cruise segment can be affected by higher fuel requirements with respect to a conventional configuration. At this point, two options are available: to install additional tanks, with consequent further increase in weight, or to reduce aircraft range.
As seen above, the variables in the way are multiples, and their interactions are anything but self-evident. Things can go in one way if considering a free standing element, but when coupled within the whole system, they can change, following a different road, pursuing a particular evolution.
There is to say that, with current technology, the electrification of large aircraft is much more problematic than that of smaller one, the main barrier being accumulators' energy density, thus weight and volume. Evidences of this are the moderate number of ultra-light and general aviation class all electric airplanes. These machines are characterized by low structural weight, low performance, relative limited endurance and a very short profile mission. The powers involved are usually in the tens or maximum hundreds kilowatt and so batteries' dimensions are limited accordingly. Some examples are the Pipistrel Alpha Electro [81], propelled by a 60 kW electric motor and a 17 kWh Li-poly batteries, for a total 90 minutes endurance, the Airbus E-fan [4], a twin-seat mid-wing all-electric plane powered by Li-ion batteries, and so forth. There is also the Extra 330LE, which belongs to the acrobatic class and lifted-off for the first time in July 2016. It has a total endurance of more or less 20 minutes and it is equipped with the SP260D electric motor produced by Siemens, fed by 14 Li-ion batteries with a total capacity of 18.6 kWh.
Concerning commercial liner aircraft, such as those of the A320 and B737 class, any prototype has been conceived till nowadays, even if great efforts have been made in the last years. Electric technology is improving fast, but it seems that this is not enough for a full electrification. Partial hybridization is relatively more feasible

and is the common road which industries try to look forward.
Following this philosophy, a percentage of the total power demand (the so called power split) is stored in batteries and fed to the main turbo-engines through electric motors. The goal is that of reducing fuel consumption and increase efficiency, in such a way as to meet 2035 and 2050 emissions' targets.

In summary, the test case that is going to be developed hereafter consists in analyse the feasibility and every possible potentials coming from the partial electrification of a middle range passengers aircraft. To do so, an engine model is needed, as well as the airplane one. Once having these at hand, a typical mission will be flown, in order to see the behaviour of the overall system.
The flow chart which follows aims at giving a general overview of the processes involved.

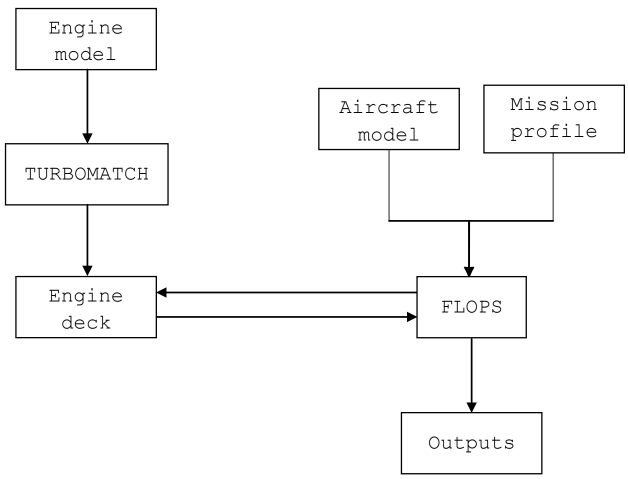

Figure 8.1. Simulation process flow chart.

The engine model is taken by Turbomatch to compute on-design and off-design conditions; some of these lasts are collected in the so called engine deck and are interpolated so as to obtain the complete engine mission envelope. On the other side, Flops receives as inputs the aircraft model and its mission profile. When the simulation starts, for each time step, to which corresponds a precise value of altitude and Mach number, Flops takes reference to the engine deck, which returns all the information needed concerning the gas-turbine engine, and makes its computations on fuel burns, which are then giving as outputs.

8.1 System architecture

In dealing with turbo/hybrid-electric propulsion, different configurations are possible, but the most common are the series and the parallel ones. View that liner aircraft are usually equipped with turbofan engines, a parallel hybrid architecture (fig.8.2) is chosen to staging the test case; the general arrangement is reported, for clarity, in the figure below.

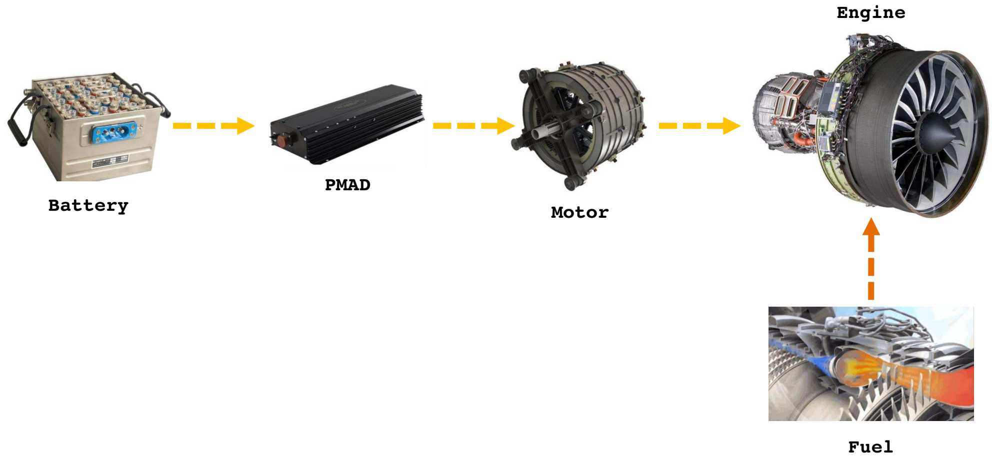

Figure 8.2. Parallel turbo-hybrid architecture.

In a little more detailed way, the turbo-engine low pressure spool is connected to an electric motor through a shaft. In turn, this last is driven by energy stored in Li-ion batteries. Between them, a power converter is interposed, which purposes are to convert DC current to AC one and to control motor rotational speed.
In this way, power is produced both from burning fuel inside the combustion chamber and from the electrical energy conversion process performed by the second "ambient-friendly" power train. In order to take into account the percentage of power introduced by the electric train with respect to the total required, a split-ratio, also called power-split factor (PS), is introduced.

$$PS = \frac{P_{el}}{P_{shaft}} \cdot 100$$

This figure of merit gives an idea about the power-splitting settings, other than a preliminary outlook on electric components sizes. Of course, as the PS increases, the energy that has to be stored in batteries grows too, as well as their mass and volume. Same trends go for the other electrical components, even if in this case the dimensions' increment is much more moderate.

Once the architecture has been defined, it is possible to proceed in setting up the analysis by adding an engine model.

8.2 Engine model

In this section, the engine model developed with the in house software for aero-gas-turbine engines performance calculation is explained, along with a short excursus on physical and thermodynamic phenomena occurring in this type of turbomachinery, and by touching on the Brayton cycle too (fig.8.4).
The baseline configuration chosen is a two spools ungeared high bypass-ratio turbofan for civil applications (fig.8.3), belonging to the 25÷30 klbs thrust class.

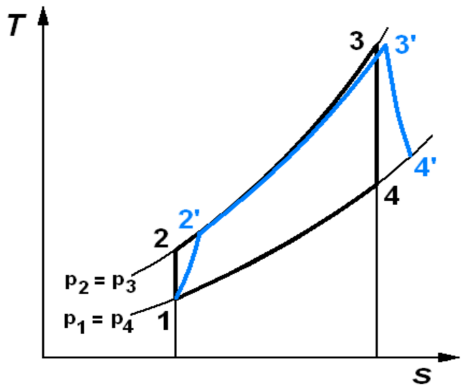

Figure 8.3. Brayton cycle.

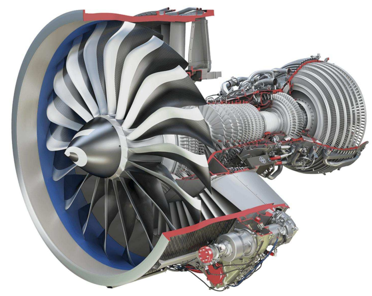

Figure 8.4. Two spool turbofan.

The air mass flow enters the inlet, it is slew down, and then it enters the fan, where the first compression takes place. In this type of engines, this row of blades is capable of producing even more than 70% of the thrust required, and this value increases in parallel with its diameter. After that, the mass flow rate splits in two parts, namely the "cold" and the "hot" one. The first is bypassed and directly goes into a nozzle, whereas the other, which is the minor part, enters the core and takes part to the thermodynamic cycle. The ratio of these quantities is defined as the bypass-ratio (BPR) and it is considered a design variable. Following the hot-flow path, this enters the low pressure compressor, which is constituted by a series of stages, made up of a rotating part, the rotor, and a static one, i.e the stator. Through these row of blades, the flow is further compressed and slew down; as a consequence, pressure, temperature and density raise. There is another series of stages mounted on a second shaft, which is the high pressure one. The process the air-mass undergoes flowing in these components is the same as that set out for the LP compressor. At the end of the compression, the combustion takes place; atomized fuel particles are sprayed in an annular chamber and mix with the relatively hot-air ($\simeq$900 K) coming from the HP compressor. Ideally, the process should be at constant pressure (same iso-p curve), but practically some losses occurs and the pressure drops of approximately by 3%. In any case, the flow purchases quite lots of energy and left the burner at more than 1600 K. This great amount of energy hoards by the fluid has to be extracted through an expansion process, that takes place in a certain number of reaction turbines. These turbo-components are exactly the compressors' counterpart; in fact, they consist of a stator, which routes the flow, followed by a rotor. The air mass expands and accelerates, decreasing both pressure and temperature. The power obtained is then used either to keep the spools rotating, balancing the need of the compressor, either to drive external devices (power off-take). Finally, the flow joins the nozzle, where it is further expanded, before being ejected to the ambient. It should be noted that the two streams, i.e the core and the bypass one, have dedicated nozzles and do not mix together (the last mixed flow bypass-turbofan was the Rolls Royce RB211).

Continue dealing with turbo-engines, it is time to provide more details in what concerning the turbofan model defined in Turbomatch. The block diagram reported hereafter highlight the main components and their connections.

In general, this kind of turbomachinery is made up of a fan, two compressors mounted on different shafts, a burner, two turbines, and two nozzles. In addition, there are also many ducts and bleeds, these last for cooling requirements.

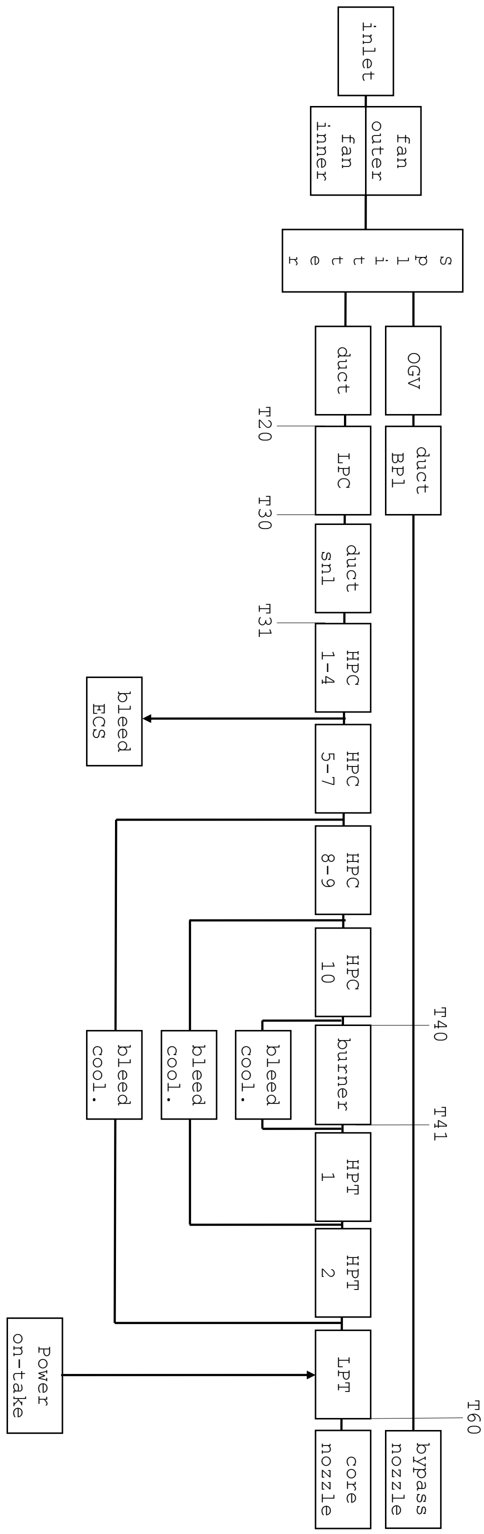

Figure 8.5. Turbofan engine model.

Starting from the left side, the first block refers to the inlet, which purpose is to channel the flow and slow it down, with as less losses as possible. These one are computed, according to USAF MIL SPEC-5008B, introducing a pressure recovery factor, expressed as a function of the upstream Mach number.

$$\eta_R = 1 - 0.075 \cdot (M_0 - 1)^{1.35} \qquad\qquad 1 < M_0 < 5$$

Before going on, a bypass ratio is also defined; instead of using the usual notation, i.e the relationship between the cold and the hot mass flow rate, a new variable is introduced, defined as the ratio of cold mass flow to the total one.

$$\lambda = \frac{\dot{m}_{cold}}{\dot{m}_{cold} + \dot{m}_{hot}}$$

Then, the air mass enters the fan, which is mounted on the low pressure spool. This component is characterized by a polytropic efficiency and a pressure ratio, computed as the ratio of the outlet pressure to the inlet one.

$$\pi_f = \frac{p_{out_f}}{p_{in_f}}$$

A degradation factor is also added to take into consideration losses coming from tip clearances, non-uniform and not 1D-flow. Given that blades height is not negligible, the flow behaves differently moving from the hub to the tip and for this reason two different maps are used: one for the inner zone, which coincides approximately to that aligned to the core, and one for the outer region, where transonic effects may take place too, especially at the blade tip.
Always making reference to fig.8.5, a splitter is added. As the name suggests, this separates the total air mass in two: most of it is bypassed and flows in the external channel, while the remaining enter the gas-turbine and takes part to the thermodynamic cycle (compression, combustion and expansion). To end the description of the outer path, three blocks are still missing: the first is an outlet guide vane (OGV), which straightens the stream, than a duct, which serves as modelling losses along the route, and finally a fixed area nozzle, where the flow gains speed and is ejected outside. Duct losses are calculated as the ratio between the pressure jump along the channel and the inlet pressure, as reported hereafter.

$$\epsilon_{duct} = \frac{\Delta p}{p_{in}}$$

Now, giving to speak of the inner path, a duct is inserted before the low pressure compressor, and it has the same tasks as the one put in the bypass region. After that, there is the LPC block, sometimes also refers as booster. As for the fan, the performance of these stages are represented on a map, along with their efficiency. The high pressure compressor (HPC), mounted on a second shaft, follows, but before it, an additional block is inserted in order to model swan-neck duct losses. The HPC is divided in four parts, each of them containing a certain number of stages and defined by their own efficiency. Again, each component has its map and its surge margin "Z", defined as a ratio of pressures' ratio differences.

$$Z = \frac{\pi_c - \pi_{choke}}{\pi_{surge} - \pi_{choke}}$$

One can also see some "output branches" located at intervals. These are bleeds for the environmental control system (ECS) and for the high pressure turbine blades cooling, respectively. The percentage of air extracted is computed by means of the bypass ratio coefficient λ.
Once the air is compressed, it enters the burner, where it mixes with fuel and takes part to the combustion (no water is injected during the process). The parameters involved in the model are the pressure loss coefficient, the combustion efficiency and the turbine inlet temperature (TIT) design variable.
Following the path toward the right, the high pressure turbine is represented. Because of the very high temperatures experienced in this region of the engine, the two stages are made of nickel-based superalloy and are cooled with air coming from the HP compressor. As for their counterpart, they need a dedicated map which includes iso-efficiency lines and additional degradation factors, in order to incorporate non-uniform flow effects. The second to last component is the low pressure turbine (LPT). The main difference with respect to the HP one is that this includes an input option, i.e, the possibility of feeding in power from external sources, such as an electric motor. In the end, once the flow has expanded and consequently cooled, it enters a nozzle and it is ejected downstream. Being a high-bypass ratio turbofan, the hot nozzle differs from the cold one and the two flows do not mix, even if in this way performance should decrease a bit. It would be better to have a mixed configuration, but the weight and wetted surface added by the mixer should affect the effective theoretical incomes.

8.3 Aircraft model

The aircraft model to which reference is made to run the simulation in NASA Flops belongs to the passengers liner class and its sizes are comparable to those of an A320/B737. The maximum take-off weight is set to about 181000 lbs, while each engine has an overall mass of more or less 6500 lbs. It can host on-board 150-200 passengers and 22000 kg maximum fuel weight (MFW), housed in separated wing tanks, plus $\simeq$1050 kg as reserve, in case of diversion to another airport.
The mission it has to fly is the typical one performed by middle range airplanes, and it consists of the following segments: taxi, take-off, climb, cruise, descent and landing. The graphical representation of the profile is reported in figure 8.6.

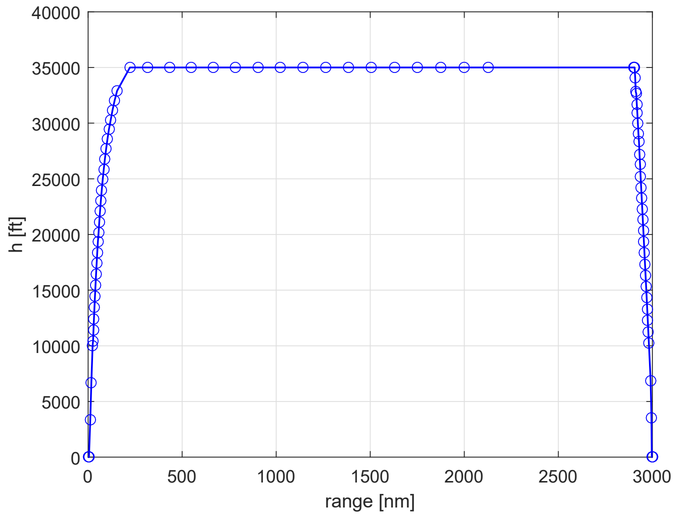

Figure 8.6. Mission profile.

Ten minutes are considered for taxi and take-off operations, while the climb phase lasts more or less 30 min. This is because the program is set so as to optimize the climb, in such a way to have the minimum fuel consumption. In addition to this, some other options are added, like the optimum altitude for cruise Mach number ($M_0 \simeq 0.82$) and the maximum lift to drag ratio $\frac{L}{D}$ during the descent segment.
Despite these considerations, the case study will focus only on the first two flight phases which will be partially electrified, i.e take-off and climb.
In running the analysis with different power-split, the "original" aircraft configuration and weight will remain fixed, and also the engines and the fuel one, whereas the additional mass coming from the introduction of electrical components, especially that of batteries, is added as "dead weight" and included in that of the structure. In doing so, the MTOW will change whenever the percentage of electrical power fed to the turbofan increases, and the same is applied for the maximum climb weight (MCW).

8.4 Electric train sizing

In order to run the test case, it is necessary to size all the electrical components. To do so, a first simulation is run in Flops, so as to obtain the power profile relative to take-off and climb phases; more specifically, the LPT power has to be computed (fig.8.7). All charts and sizing refer to one single engine.

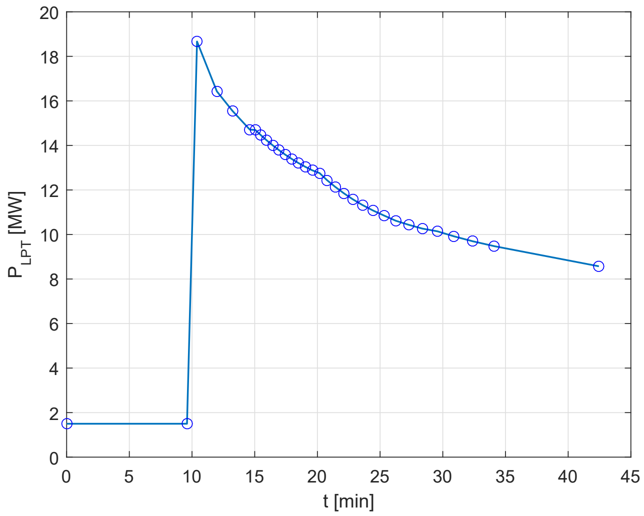

Figure 8.7. LPT power profile.

The maximum power requirements are at take-off and the peak value equals 18.67 MW (this value refers to one single engine). A percentage of this number is than taken to calculate the power-split fraction, i.e the amount of power to be produced by the electrical modules. Consequently, the electric motor and the power converter are sized accordingly. In what concerning batteries, the sizing process starts from here as well, by integrating in time the power profile. The procedure is going to be described in the following subsections, whereas the table reported hereafter shows the peak electrical power requirements for different PS.

PS [%]	Power [W]
5	933311.765
10	1866623.530
15	2799935.295
20	3733247.059

Table 8.2. Power-split settings.

8.4.1 Electric motor sizing

The main parameter that defines its mass and volume is the maximum engine power demand during operation, which coincides, in this case, with the PS fraction. Having at hand also the design rpm of the low pressure spool, set at 4500 rpm, and its maximum rotational speed (about 5200 rpm), the overall dimensions of the machine can be computed.
For what concerning motor architecture, a three phases one pole pair configuration is adopted. The choice of two poles lies in the fact that these machines are more efficient and lighter if compared to a multi-poles ones, such as a four or eight poles architecture. In addition, view that the rotational speed is inversely proportional to poles' number, these motors can run at higher rpm to produce the same amount of torque required, and thus they can be kept more compact, saving weight and volume. Furthermore, other two considerations have to be done; the first is that in this case, a two poles configuration performs better with the level of power it has to manage. The second, on the other hand, is related to the starting torque; since rotor radius and stator mass increase with the number of poles, a four poles motor requires a higher starting torque with respect to the two one in order to begin rotate, and this can impact battery sizing. Also the cooling characteristics are quite different: one pole pair configuration requires less air, while increasing this number, the design change and a cooling system with proper control of hotspots is mandatory. Summing up, due to the reduced costs and massive increase in efficiency of frequency converters (PMAD), it is often more economical and efficient to run a faster motor and to slows it down, rather than utilizing a massive machine and to speeds it up. The other parameters necessary for completely define the sizing process are strictly related to motor type and architecture other than from manufacturers experience. Tables 6.10 and 6.12, reported these data used for conventional design.
The table below (tab:8.4) summarizes the main geometrical parameters coming out from the sizing process, along with the mass of the different parts.

PS	5%	10%	15%	20%
D_{core} [m]	0.181	0.182	0.182	0.183
D_{rotor} [m]	0.131	0.132	0.132	0.133
D_{shaft} [m]	0.113	0.113	0.113	0.113
D_{tot} [m]	0.420	0.421	0.422	0.423
L_{rotor} [m]	0.546	1.091	1.637	2.183
L_{tot} [m]	0.568	1.114	1.660	2.205
m_{arm} [kg]	17.310	21.447	25.618	29.821
$m_{magnets}$ [kg]	18.575	32.334	46.203	61.156
$m_{rotor} + m_{shaft}$ [kg]	44.675	87.793	130.994	174.264
$m_{service}$ [kg]	18.131	35.396	52.726	70.106
m_{stator} [kg]	35.096	60.404	85.813	111.286
m_{motor} [kg]	133.787	237.374	341.354	446.633

Table 8.4. Electric motor sizes for different power split.

One can see that the most relevant geometrical changes come from the motor length ($L_{motor} \propto P$), whereas the external diameter (which includes the casing too) remains almost constant (little changes are due to air gap increment with power), and this can help if the integration process is considered. In fact, view that the electric motor has to be fastened in line with the gas-turbine engine, a smaller frontal section does not let aerodynamic drag to grows up. Of course, the machine can be installed on-board too and connected to the low pressure spool by means of a mechanical transmission, at the expense of further losses coming from gimbals and gears.
Concerning mass, the greatest contribution derives from the rotor and the shaft, which is responsible of torque transmission, and so has to be strong and fast. The other relevant component is the stator, which accounts for approximately 25% of the total weight, while the remaining parts contribute for less than 15%.
Once the geometry is known, it is possible to compute losses, and hence efficiencies, as reported in the following figures, which highlight their trend as a function of the power output.

- PS=5%

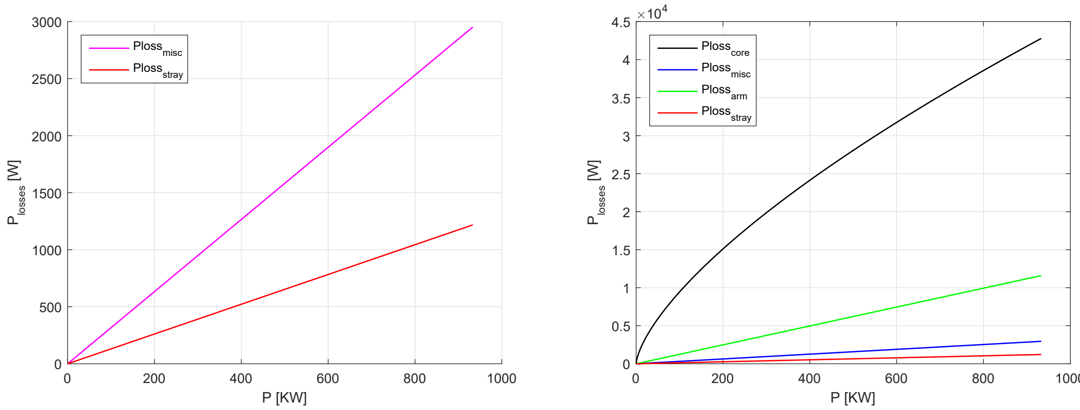

Figure 8.8. Motor losses breakdown PS=5%.

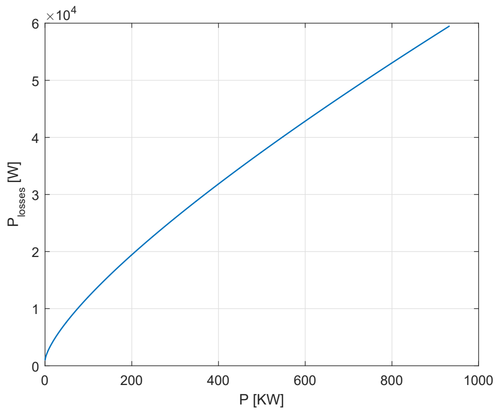

Figure 8.9. Motor total losses PS=5%.

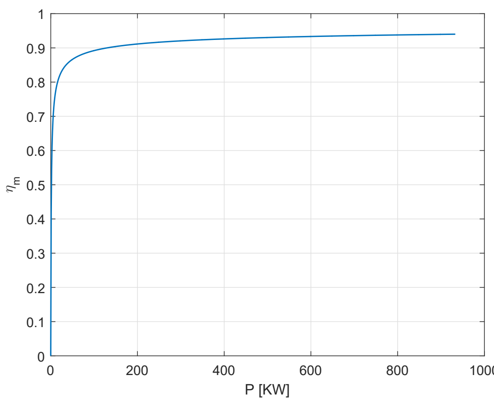

Figure 8.10. Motor efficiency PS=5%.

- PS=10%

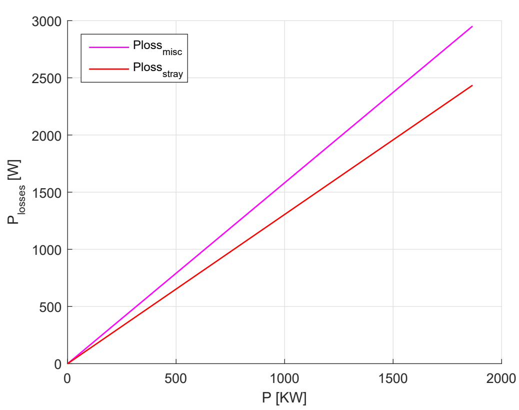

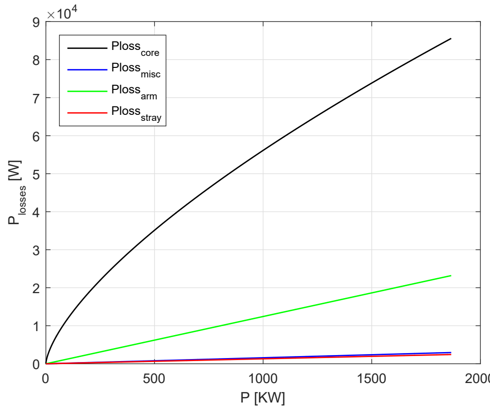

Figure 8.11. Motor losses breakdown PS=10%.

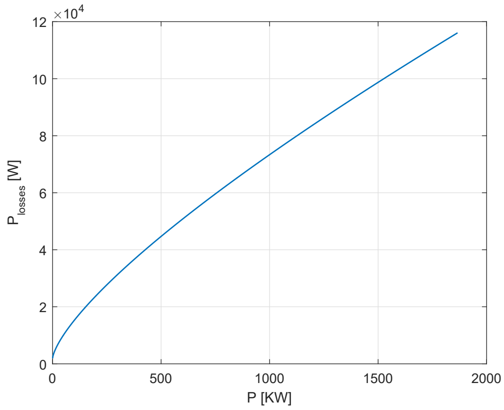

Figure 8.12. Motor total losses PS=10%.

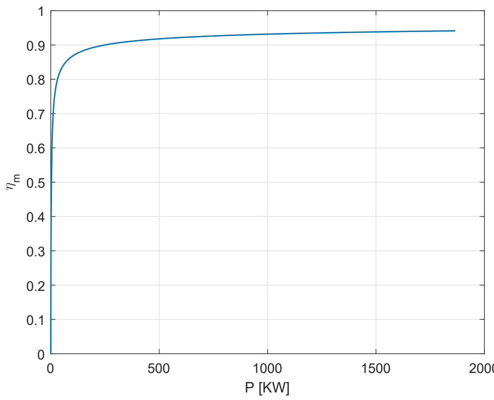

Figure 8.13. Motor efficiency PS=10%.

- PS=15%

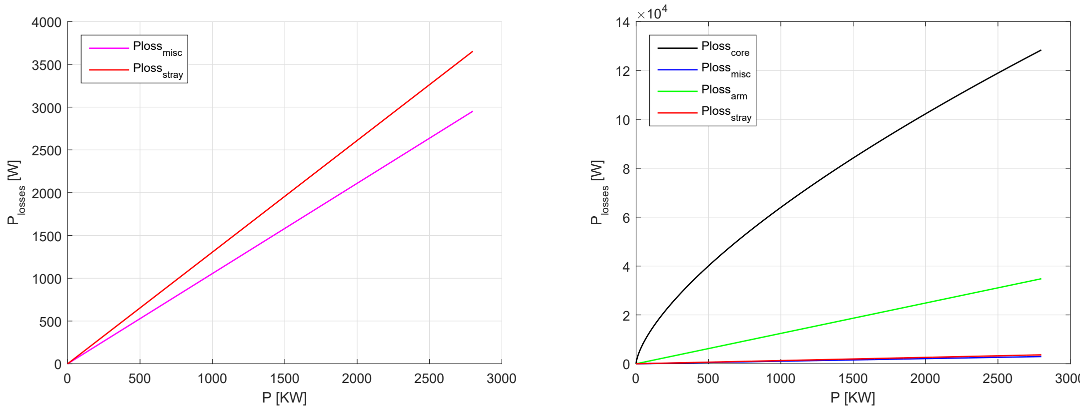

Figure 8.14. Motor losses breakdown PS=15%.

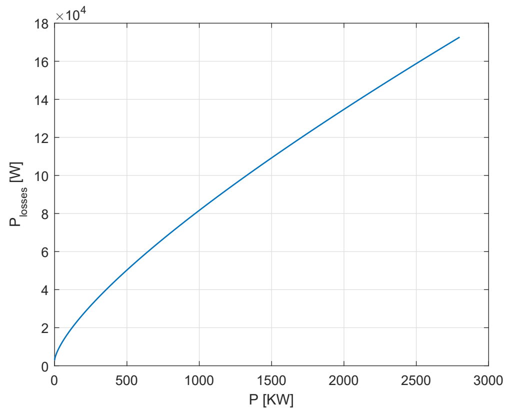

Figure 8.15. Motor total losses PS=15%.

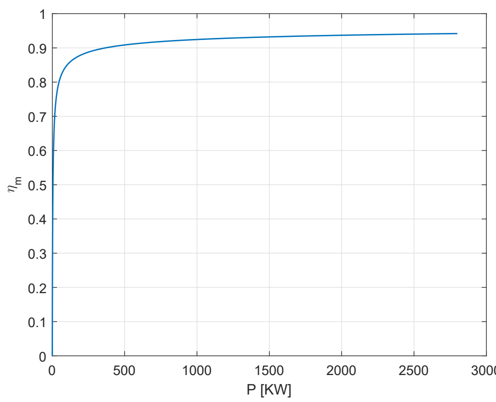

Figure 8.16. Motor efficiency PS=15%.

- PS=20%

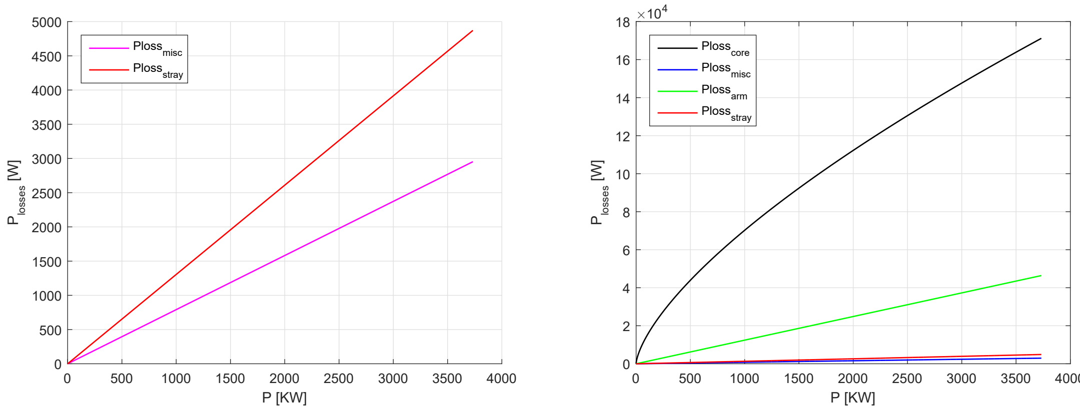

Figure 8.17. Motor losses breakdown PS=20%.

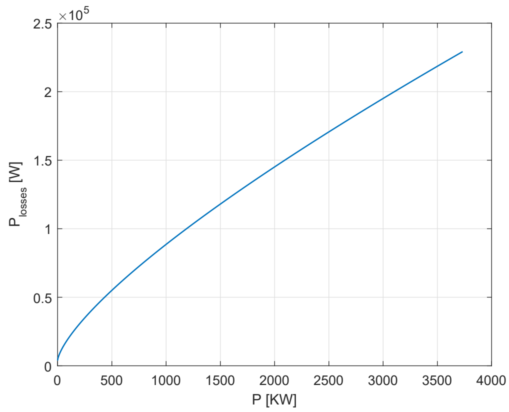

Figure 8.18. Motor total losses PS=20%.

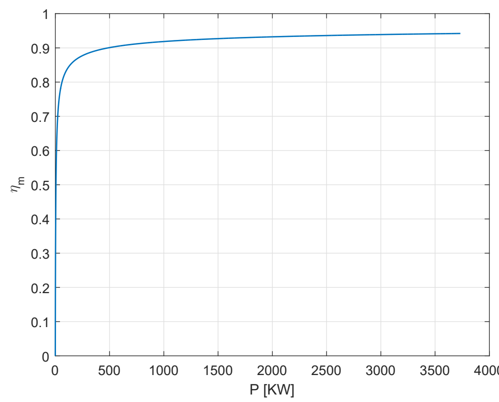

Figure 8.19. Motor efficiency PS=20%.

Table 8.6 summarises total losses and efficiency values for the different power-split configurations adopted.

PS	5%	10%	15%	20%
total losses [W]	59516.352	116080.689	172645.027	229254.917
η_{motor}	0.943	0.942	0.941	0.940

Table 8.6. Motors' efficiencies and total losses.

One can appreciate that losses raise as power increases. In fact, as outlined during model's description, these are directly related to torque and rotational speed, which are synonyms of power ($P = T \cdot \omega$). The main contribution comes from the core losses, which take into account hysteresis effects, followed by the armature ones, directly related to the heat dissipated in coils and windings. The remaining, i.e the miscellaneous and the stray ones, are negligible if compared to those mentioned above, and share of only few percentage points. Talking about efficiency, they are quite high, as expected from this kind of AC machines, and remain almost constant for each power-split mode.

8.4.2 Power converter sizing

The sizing process is more or less the same as that described for the electric motor. The module is dimensioned in order to be successful in managing peak power demands, namely that defined by the power-split parameter. A voltage of 3000 V is taken as nominal line value: this choice, as it will be further explain in subsection 8.4.3, comes from the necessity of reducing current magnitude, so as to limit losses and electromagnetic compatibility effects, raising performance.
For what concerning diodes and transistors electrical parameters, such as reference and maximum current and voltage, manufacturers' data are taken as a guideline [72] and are reported in table 6.2 and 6.4.
In the following figures, main components' losses, total losses and efficiency trends are plotted against power requirements.

- PS=5%

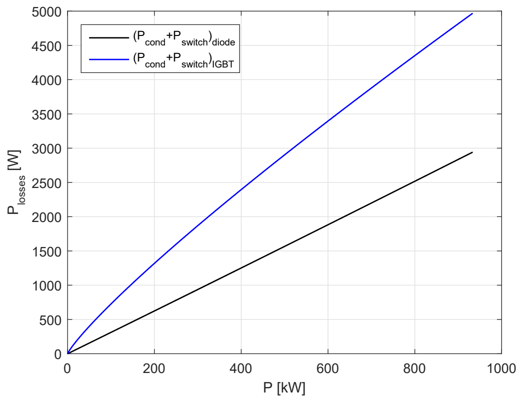

Figure 8.20. Inverter components' losses PS=5%.

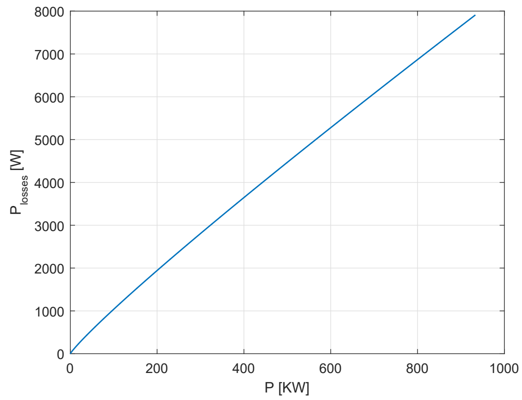

Figure 8.21. Inverter total losses PS=5%.

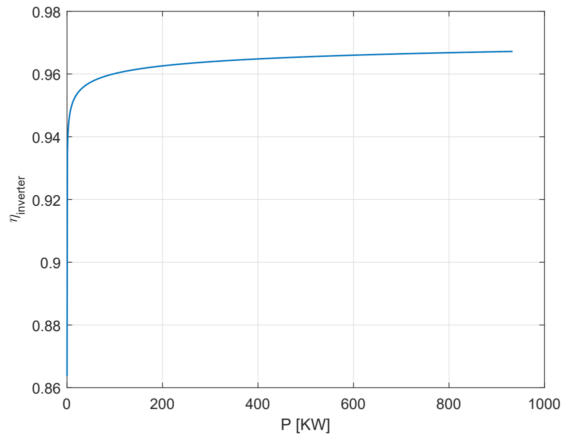

Figure 8.22. Inverter efficiency PS=5%.

- PS=10%

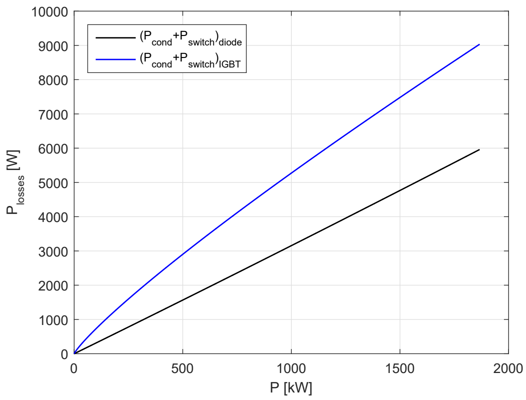

Figure 8.23. Inverter components' losses PS=10%.

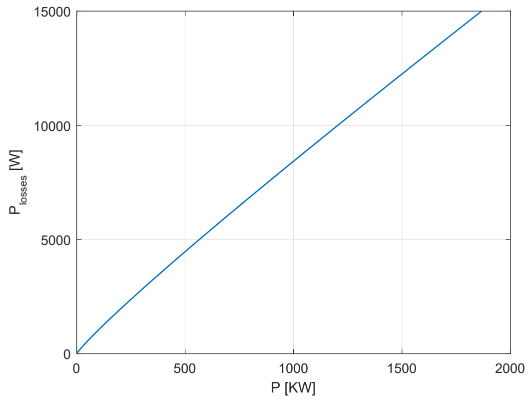

Figure 8.24. Inverter total losses PS=10%.

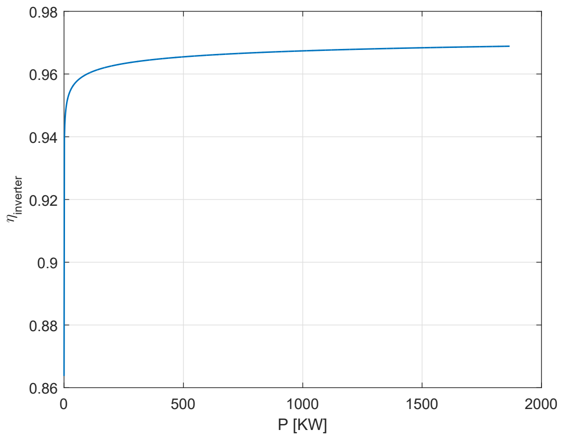

Figure 8.25. Inverter efficiency PS=10%.

- PS=15%

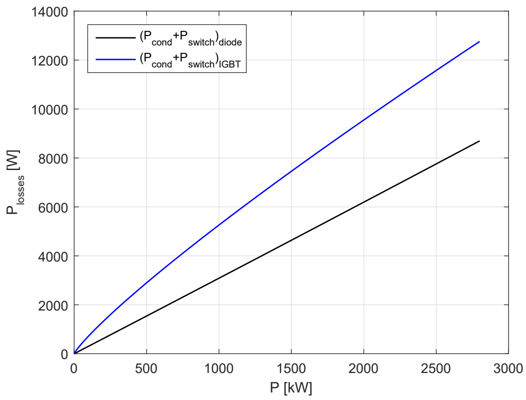

Figure 8.26. Inverter components' losses PS=15%.

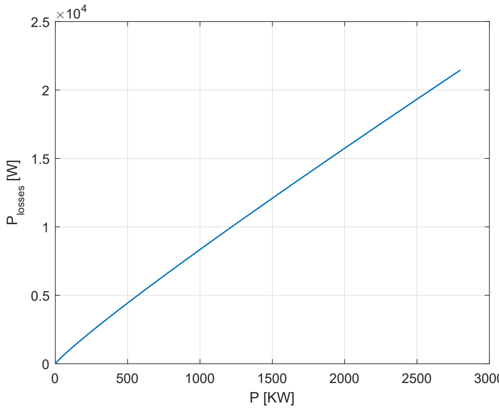

Figure 8.27. Inverter total losses PS=15%.

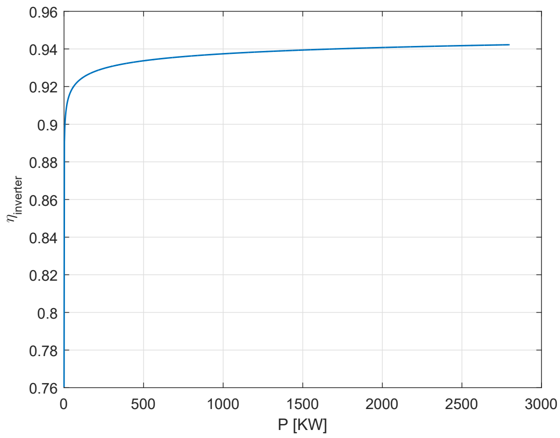

Figure 8.28. Inverter efficiency PS=15%.

- PS=20%

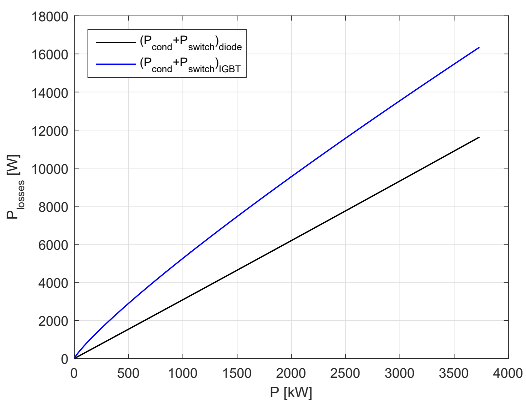

Figure 8.29. Inverter components' losses PS=20%.

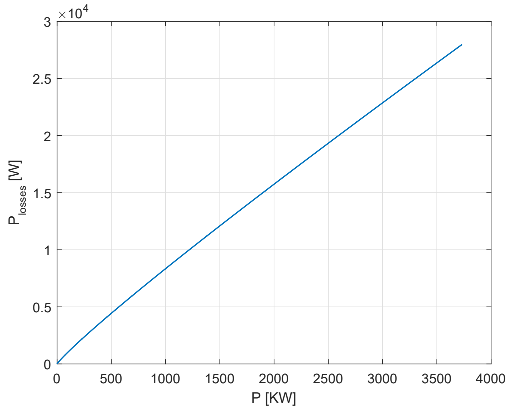

Figure 8.30. Inverter total losses PS=20%.

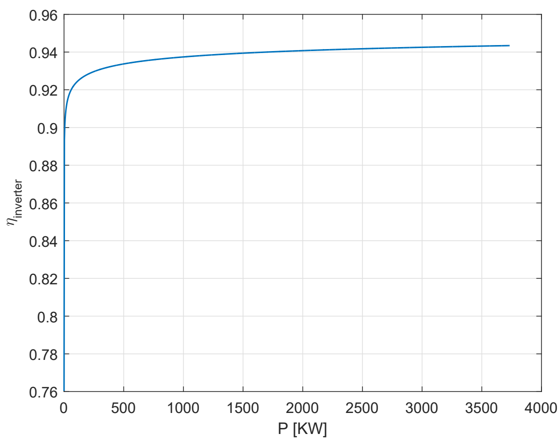

Figure 8.31. Inverter efficiency PS=20%.

Table 8.8 summarises the most meaningful parameters coming from the sizing procedure, among them the total weight, something that is of particular importance for the simulation process.

PS	5%	10%	15%	20%
P_{losses} [W]	8064.701	15244.941	21838.090	28453.160
η_{inv}	0.969	0.967	0.943	0.941
$m_{inverter}$ [kg]	326.659	653.318	979.977	1306.636

Table 8.8. Power converter main parameters.

As for the motor, losses raise with power. Stating that $P = V \cdot i$ and for the case of constant line voltage, one can observe that current increases proportionally with "P". As a consequence, Ohm effects become ever more important ($P_{Ohm} = R \cdot i^2$) and the heat dissipated by transistors and diodes boosts. This directly results in an efficiency jump, which decreases from 97% to less than 95%. Moreover, the reason of this efficiency drop between PS=10% and PS=15% relies on switches limiting current. In fact, as it happens in this case, when this value is exceeded, in order to lower the tied and avoid damages, another module is connected in parallel and this addition immediately reflects on efficiency (see eq.6.30).
Giving to speak of mass, this is an actual scourge that affects their performance. Despite the introduction of new components, such as SiC miniaturized transistors, the power density still remains low, and this will severely affect, just like batteries, the aircraft electrification process.

8.4.3 Batteries sizing

Again, the sizing procedure starts from the power profile of figure 8.7 and by considering the different power-split conditions along all the segments analysed. The sizing process has to take into account losses which occur along the line, from the source to the load; for this reason, a transmission efficiency parameter is introduced, defined as the product of the main components' efficiency.

$$\eta_{tr} = \eta_{bat} \cdot \eta_{inv} \cdot \eta_m$$

Since storage system efficiency is unknown, an initial value is guessed and it is then updated during a second iteration, till convergence.
Going on, in order to obtain batteries' weight it is necessary to compute their capacity, by integrating power requirements in time.

$$C_{tot} = \int_0^t \frac{P(t)}{\eta_{tr}} dt$$

From here, the mass is calculated assuming a typical Li-ion battery energy density of 200 $\frac{Wh}{kg}$ and an additional factor $k_{add} = 1.15$ for what concerning wirings and casings.

$$W_{bat} = \frac{C_{tot}}{\rho_{bat}} \cdot k_{add}$$

Results are summarized in table 8.10, reported hereafter.

PS	C_{tot} [kWh]	W_{bat} [kg]
5%	461.823	2655.483
10%	923.646	5310.965
15%	1385.469	7966.448
20%	1847.292	10621.930

Table 8.10. Battery weight and capacity for different power-split.

Even if the segment which is going to be partially electrified takes only a small amount of time, if compared to the overall mission, one can observe that the mass which is going to be added on the plane is nothing but negligible, considering also the fact that these values refers to one single engine, and so has to be doubled for a twin engine aircraft.
Once the global variables has been defined, it is possible to progress with the electrical sizing, i.e define the number of cells to put in series, the amount of modules to connect in parallel and the number of packs. A nominal 3000 V line voltage is chosen, so as to keep tide values within an acceptable limit, thus reducing interferences, line dispersions and Ohm losses. Same reasons lead to split batteries in more than one pack when considering $PS > 5\%$, with the advantage of partially increase efficiency too. In addition to this, the state of charge at the end of the climb phase might be grater than 20%, in order to prevent electrodes' damages. For safety reasons, the lowest limit is set to $SOC = 25\%$, and this +5% margin can be seen as a sort of safety factor.
Riding back for a moment, it has been stated that current has to be kept as low as possible so as to minimize losses. In order to explain this concept in a more detailed way, some charts are reported hereafter; they show tide and efficiency trends for many power split configurations, other than in function of different battery packs' number. Analysing the trends, one can see that increasing electrical power leads to currents which are absolutely extremely high. A direct consequence, as can be visible in the plots, is a remarkable efficiency drop, caused by the huge amount of losses produced. Furthermore, such high values are not consistent in terms of safety, especially if installed closed to other aircraft subsystems; in fact,

heat transfer and electromagnetic compatibility issues can arise, further complicating the overall design and integration process. Furthermore, cables' size will increase due to additional insulating material that must be added, thus further increase their mass. In short, maximum current values must be kept lower, and this is done dividing battery modules in more than one pack, according to electrical engineering laws. In this way, Ohmic losses drops down and greater efficiencies are to be expected. On the other hand, adding too many packs will result in additional complexity and will increase the number of connections. Therefore, a compromise has to be done, so as to balance all this aspects.

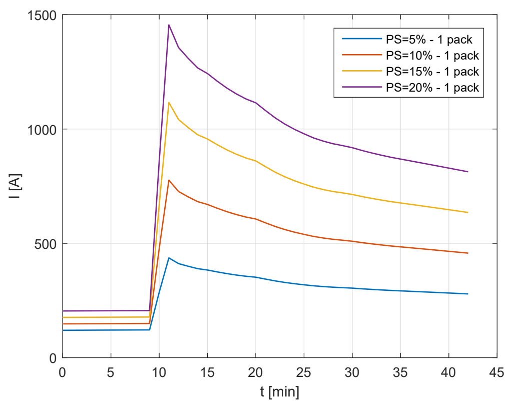

Figure 8.32. 1 battery pack current for different PS.

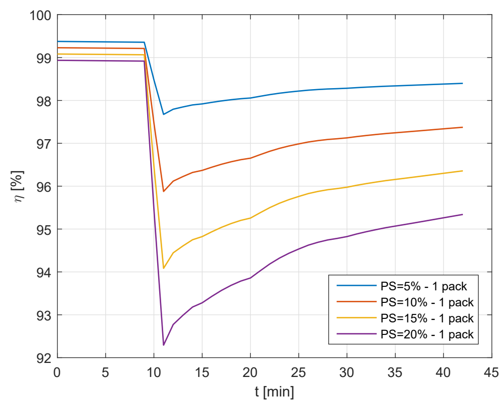

Figure 8.33. 1 battery pack efficiency for different PS.

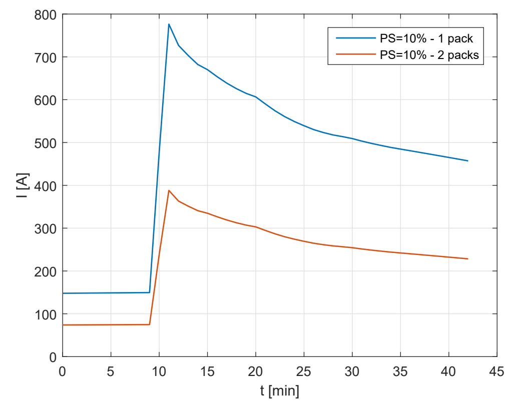

Figure 8.34. Current for n-battery packs - PS=10%.

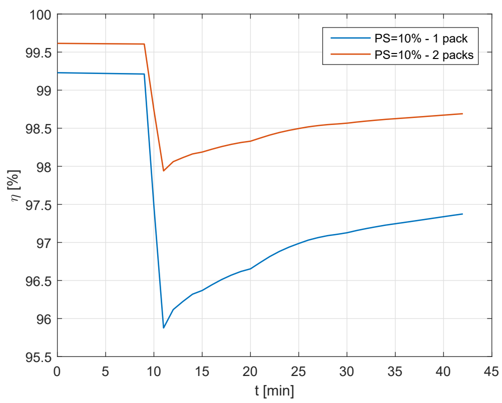

Figure 8.35. Efficiency for n-battery packs - PS=10%.

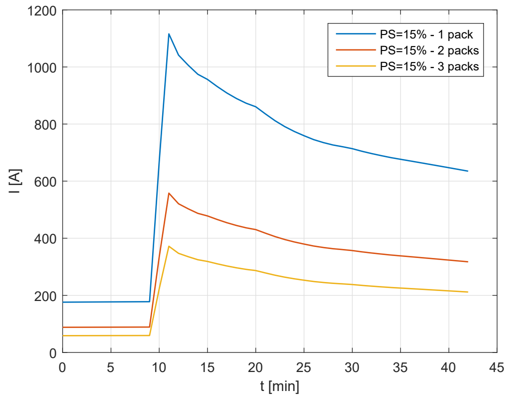

Figure 8.36. Current for n-battery packs - PS=15%.

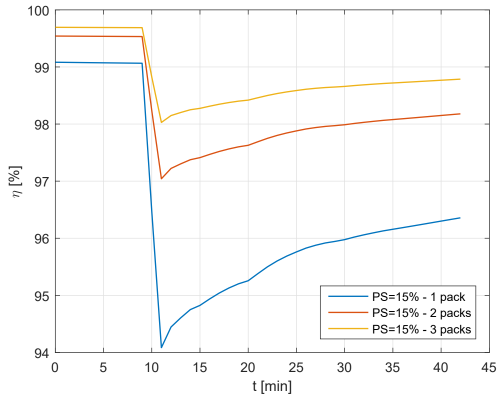

Figure 8.37. Efficiency for n-battery packs - PS=15%.

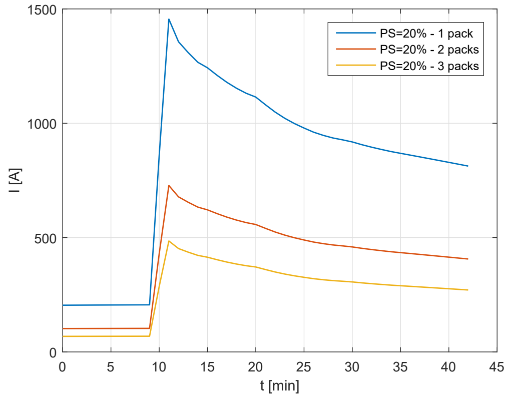

Figure 8.38. Current for n-battery packs - PS=20%.

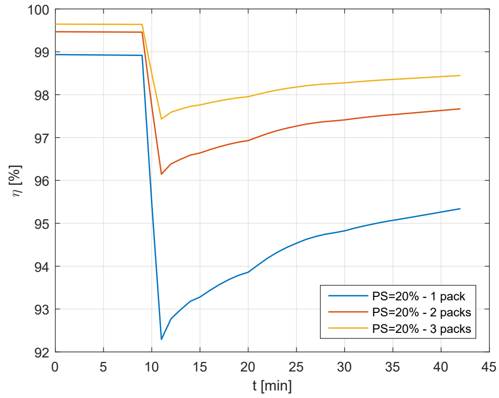

Figure 8.39. Efficiency for n-battery packs - PS=20%.

The following table summarises the variables of interest coming out from the model used, along with the number of battery packs chosen as a compromise for an acceptable outcome.

PS	5%	10%	15%	20%
$n°$ packs	1	2	3	3
$n_{cell_{series}}$	800	800	800	800
$n_{cell_{parallel}}$	5800	4900	4550	5880
$n_{cell_{tot}}$	$4.6 \cdot 10^6$	$7.84 \cdot 10^6$	$10.92 \cdot 10^6$	$14.11 \cdot 10^6$
I_{max} [A]	437.955	389.779	373.362	487.624
$\eta_{bat_{mean}}$	0.985	0.987	0.988	0.984
SOC_{end}	25%	25%	25%	25%

Table 8.12. Battery output parameters for different power-split.

The set of figures reported herein highlight several electrical variables' trend for the four power-split configurations considered. Since the cell voltage behaviour is unchanged, as well as the voltage drop with time, these two plots are reported only once.

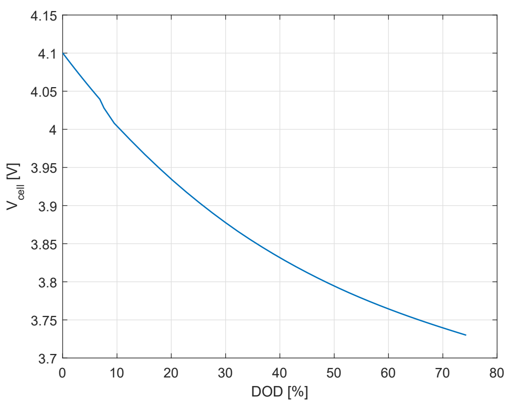

Figure 8.40. Battery voltage-depth of discharge.

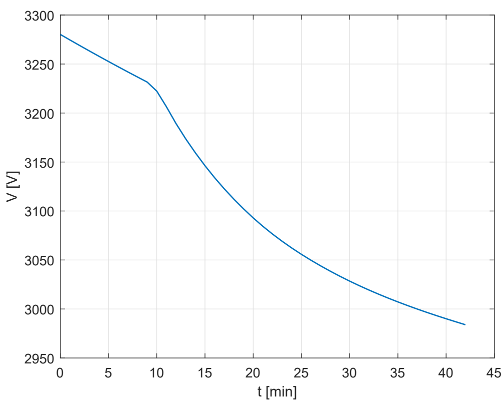

Figure 8.41. Battery voltage-time.

- PS=5%

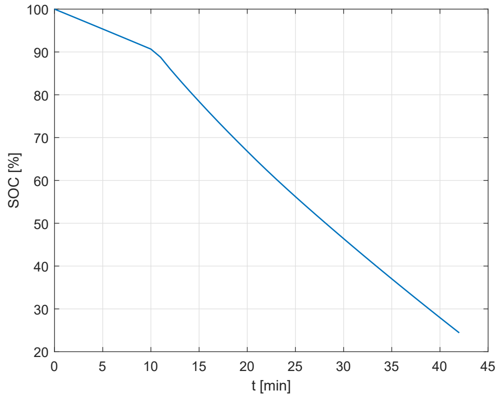

Figure 8.42. State of charge PS=5%.

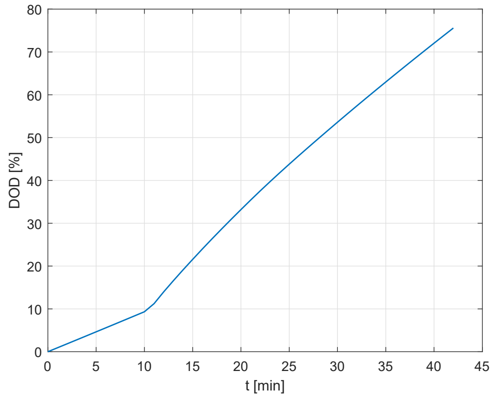

Figure 8.43. Depth of discharge PS=5%.

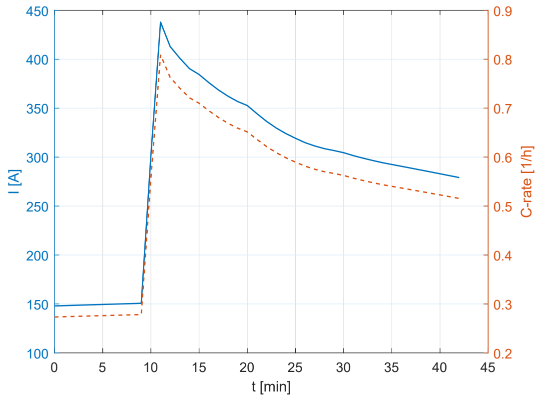

Figure 8.44. Current and C-rate PS=5%.

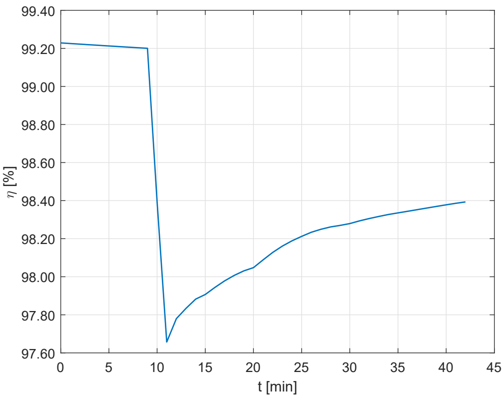

Figure 8.45. Battery efficiency PS=5%.

- PS=10%

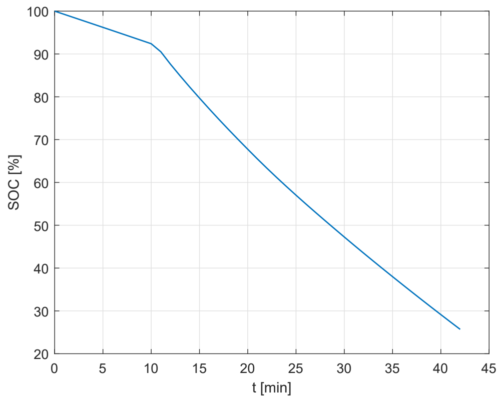

Figure 8.46. State of charge PS=10%.

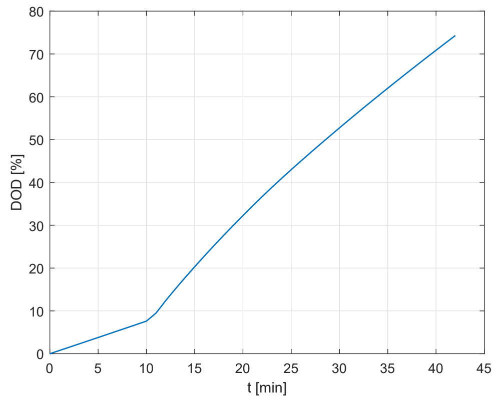

Figure 8.47. Depth of discharge PS=10%.

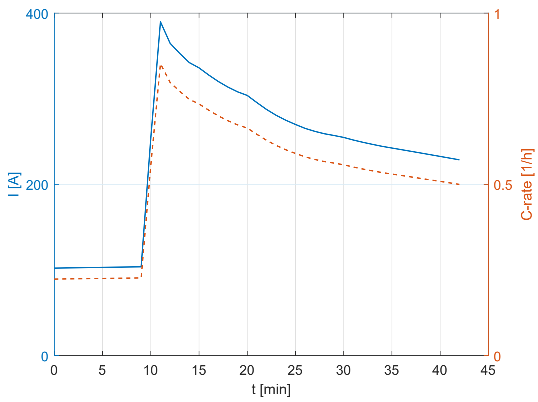

Figure 8.48. Current and C-rate PS=10%.

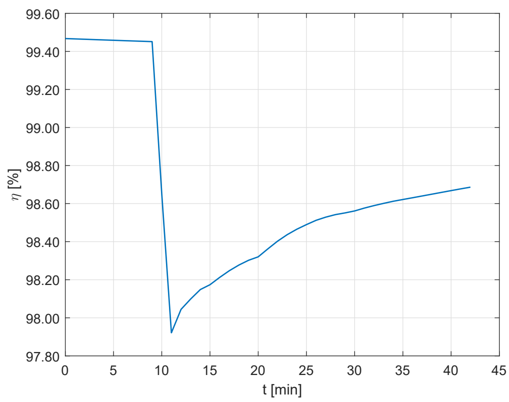

Figure 8.49. Battery efficiency PS=10%.

- PS=15%

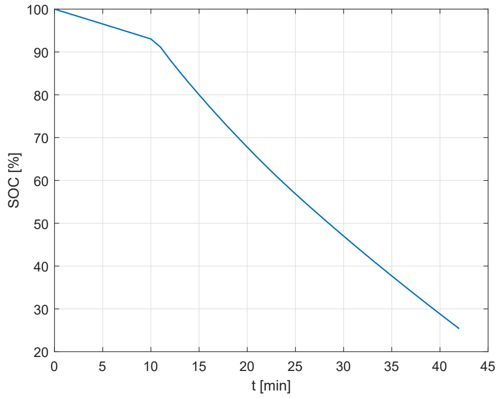

Figure 8.50. State of charge PS=15%.

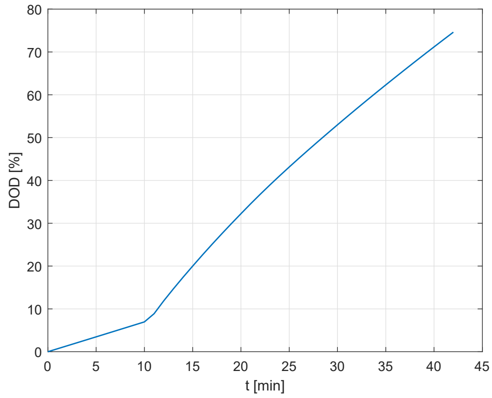

Figure 8.51. Depth of discharge PS=15%.

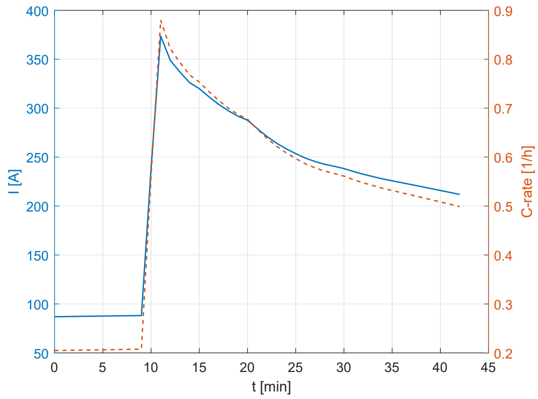

Figure 8.52. Current and C-rate PS=15%.

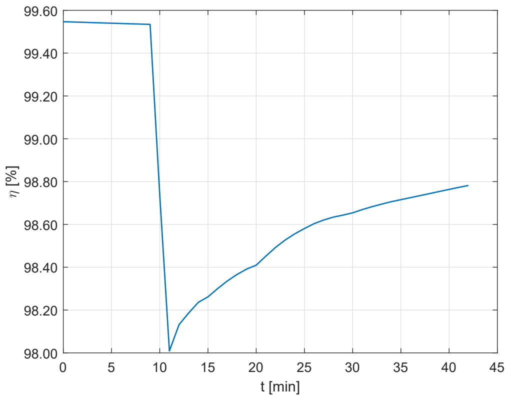

Figure 8.53. Battery efficiency PS=15%.

- PS=20%

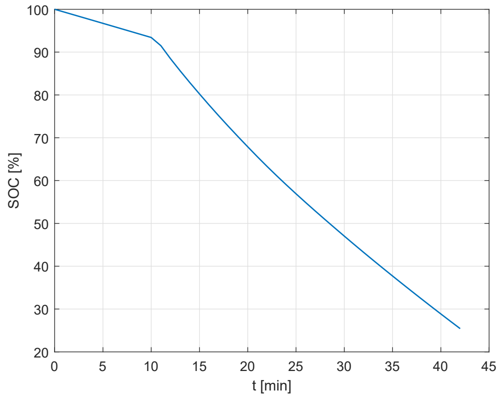

Figure 8.54. State of charge PS=20%.

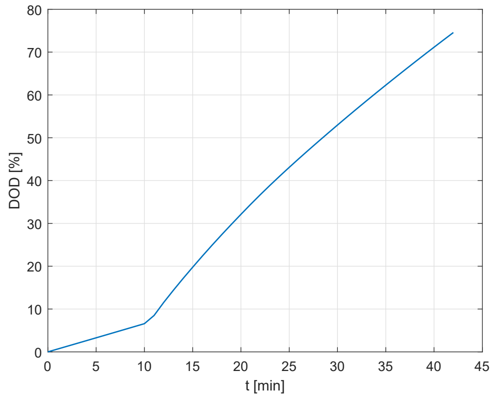

Figure 8.55. Depth of discharge PS=20%.

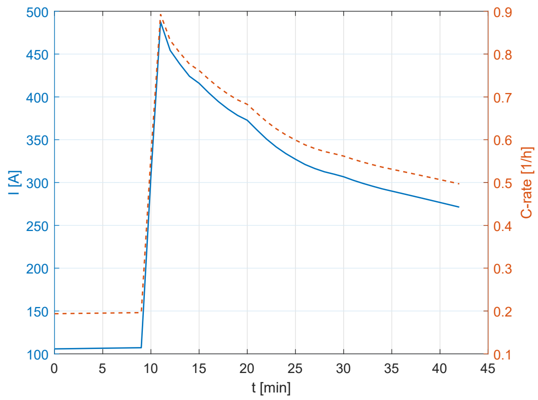

Figure 8.56. Current and C-rate PS=20%.

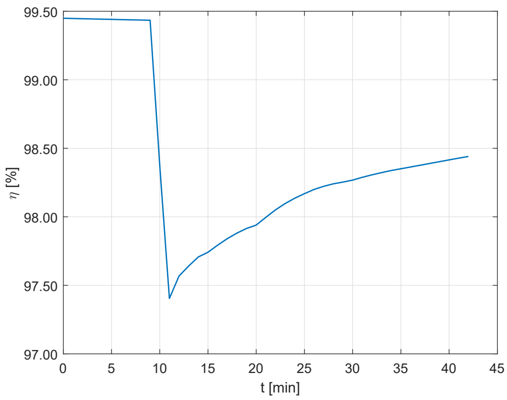

Figure 8.57. Battery efficiency PS=20%.

As can be seen, voltage constantly decreases in a more or less regular basis, depending on the power absorbed by the electrical motor. As a consequence, during peak power demand, current grows in a steepest manner, and the battery discharges more rapidly (C-rate increases). Then, proceeding with the climb phase, the power required reduces with time, and the same happens to tied. Looking at efficiency curves, a dramatically falling appears at take-off, in line with what has been said just now. Then, it rises in a non linear manner, as the LPT power decreases (along with current). One can states that their trends are inversely proportional.

8.5 Sensitivity analysis

In this brief paragraph, few considerations relating weight with actual and future technology are exposed, in order to see possible differences and improvements.
Summing up components weight, the total drive train mass is obtained for each power split configuration (fig.8.58), whereas figure 8.59 shows relative weight breakdown percentage.

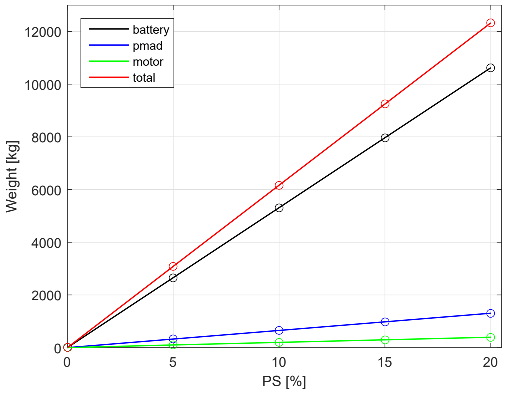

Figure 8.58. Weight trend for different PS.

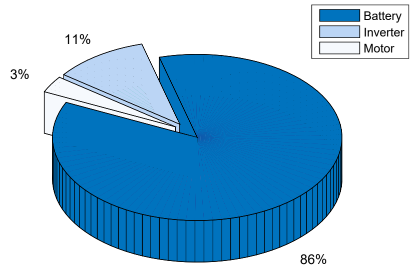

Figure 8.59. Weight breakdown.

It is evident that batteries are the preponderant part, engraving for 86% on the total train mass. This is due to their low power density, which puts them bulky and heavy, making it impossible to electrify an aircraft over a predetermined level. That is why scientists are trying to raise batteries' capacity, improving current technology or developing new ones. If energy density will increase, and considering same output requirements, weight will drop and the road towards a full hybridization would become more feasible, fully reaping all the potentialities electricity brings with.
The following table compares actual storage system technology and weight with those assumed for future aircraft concept developments. A graphical representation is also reported in fig.8.60.

ρ_{bat} $[\frac{Wh}{kg}]$	200	500	1000	1500
PS	weight [kg]			
5%	2655.483	1062.193	531.097	354.064
10%	5310.965	2124.386	1062.193	708.129
15%	7966.448	3186.579	1593.290	1062.193
20%	10621.930	4248.772	2124.386	1416.257

Table 8.14. Battery weight-energy density.

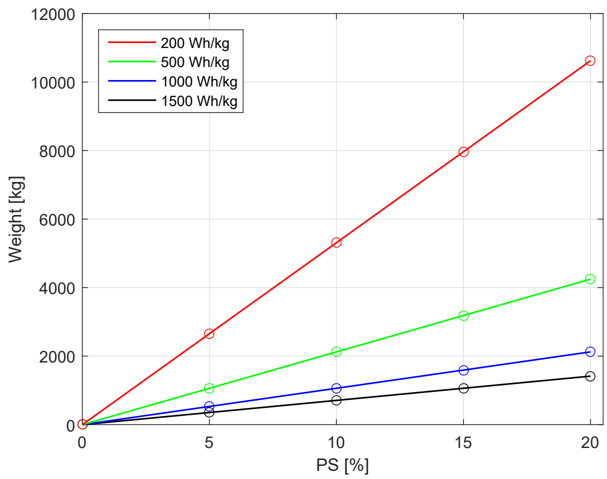

Figure 8.60. Battery weight function of energy density.

Taking reference to the test case developed, an increase in energy density from 200 $\frac{Wh}{kg}$ to 500 $\frac{Wh}{kg}$ would reduce battery weight by 60%, while a further increment up to 1500 $\frac{Wh}{kg}$ would lead to a weight saving of almost 86%. In this way, the take-off and climb phases could be fully electrified, and the cruise segment too. As a consequence, fuel consumption would drop to zero, and the gas-turbine engine would be replaced by more efficient electric-driven fans. At this point, in order to further improve efficiency, the blended wing-body configuration and the concept of distributed propulsion would come into play.
To see the effects on the aircraft itself, the maximum take-off weight is plotted against power-split settings, for different battery energy density (fig.8.53). MTOW includes, in this case, also the e-train mass, i.e that of accumulators, power converters and motors. With 20% power split and state of the art technology (200

$\frac{Wh}{kg}$), additional 24.65 tonnes have to be carried up, and this is a huge amount of weight, whereas, if considering an energy density of 500 $\frac{Wh}{kg}$, the MTOW would grow approximately only by the half part, i.e 11.9 tonnes. From this short analysis, it is possible to conclude that the hybridization process of large airplanes will take advantages only if accumulators' systems will increase their capacity, so as to perform the same tasks with an incredible mass saving.

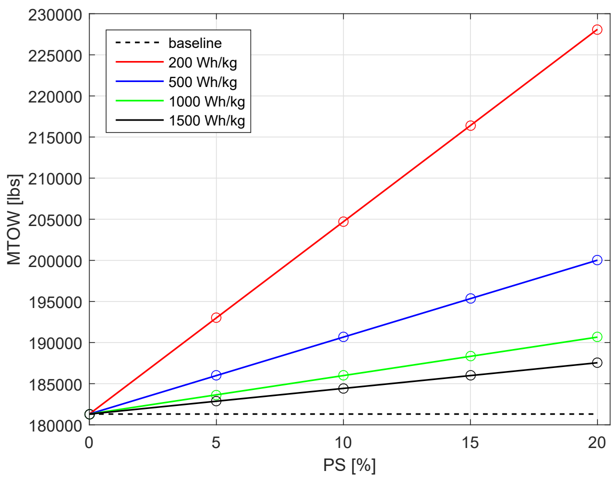

Figure 8.61. MTOW-PS for different energy density.

Same trends are highlighted in the following for what concerning power converter and electrical motor.

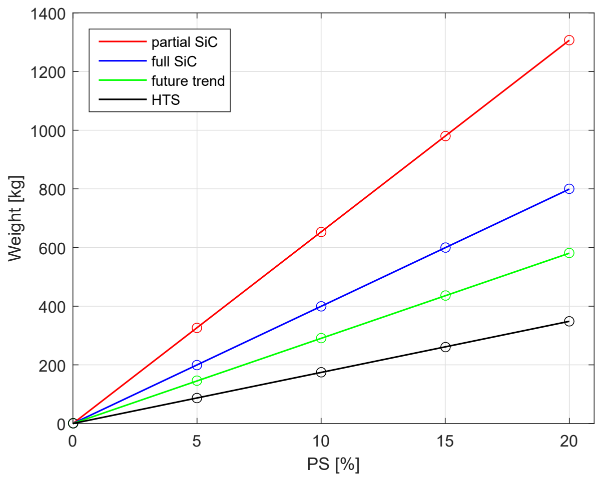

Figure 8.62. Inverter weight-PS for different power density.

Inverters suffer from a very low power density, which makes them extremely heavy and bulky. SiC technology raises the kilowatts per kilo up to 6.54, whereas future trends tend to go higher, till 9 $\frac{kW}{kg}$. Further improvements will come introducing high temperature superconducting technology, which is expected to reach an extremely outstanding performance, not comparable with predecessors. In fact, 15 $\frac{kW}{kg}$ are claimed, which will make more feasible the hybridization process.
Dealing with motors and looking on what is going on, trends are much more optimistic. Nowadays, power density range from 5 to 9 $\frac{kW}{kg}$: for example, the ElectriFly GPMG4805 brushless motor has 5.68 $\frac{kW}{kg}$, the Yasa 400 reach 6.87 $\frac{kW}{kg}$, while the Emrax 228 claims 10 $\frac{kW}{kg}$. Looking at the future, especially to HTS technology, the few tests-bench performed and experts estimate an increment up to 15 $\frac{kW}{kg}$ for a partial HTS architecture, in which only the rotor works at cryogenic temperature, whereas for full HTS motors the values into play seems to almost double. Of course, these improvements will lead to ameliorate not only the electric train performance, but also the aircraft one, as components would be subjected to a dramatically reduction both in losses and mass.

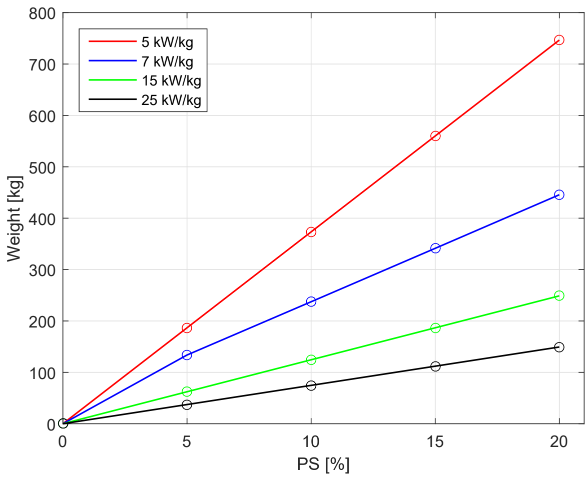

Figure 8.63. Motor weight-PS for different power density.

8.6 Simulation and results

In the following section, the simulation process is explained and results showed up. To run it, the engine model made with Turbomatch is integrated within the plane one in Flops and a first mission is flown. Then, other four missions were set up, one for each power-split configuration; the additional mass coming from the introduction of the electrical drive-train is taken into account increasing aircraft total weight (more specifically, this quantity is added to the structural weight parameter). In this way, as the percentage of power introduced by the external source raises, the airplane becomes heavier and the software computes fuel consumption accordingly. There are still few things to say about simulation settings. The first is that with partial hybridization, the climb phase is usually longer than the conventional one, the rate of climb is lower and so it may takes more time. In addition to this, as fuel burning is of primary importance in this analysis, the software is set to the minimum fuel-to-climb mode, with the first throttle cutback at about 690 ft. Finally, lasts settings concern optimum altitude and flight Mach number, defined at 35000 ft and 0.82 respectively.
Results and further considerations are presented in the remaining part of this section. As already mentioned, the analysis focus on take-off and climb phases.
Figure 8.64 shows the low pressure turbine power profile as function of altitude, while figure 8.65 plots the same variable against climb time. The other curves refers to the hybridization cases, where a percentage of the power required is given by the electric train (data refers to one engine).

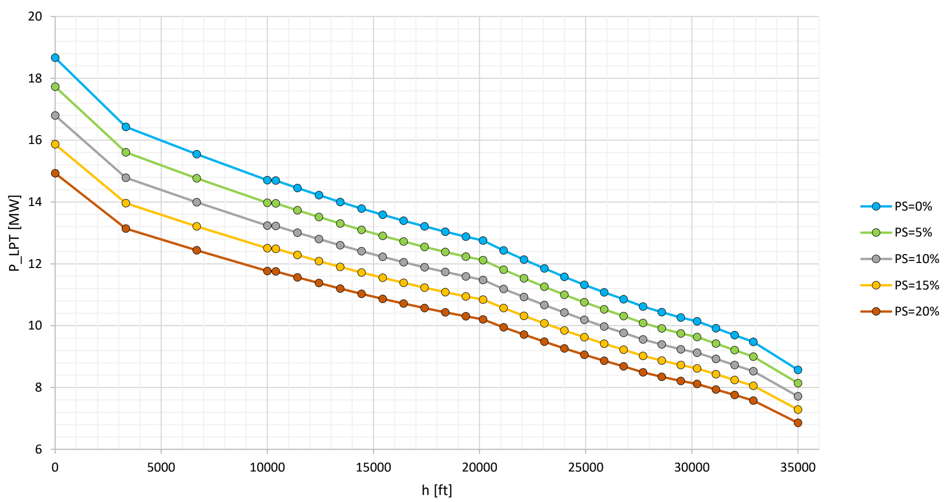

Figure 8.64. LPT power-altitude.

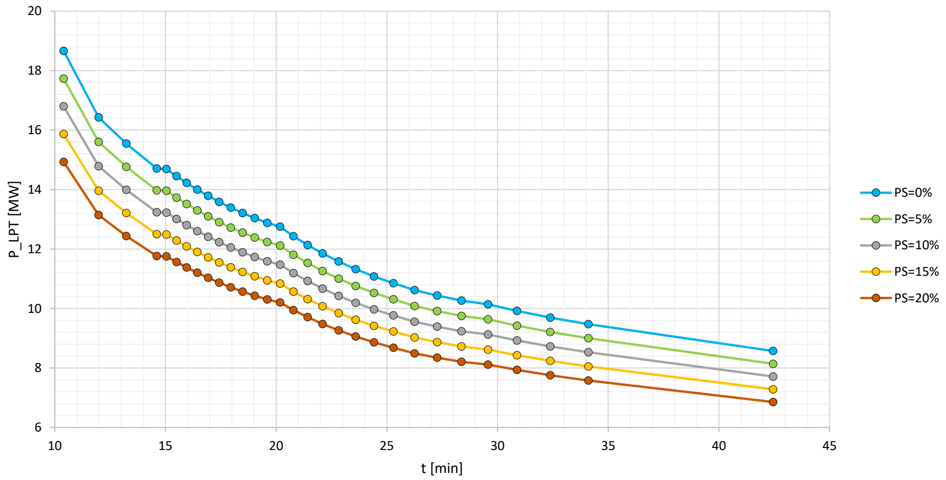

Figure 8.65. LPT power-time to climb.

During ground manoeuvres, the turbofan runs only a bit over idle conditions, and the power developed by the low pressure turbine is tiny (less than 3 MW per engine). This segment is not represented on charts, and can only be appreciated by the fact that the time axis of fig.8.65 has its minimum value set at 10 min.
The maximum power requirement, as stated in previous sections, is during take-off, where the gas-turbine engine could even overspeed by a certain amount. This phase also corresponds to the high thrust one, as the aircraft has to accelerate and lift-off. During the climb segment, on the other hand, altitude increases and air density decreases. As a consequence, the mass flow rate injected by the inlet is less if compared to that at sea level, thrust diminishes and the power generated by the LPT reduces as well, until cruise altitude is reached.
The time to climb may look too long, but, as the minimum fuel-to-climb option is set in Flops, this last has optimized the rate of climb, and thus the time, in order to have the least kerosene consumption. That is the reason why about 30 minutes are needed to fly from the ground to 35000 ft.
Figure 8.66, on the other hand, displays the quantity of fuel consumption per second $\left(\frac{kg}{s}\right)$ and per engine as a function of the LPT power, for various power split settings.

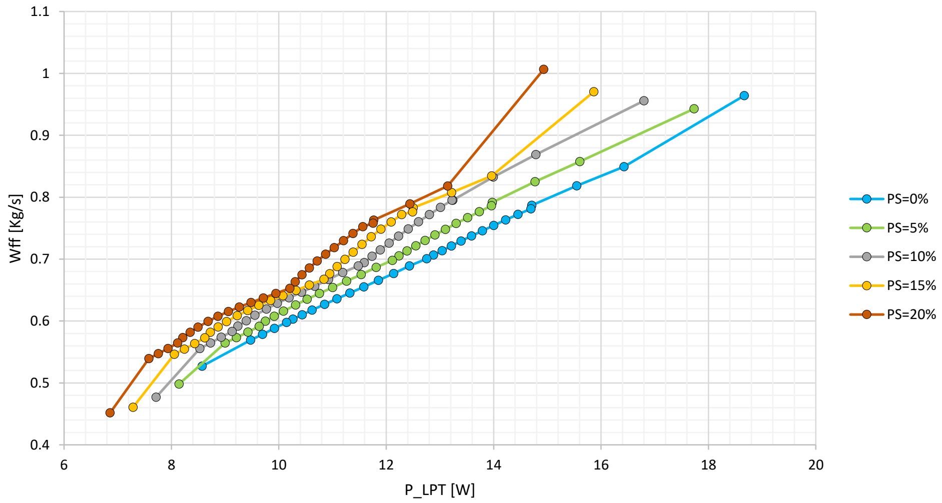

Figure 8.66. Fuel consumption rate-LPT power.

Fuel consumption, as can be seen, is directly related to the power developed. Peak values refers to take-off, while their opposite to the first part of the cruise, immediately after the top-of-climb condition. The 5% power split configuration has the minimum quantity of take-off fuel burn, precisely -2.2% with respect to the conventional kerosene-based aircraft. The additional weight coming from the introduction of batteries and other electrical components does not jeopardise its performance, rather they improve. With a PS=10%, only 0.86% of fuel is saved, whilst further increasing the amount of "electrical power" leads to an opposite trend; in fact, batteries' mass becomes extremely huge enough to increment fuel consumption, even more than that of the baseline airplane (tab.8.16). An hybridization of 20%, which means that 3.7 MW are fed by batteries through an electric motor, leads to +4.4% fuel burn in $\frac{kg}{s}$, in comparison to the PS=0% mode, and the penalty the aircraft receives in terms of MTOW is of 21.24 tonnes. This great amount of mass is the main responsible for the extra fuel consumption during taxi and lift-off phases, and if engines are not powerful enough, there is also the risk of lengthen the take-off run or, worst of all, that the plane does not make it off. One must also keep in mind that the aircraft configuration is kept fixed (same wing surface, aspect ratio, fusolage diameter, horizontal and vertical tail), and so the aerodynamics and the lift it generates remain almost the same.

PS	$W_{ff}\left[\frac{kg}{s}\right]$	$W_{ff}\ [kg]$
0%	0.964	601.598
5%	0.943	588.342
10%	0.956	596.407
15%	0.970	605.506
20%	1.007	628.120

Table 8.16. Take-off fuel consumption-PS.

Because of the importance of fuel consumption as one of the major performance analysis' parameters, other two charts are added below, highlighting its trend in function of altitude (fig.8.67) and time (fig.8.68). Both figures refer to one engine only.

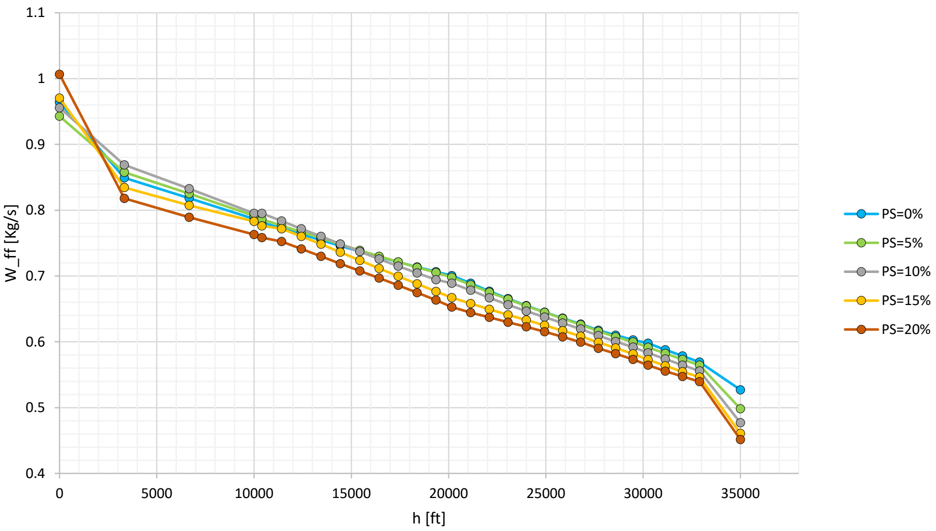

Figure 8.67. Fuel consumption rate-altitude.

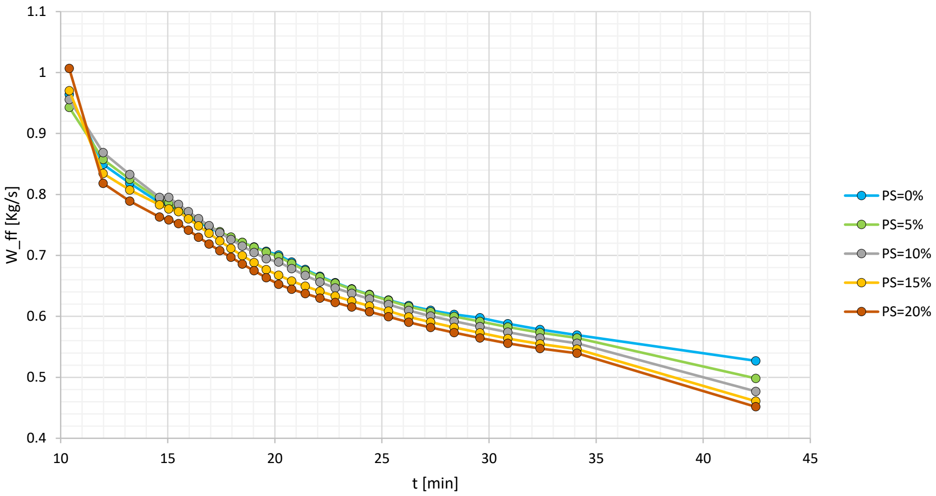

Figure 8.68. Fuel consumption rate-time.

At first glance, one can appreciate the decreasing rate in kilos per second of fuel burnt by the engine as it climbs to higher altitudes. As outlined before, when the quantity of power delivered by the electrical drive-train boosts, the aircraft maximum take-off weight increases because of batteries; apart for the lower power-split settings (up to 10%), the consequence is a direct fuel burn increment, as can be seen for PS=15% and PS=20%. Despite this, during the climb segment batteries and motors play their role and the amount of fuel consumed effectively reduces. The more the power fed by the electrical train, the less the one that has to be produced by the turbine; therefore, less fuel flow is needed and the temperature at the combustor exit can lower a bit. The largest drop in fuel burnt can be seen for the 20% power-split case (first two points on the chart), where more than 3.7 MW are supplied by the "external source". In what concerning the 5% and 10% PS modes, this last is initially higher than the first at take-off and only drops down after a while, crossing the baseline curve. This trend can be understood by remembering weight influences on the overall aircraft performance. In fact, if only the propulsion system is considered alone, there would not be intersections among different PS lines, as the interaction within the airplane would not be considered, and curves would present themselves detached and would follow a similar decreasing trend.
Now, giving to speak of effective consumption during take-off and climb segments, two charts are further added; trends refers to one single engine, but doubling the values one can obtain the aircraft's fuel use as a all.

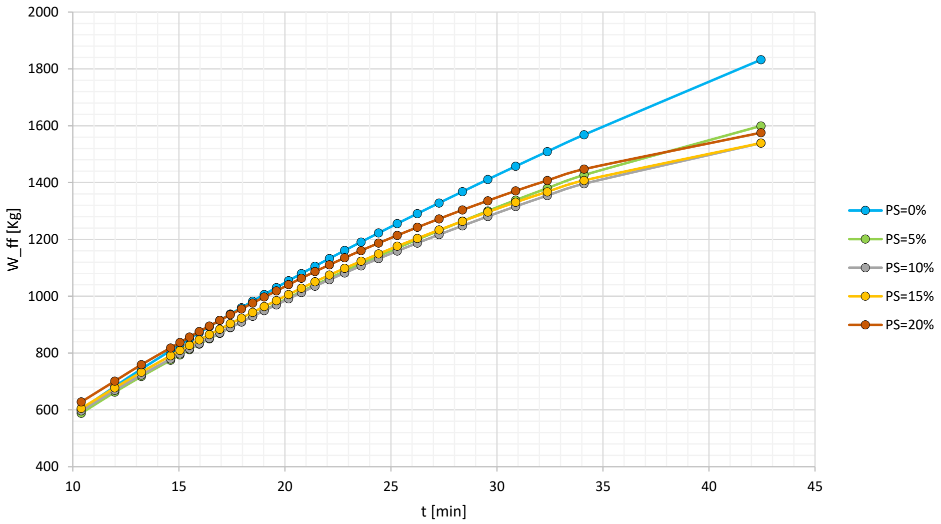

Figure 8.69. Fuel consumption-time.

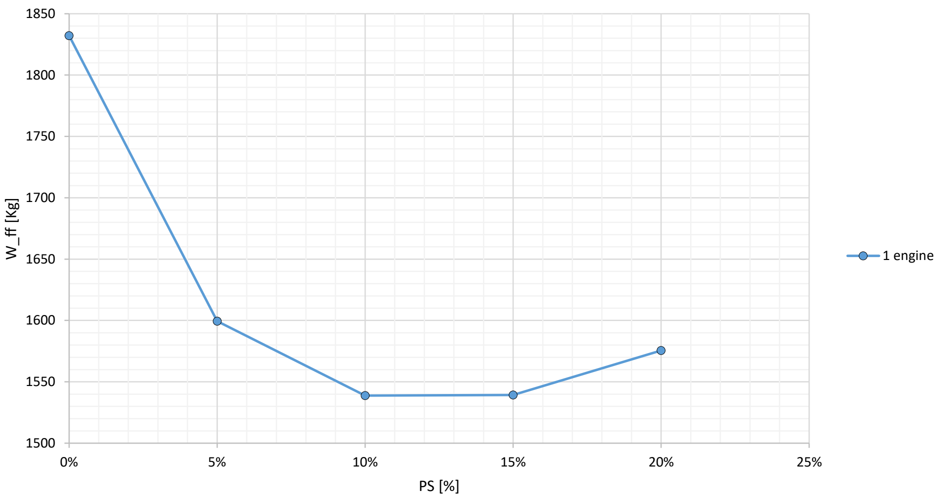

Figure 8.70. Overall climb fuel consumption-PS.

Figure 8.70 shows the total fuel burnt by one engine during the climb phase, for many power-split configurations. The baseline engine in the less efficient and the less environmental friendly one, if compared to its hybridized counterparts. Whatever the amount of power introduced by means of electrical machines, a fall in consumption more or less relevant is evident. With a PS=5%, about 1 MW is introduced from the outside to drive the low pressure turbine, and 12.7% fuel saving is achieved. The peak efficiency point belongs to the 10% hybridization case, in

which an additional 3.8% is attained, for a total kerosene economy of 16%. Further PS increment still brings some benefits in comparison to the baseline architecture, but not as much as it can be expected. For the last two cases, 15.9% and 14% fuel reduction is computed respectively, which is quite a larger quantity. However, benefits coming from these numbers are less than those inherent to the 10% PS case; the gap is in the order of 0.03% and 2%, indeed.
The following table sums up essential variations between the four hybridization cases handled; data refers again to one engine.

PS [%]	W_{ff} [kg]	$W_{ff_{saved}}$ [kg]	Δ [%]
0%	1832.137	0	0
5%	1599.420	-232.718	-12.702
10%	1538.786	-293.352	-16.011
15%	1539.240	-292.898	-15.987
20%	1575.469	-256.668	-14.009

Table 8.18. Fuel saving comparison during take-off and climb.

The analysis carried out points out that the electrification process get the highest performance with a power-split setting equal to 10%. In this case, the best trade-off between weight increment due to electrical stuff and power delivered is attained, fuel economy takes its maximum, best efficiencies are reached. As reported in fig.**??**, after PS=10% fuel consumption starts to grow again. There is still some convenience in terms of fuel saving with respect to the baseline configuration (PS=0%), but the mass added by batteries makes the aircraft heavier and that is why the slope changes and begins to grow-back.
The following table highlights all the variations related to the multiple degrees of hybridization tested, focusing on the gap between each "block".

PS	W_{ff} [kg]	$\Delta_{PS=0}$ [%]	$\Delta_{PS=0}$ [kg]	$\Delta_{PS=5}$ [%]	$\Delta_{PS=5}$ [kg]	$\Delta_{PS=10}$ [%]	$\Delta_{PS=10}$ [kg]	$\Delta_{PS=15}$ [%]	$\Delta_{PS=15}$ [kg]
0%	1832.137	0	0	0	0	0	0	0	0
5%	1599.420	-12.702	-232.718	0	0	0	0	0	0
10%	1538.786	-16.011	-293.352	-3.791	-60.634	0	0	0	0
15%	1539.240	-15.987	-292.898	-3.763	-60.180	0.030	0.454	0	0
20%	1575.469	-14.009	-256.668	-1.497	-23.951	2.384	36.683	2.354	36.229

Table 8.19. TO+climb fuel consumption comparison-PS.

In terms of energy consumption, block fuel is multiplied by the lower specific heat (LHV=43100 $\frac{kJ}{kg}$), and the result is reported hereafter.

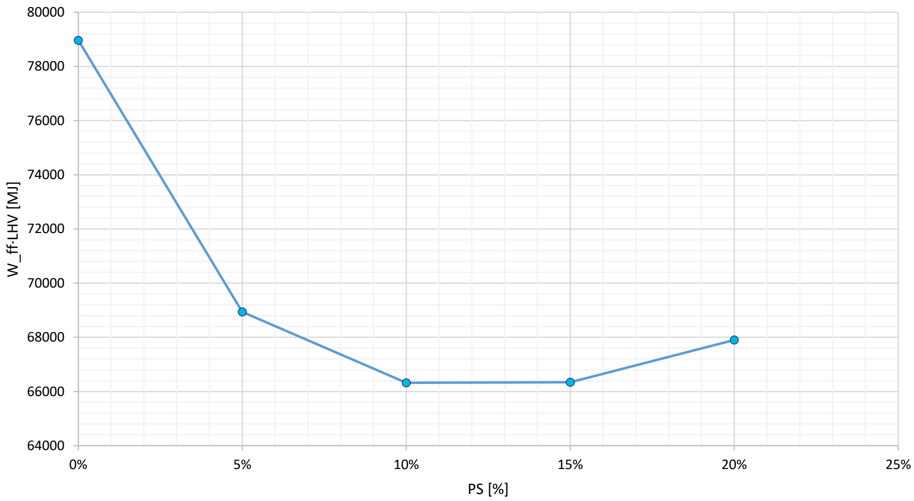

Figure 8.71. Energy consumption during take-off and climb phases.

The trend is very similar to that of fuel flow. It is possible to see that, thanks to the electrical train, with 5% PS more than 10000 MJ are saved in terms of fuel energy. Further improvements come doubling the percentage of electric power, as additional 2500 MJ are spared. This gap is compensated by batteries, which are able to supply this huge gap of energy, in order to fulfil LP spool power requirements. However, the amount of energy provided by the storage system linearly increases with power-split percentage and does not have a slope inversion, as happens in the fuel energy chart. This is because the electrical system is sized according to the power demand and does not take into account some kind of interactions between the aircraft, its aerodynamics and the engines themselves.
Continue dealing with energy, the following histograms show the quantity of energy produced burning fuel in comparison to that one stored in batteries (these data always refers to take-off and climb phases). View that 1 kWh equals 3.6 MJ, in order to compare the two quantities, battery energy is converted in the same unit used for measuring fuel flow one.

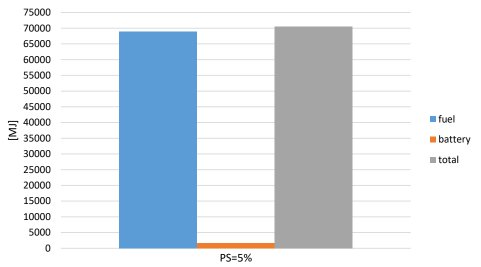

Figure 8.72. Energy PS=5%.

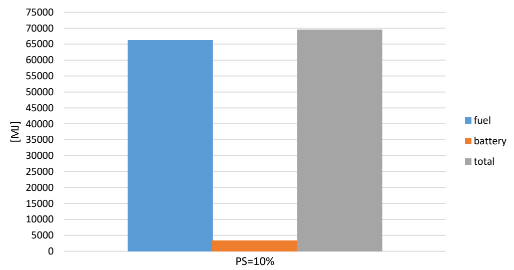

Figure 8.73. Energy PS=10%.

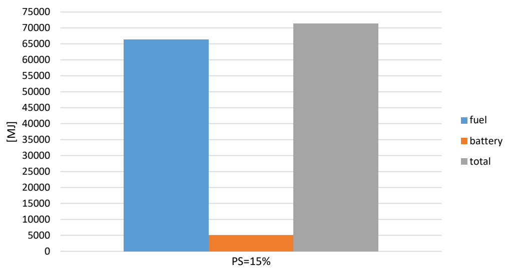

Figure 8.74. Energy PS=15%.

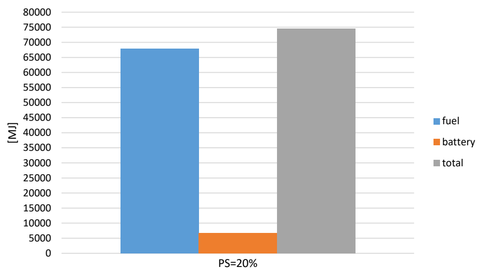

Figure 8.75. Energy PS=20%.

It is possible to appreciate that as the percentage of electrical energy fed by the storage system increases, the one related to chemical reactions taking place in the combustion chamber drops. If considering the sum of the two contributions, the optimum point still remains at a power split equal to 10%, i.e, where the fuel burnt is minimum. The global trend is reported in the figure below.

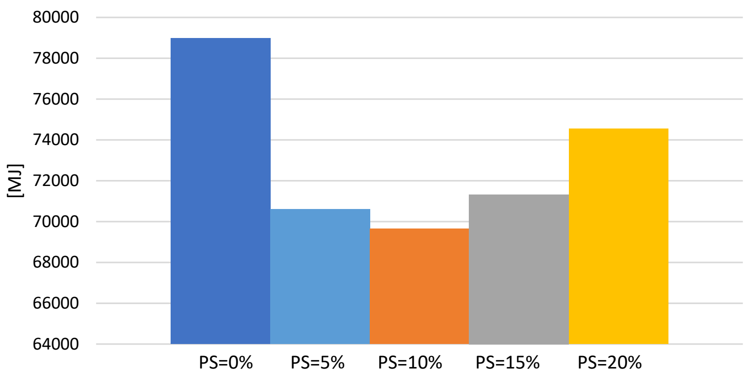

Figure 8.76. Energy levels for different PS.

Given that CO_2 emissions are directly related to fuel consumption, it is possible to calculate, in first approximation, how many kilos of carbon-dioxide are effectively produced by the gas-turbine engine considered in the analysis, and the equivalent reduction coming from the hybridization process. Taking reference to [79], for each gram of kerosene 3.5 g of CO_2 are produced and thus, applying this proportion to take-off and climb phases, the overall amount of pollutant emitted into the atmosphere is obtained.

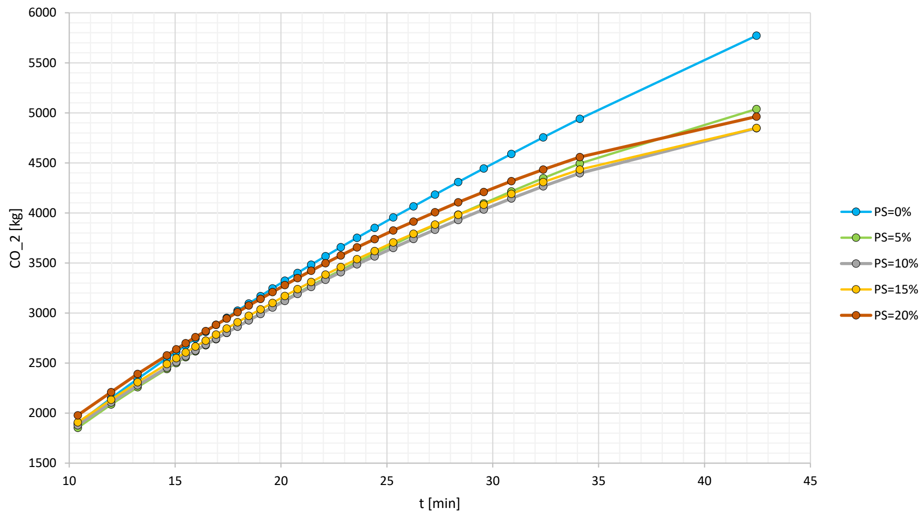

Figure 8.77. CO_2 emissions during take-off and climb phases.

Continue dealing with pollution, the other important parameter concerns the quantity of nitrogen-oxides produced during the combustion process. These are extremely harmful and many strategies were carried out in order to keep them in low percentage; one of these techniques refers to the "lean combustion". Following the procedure reported in [83] for an engine of the same thrust class and burner configuration, and taking an averaged value of the interpolation function there utilized, a chart has been made in which the rate of fuel consumption per second is plotted against the quantity (in grams) of NO_x produced per kg of fuel burnt.

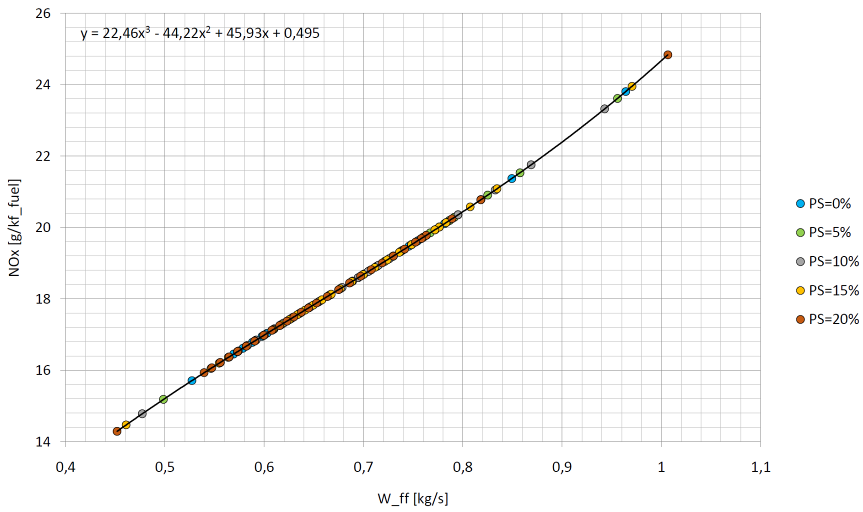

Figure 8.78. NO_x emissions interpolation curve.

To see what is the overall pollutant's production during take-off and climb segments, the NO_x emission parameter is interpolated from the graph (fig.8.78) [83] for each time segment and multiplied by the corresponding value of kerosene burnt. Results referring to one engine are shown in the following chart and resumed in table 8.21.

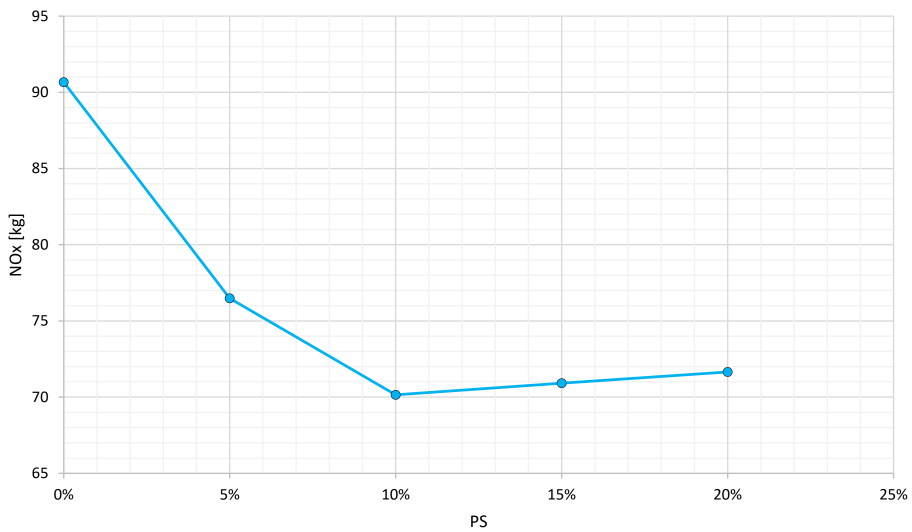

Figure 8.79. NO_x overall emissions during take-off and climb phases.

PS	NO_x [kg]
0%	90.663
5%	76.491
10%	70.153
15%	70.911
20%	71.645

Table 8.21. NO_x emission during take-off and climb.

The higher the fuel consumption, the higher the production of atmospheric pollutants. Being the 10% power split configuration the one which saves more fuel, it is also the one which produces less CO_2 and less NO_x. Same reasoning applies to the other PS settings, taking in mind that these quantities are strictly related to the amount of fuel used.
Moving on, view that the fuel flow is strictly related to the temperature at the exit of the burner ($W_{ff} \propto T_{41}$), it seems appropriate to say a quick word on it. Thus, the more critical situation is considered, i.e, that of take-off, where the TIT reaches its maximum value and, as a consequence, materials are subjected to higher stress' levels. Now, since a 5 K reduction in temperature brings to almost +50% life extension of the component taken into consideration, if the hybridization process leads to a temperature decrement, further potential benefits will come in terms of maintenance costs too. In fact, the lower the TIT, the lower materials' wear and fatigue, that is, less substitutions of corrupted chunks and longer inspections' intervals, with the immediate effect of dropping life-cycle costs. However, on the other hand, as T_{41} goes down, emissions are going to grow a bit. During combustion, new substances coming from chemical combinations of fuel and oxygen are created (these are the so called exhaust). When a hydrogen-carbon-based fuel burns, the exhaust includes water, carbon dioxide and also chemical combinations from the oxidizer alone, such as nitrogen oxides. Now, in order to reduce emissions, these compound should be split, and this process is directly related to chamber's temperature. Carbon dioxide's dissociation starts at around 900°C, while Nitrogen oxides one at 1200°C. So, the higher the temperature, the less NO_x production, but, unfortunately, as the degrees raise, CO_2 is subjected to another reaction, which ends with the formation of carbon monoxide (CO), a dangerous pollutant, one of the ones in charge of the depletion of the Ozone layer. None the less, many studies are focusing on the "dry low NO_x" (DLN), i.e the possibility of reducing nitrogen oxides' emissions keeping CO production as low as possible, and this is accomplished at the limits of combustion stability, by utilizing a weak mixture. In short, TIT

increment or decrement has its pros and cons, depending on the point o view. The chart reported hereafter shows take-off TIT as function of power-split.

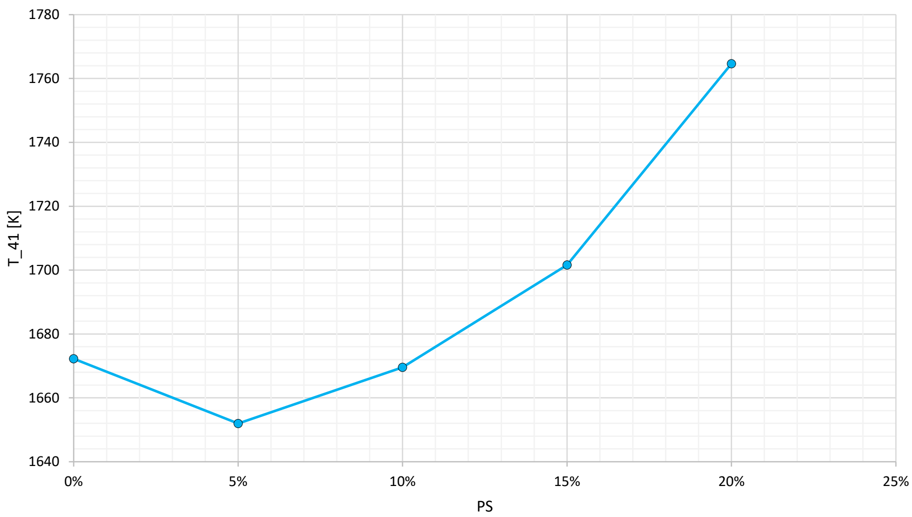

Figure 8.80. Take-off TIT function of PS.

It is possible to appreciate that with PS=5% temperature reaches its lowest value; this mean that the first turbine stage is subjected to smaller thermal stress and the amount of coolant can be reduced as well. In this case, the quantity of weight added by the electrical system with respect to its power is not so dramatically high and it does not adversely affect aircraft and engine performance. Moreover, a PS setting equals to 10% remarks a temperature increment if compared to the 5% mode, but the value is still 3 degrees less than that referring to PS=0%. The fact that now TIT is higher comes from the extra mass installed on-board, which starts to undermine electrification benefits. However, being the configuration which saves much more fuel than the others, this lead to the conclusion that it is also the one with less emissions, both in terms of CO_2 and NO_x. In addition, the slightly lower T_{41} brings its benefits on material deterioration and maintenance costs. Continue looking at the figure, one can see that it is not worth going further, to higher PS, as temperature dramatically boosts. Furthermore, the aircraft weight, as stated in previous comments, substantially increases, along with fuel consumption. As a consequence, emissions increase as well, as can be seen from table 8.19. One might argued that if the TIT is higher, the amount of NO_x produced should be lower; this is true, but in this case it should be noted that the quantity of fuel burnt is increased too by a great amount and so goes for pollutants, as highlight in fig.8.77. Carrying on the analysis, a cursory examination of the cruise segment might deserves some attention too. In order to say a few words on it, some results are plotted in the figures below (data refers to one single engine).

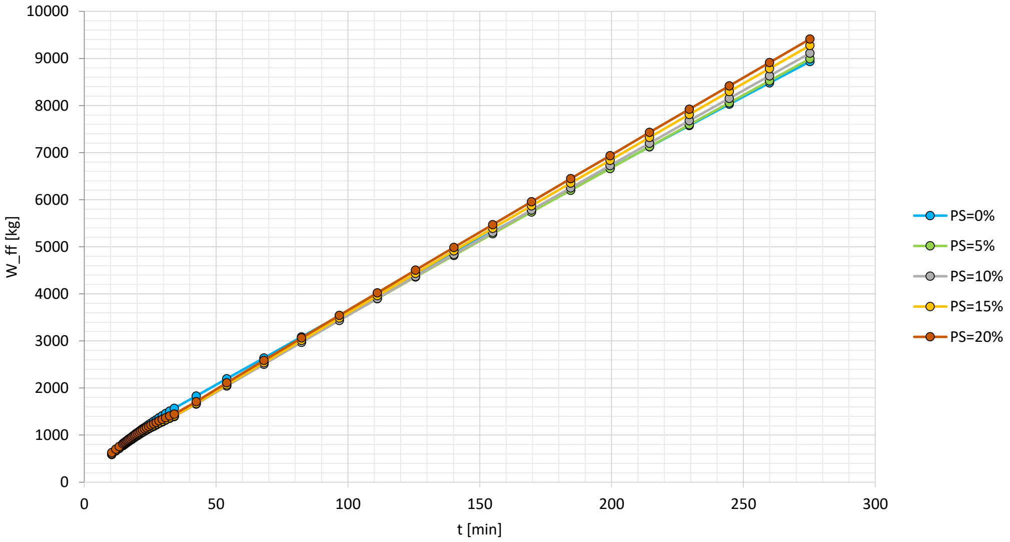

Figure 8.81. Fuel consumption at cruise.

Obviously, the global amount of fuel burnt increases during cruise (along this long period of time, no additional power is fed to the turbine), but in a different manner, depending on the degree of hybridization. Batteries should be recharged as well, but in this analysis the aforementioned process is not taken into consideration; however, this would increase fuel consumption even more. With regard to 5% power-split setting, one can observe that after the first steps the quantity of kerosene is always bigger than the one involving the baseline aircraft; considering the last value, it gets +1% in fuel consumption, while 0.75% corresponds to the mean value of additional fuel burnt along the entire cruise path. Further drawbacks come out when a greater amount of power has to be handle by the electrical components, and precisely when a PS=10% ($\simeq$1.9 MW) is considered. In this case, an average +2% is computed all along the path, while comparing the last data, it increases of about 2.11%, which, in any case, is much higher than the PS=5% architecture. As happened for the climb phase, further "electrical power" increment results in huge weight addition to the airplane and, as a consequence, fuel consumption inevitably boosts up. The PS=20% curve is a clear sign of what than just mentioned; it starts under the baseline configuration, then it crosses the other trends' lines until raising up to over 9000 Kg, i.e almost more than 350 Kg (+4.8%) of kerosene in comparison to the PS=10% case. This turnaround is mainly due to batteries' mass, which add 21 tonnes to the MTOW, underlining today technology limits too. One must keep in mind also the fact that aircraft aerodynamics is always the same for each PS setting, as the overall configuration is kept fixed. Actually, not only taxi and take-off consumption boost, but also the cruise one, and even if during the climb segment electrification's advantages come into play, these benefits seems to be enormously

cut off when looking at the mission in its entirety.
The chart reported hereafter (fig.8.82) shows the total mission fuel consumption related to one of the two turbofan engines installed on the aircraft, for many power-split conditions.

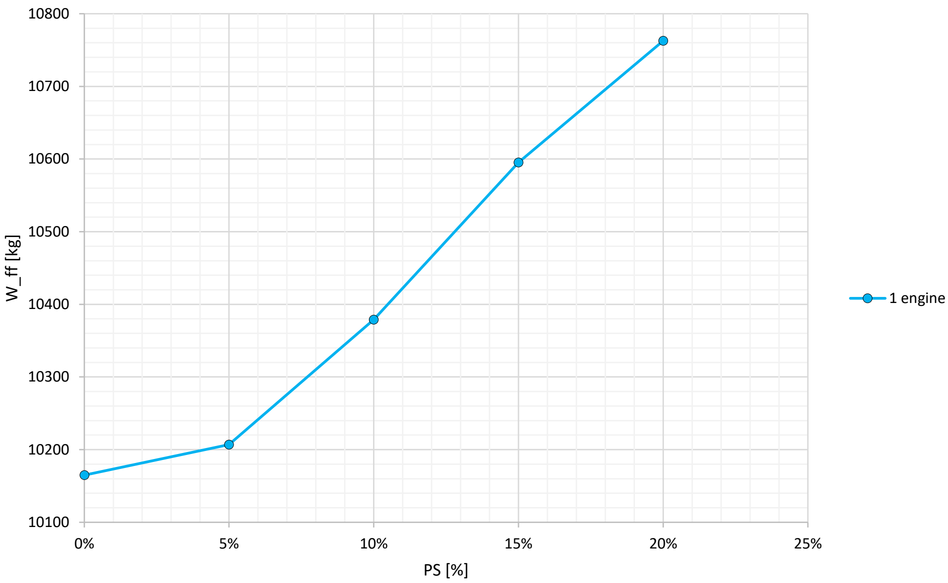

Figure 8.82. Overall mission fuel consumption.

The optimum hybridized architecture which produces less emissions, and thus less fuel consumption during take-off and climb is the one with PS=10%, but this is not if the all mission is considered. Due to the huge weight increment and the extended cruise time, the overall mission fuel consumption inevitably increases with the PS setting. The chart also takes into account the descent and the approach phases, in which fuel flow increases again a bit. The reason why consumption raises in these last two segments can be explained by considering that for a given aircraft, the optimum lift-to-drag ratio occurs at a particular speed. Furthermore, this last increases with airplane mass, so when it is heavier, it is expected to fly at higher Mach number during the descent and initial approach segments. The overall kilos of kerosene consumed would increase even more if battery recharging process is taken into consideration during cruise, due to their additional power off-take. It is true that, in doing this, electricity would be utilized along the lasts mission phases, i.e descent and approach, but the fuel saving coming from this shrewdness would be negligible if compared to the tonnes burnt in cruise. In order to obtain some benefits from the hybridization process, and thus save some kilos of kerosene, aircraft range should be reduced by a certain amount; in this case, it should be cut in half.

Table 8.23 summarizes the global mission's fuel consumption, and the additional kilos of kerosene consumed per engine, for each type of configuration adopted.

PS [%]	W_{ff} [kg]	W_{ff_add} [kg]	Δ [%]
0%	10164.909	0	0
5%	10266.91	102.004	1
10%	10379	214.091	2.11
15%	10595.42	430.51	4.24
20%	10762.63	597.726	5.88

Table 8.23. Mission's block fuel comparison.

If considering both engines, a power-split equal to 10% brings with it more or less half-ton fuel consumption increment, while for a PS=20% the amount boosts till 1200 kg. Of course, the high additional weight introduced in this last case, along with the complexities coming from the integration of the electrical drive-train and its connections with the gas-turbine engine, leads to the conclusion that is not worth going further with the electrification process, because there is more toil than profit, both from mechanical and economical point of view.
In conclusion, the following table highlights all the variations related to the multiple degrees of hybridization tested, focusing on the gap between each "block".

PS	W_{ff} [kg]	$\Delta_{PS=0}$ [%]	$\Delta_{PS=0}$ [kg]	$\Delta_{PS=5}$ [%]	$\Delta_{PS=5}$ [kg]	$\Delta_{PS=10}$ [%]	$\Delta_{PS=10}$ [kg]	$\Delta_{PS=15}$ [%]	$\Delta_{PS=15}$ [kg]
0%	10164.909	0	0	0	0	0	0	0	0
5%	10266.913	1.003	102.004	0	0	0	0	0	0
10%	10378.999	2.106	214.091	1.092	112.086	0	0	0	0
15%	10595.418	4.235	430.51	2.085	216.419	3.2	328.505	0	0
20%	10762.635	5.88	597.726	3.696	383.636	4.828	495.722	1.578	167.217

Table 8.24. Mission fuel consumption comparison-PS.

Chapter 9

All-electric architecture preliminary investigation

In this chapter, a preliminary investigation of an all-electric configuration is given. Taking as reference the same aircraft model utilized previously, the following analysis aims at considering the possibility of a complete electrification (PS=100%). Comparisons between actual and future promising technology will be made, in order to highlight today deficiencies in building this type of architecture. Again, view that actual batteries' energy density, along with current motor and inverter power-to-weight ratio are not high enough, the following test case will be approached taking reference to superconducting technology and on foreseeable storage system capacity values, which are going to be expected in the next thirty years. In light of this, a battery energy density equals to 2000 $\frac{Wh}{kg}$ is considered, even if comparisons will be made against smaller values, such as 1500 $\frac{Wh}{kg}$ and 200 $\frac{Wh}{kg}$, being this last current state-of-the-art technology for Li-ion accumulators. Dealing with power converter, a power density of 12 $\frac{kW}{kg}$ is suggested as possible next generation value, whereas for electric motors this parameter will raise till 18÷20 $\frac{kW}{kg}$.
A drive train is going to be set up, as in the previous case study, with the main difference that now gas-turbine engines do not exist any more, and they are replaced by an equal number of motor-driven fans. Because of the high powers into play, especially during take-off, large voltages are ruled out and a nominal 3000 V line is chosen. Therefore, according to the formula $P = V \cdot i$, current can be kept as low as possible, so as to minimize Ohm and interference losses along the line and inside each element too, with further possible efficiency's increment.
A focus will be also made on weight's breakdown, and components' mass will be compared with the one calculated in the previous chapter.
It is worth to emphasize even more that, due to technology limitations, the architecture that is going to be sized is absolutely unattainable nowadays, essentially in terms of components power density and weight. This is the target to which aviation

industry is trying to move towards, in order to built more "eco-friendly" aircraft and thus satisfying IATA and NASA's N3+ emissions' regulations.

9.1 Electric train sizing

As done for the hybridization test case, in order to size the electrical components the power profile is needed (fig.9.1). In this case, a PS=100% is considered, i.e the overall power is produced and fed only by the electric train, and thus there is no more the necessity of a kerosene based turbo-engine. Actually, they are replaced by lighter motor-driven fans respectively.

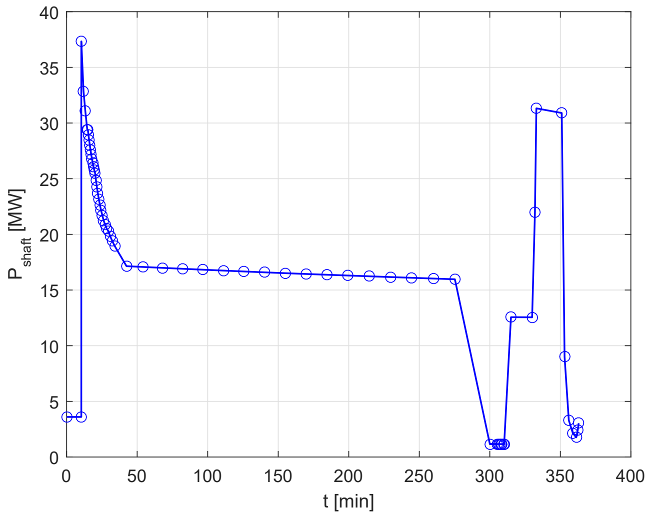

Figure 9.1. All-electric aircraft power profile.

The figure above refers to the overall power requirement, which as to be split between the two fans. The profile includes also a holding and a diversion phase, in case the destination aerodrome's landing may not be made for some reasons (for example awful weather conditions or air strip's congestion). One can see that the peak power demand corresponds to the take-off phase, where the two HTS motor have to deliver more than 18 MW each. During the climb segment, power requirements decrease till top of climb altitude; from this point on, the cruise path begins and it is carried out at approximately constant power. After that, the descent phase takes place, followed by a go-around and a diversion segment, that leads up to the final approach and landing. Again, as done in chapter 8, approximately 10 minutes are considered for engines' starting clearance and taxi operations, while only few minutes are accounted to reach the gate, after landing is complete.

9.1.1 HTS motor sizing

Superconducting technology permits to shrink components' dimensions, at the expense of a more detailed and complicated design, involving a cryogenic cooling system. Nonetheless, high power to weight ratio can be achieved, even twice times than that corresponding to their conventional counterpart, while losses are reduced by a great amount; in fact, as the working temperature drops ($\simeq$ 70÷80 K), the resistance tide uncounters along the path goes down.
Each of the two electric motors is sized taking as reference the peak power demand. Being an HTS architecture, a slotless configuration is assumed and, as a consequence, the armature is removed [5]. As can be deduced, this configuration leads to a considerable weight saving, such that high power can be achieved without many problems involving volumes and installation.
The following table summarises the mass of the different parts, whereas the figures that follow show losses and efficiency trends for a single HTS motor.

D_{tot} [m]	0.579
L_{tot} [m]	3.183
$m_{magnets}$ [kg]	73.197
m_{rotor}+m_{shaft} [kg]	254.241
$m_{service}$ [kg]	68.357
m_{stator} [kg]	198.385
m_{motor} [kg]	594.181

Table 9.2. HTS motor mass breakdown.

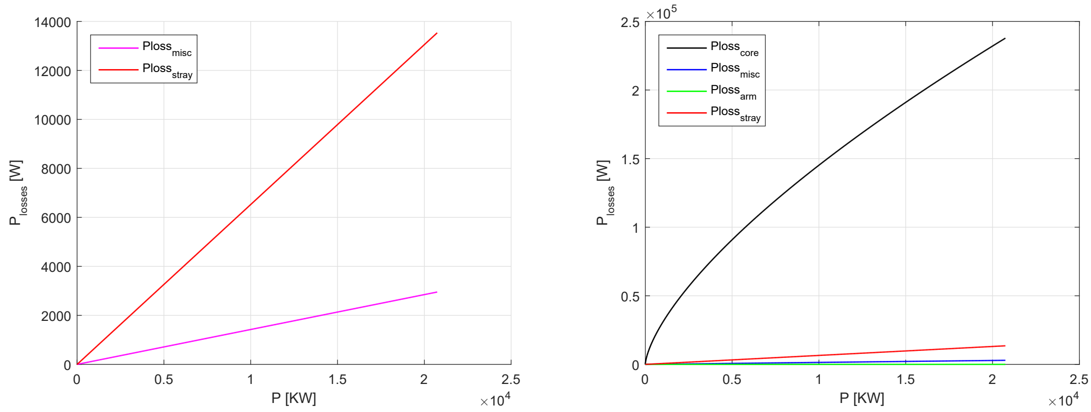

Figure 9.2. HTS motor losses breakdown.

The main losses are always associated to the core, but this time they are much less than those belonging to the same motor, but with a conventional architecture. Armature losses are null, while the miscellaneous and the stray ones are negligible.

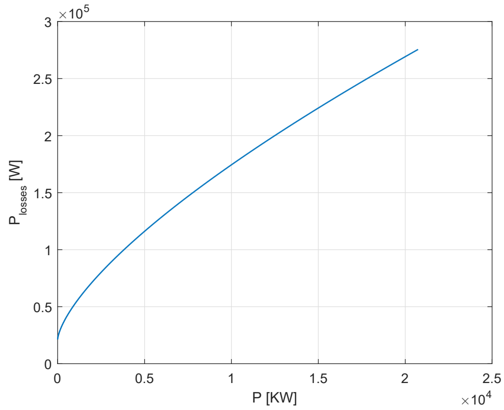

Figure 9.3. HTS motor total losses.

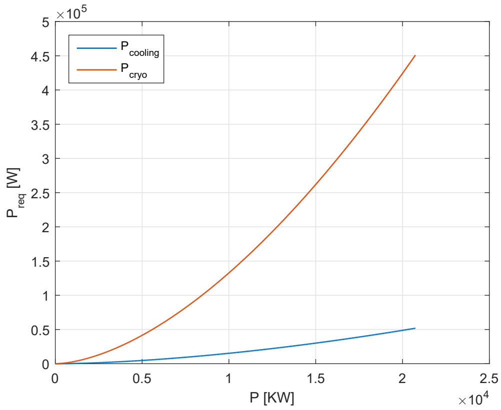

Figure 9.4. Cryo-cooler and cooling power.

In order to cools the system down up to cryogenic temperatures, an additional apparatus, the cryo-cooler, has to be installed. This is a heavy, bulky and low efficient machine, as can be seen in the gap between the cooling power and the cryo-component one. Because of this additional item, the overall efficiency of the superconducting motor drops from 0.987 to 0.966 as outlined in figure 9.5.

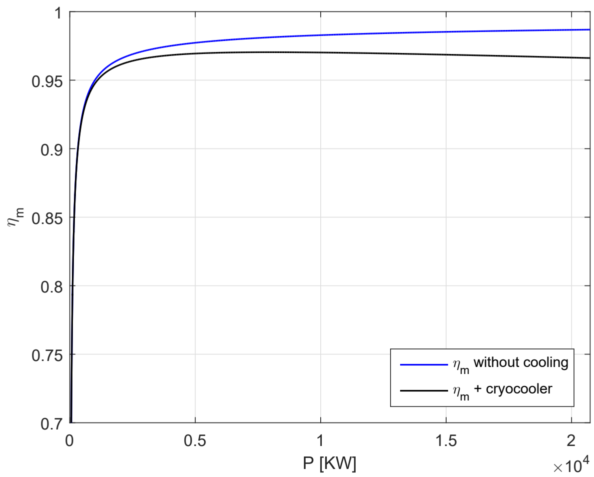

Figure 9.5. HTS motor efficiency.

Continue dealing with HTS machines, it is now the turn of the power converter. Unfortunately, very few informations are available in the literature, concerning its characteristics. Among them, it is expected that it should have higher efficiency, well above 95% and greater power density, up to 15 $\frac{kW}{kg}$ [21]. Now, so as to give an idea of what could be its mass and the global train efficiency, a power to weight ratio of 12 $\frac{kW}{kg}$ and $\eta_{inv} = 0.97$ are taken as reference values. This choice leads to a total mass of 3111.04 kg.

9.1.2 Batteries sizing

The sizing procedure takes exactly the same steps done for the hybridization test case [8]. Line and components' losses are taken into account by introducing a transmission efficiency η_{tr}, while batteries' mass is obtained by computing the overall capacity needed to accomplish the entire mission. Additional 270 kW are added, so as to take into account subsystems' off-take requirements, while a state of charge of 25% is set as the minimum end of mission threshold safety value. Furthermore, due to powers into play, batteries are divided in 15 packs; in this way, one container has only to handle $\frac{1}{15}$ of the total power, and the global efficiency raises a bit.
The table reported hereafter shows some results related to the sizing procedure.

$P_{offtake}$ [kW]	270
ρ_{bat} $\left[\frac{Wh}{kg}\right]$	2000
W_{bat} [kg]	53266.995
U_{nom} [V]	3000
C_{tot} [MWh]	92.638
$n_{cell_{series}}$	800
$m_{cell_{parallel}}$	75000
$n_{cell_{tot}}$	$60 \cdot 10^6$
SOC_{end}	25%
n_{pack}	15
η_{mean}	0.976

Table 9.4. Batteries' sizing results for all-electric configuration.

Having all the data at hand, the overall transmission efficiency of the train can be obtained by multiplying those of each single component; taking into account also the cryo-cooler, it is $\eta_{tr} = 0.917$.
The set of figures reported in the following pages highlight electrical variables trends for the all-electric configuration considered.

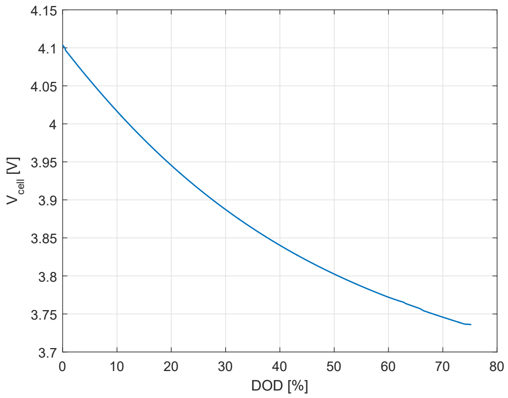

Figure 9.6. Battery cell voltage-DOD PS=100%.

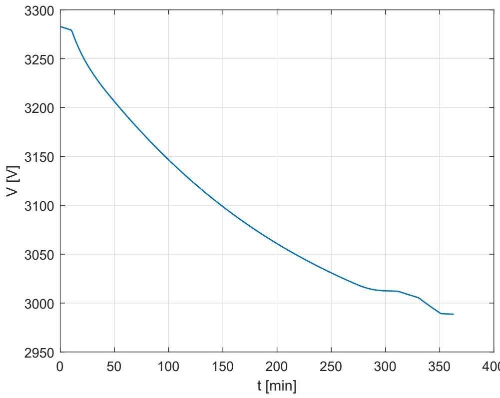

Figure 9.7. Battery voltage-time PS=100%.

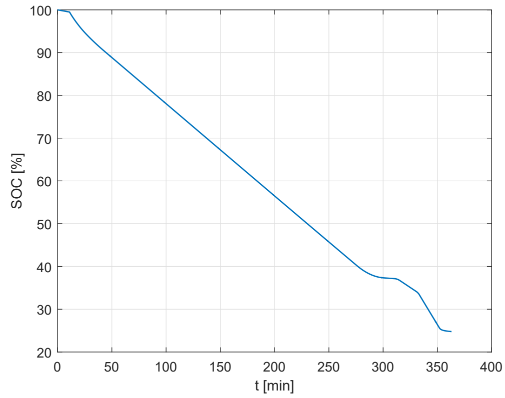

Figure 9.8. State of charge PS=100%.

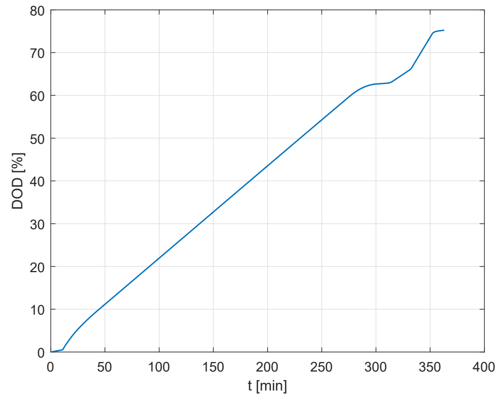

Figure 9.9. Depth of discharge PS=100%.

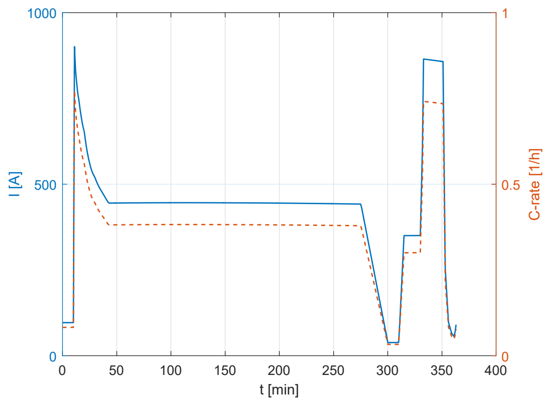

Figure 9.10. Current and C-rate PS=100%

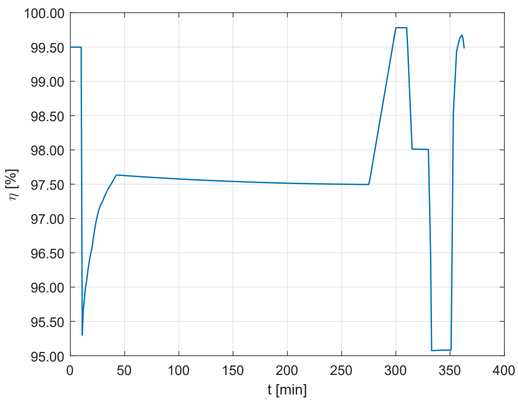

Figure 9.11. Batery efficiency PS=100%

Cell's voltage constantly decreases during the discharge process, as well as the overall output voltage. However, this last has a flat region, which coincides with the minimum power demand phase. Then, due to throttle settings adopted along the second climb phase, i.e that of diversion, power increases and, as a consequence, voltage starts to drop again. Same trends can be observe for the SOC and DOD, which is essentially its counterpart (the two curves are flipped each others). As voltage constantly decreases, current, on the other hand, grows and drops according to power's demand; as this last raises, "Ampères" do the same, and vice-versa. Up peaks' current (i) correspond to high C-rate peaks and low peak efficiency, as losses increase proportionally to "i"'s square and thus batteries discharge rate is steeper. Conversely, low currents are followed by more moderate C-rate and higher efficiency.

In what concerning storage system's mass, a comparison is made hereafter for three different energy density parameters, ranging from state-of-the-art to foreseeable target ones (fig.9.12). Today complete aircraft electrification would account for more than 500 tonnes of batteries, a weight which is quite similar to that of an Airbus A380. Of course, this is completely absurd, as the result would be a "flying battery" instead of an aircraft. For this main reason, a power split equal to 100% is definitely unfeasible and it makes no sense. An energy density increment up to 1500 $\frac{Wh}{kg}$ dramatically changes perspectives. In fact, in this case, the overall mass drops to 71.02 tonnes (-86.7%), and this numbers take much more sense. A further rise up to 2000 $\frac{Wh}{kg}$ permits to save another 3.3% of mass, for a total of 53.27 tonnes. In this way, an all-electric architecture can be taken into consideration as a possible option for future aircraft design.

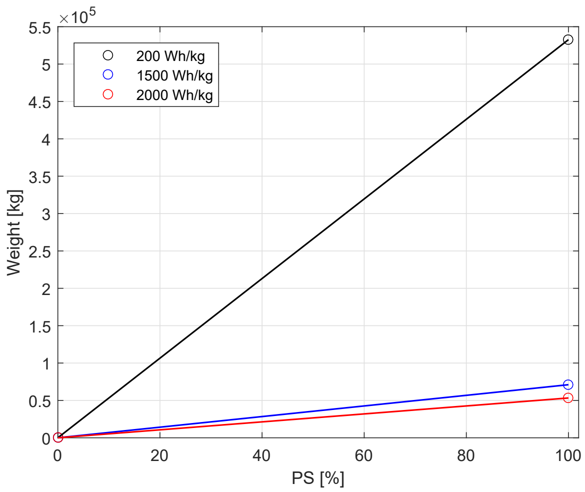

Figure 9.12. Battery energy density comparison for all-electric architectures.

Figure 9.13 and figure 9.14 highlight the mass breakdown for the all electric aircraft configuration analysed. Again, the most relevant percentage is that of batteries, followed by the PMAD and by the superconducting motors. One must keep in mind that this data do not refers to actual technology level, but at the one planned for 2035 and, more probably, 2050.

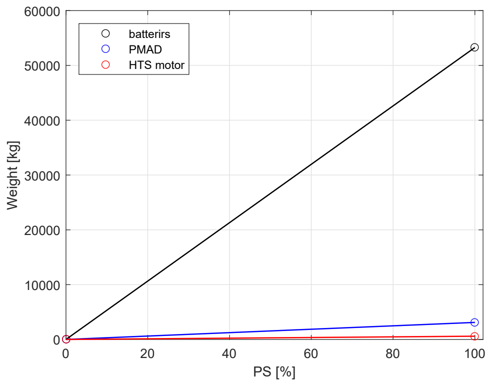

Figure 9.13. Components mass for PS=100%

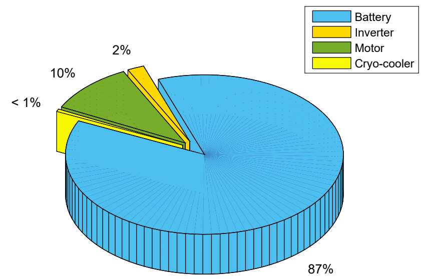

Figure 9.14. Weight breakdown for PS=100%

A last comparison is made between the MTOW of the baseline aircraft's configuration and that of the all-electric one. The final output is reported in fig.9.15.

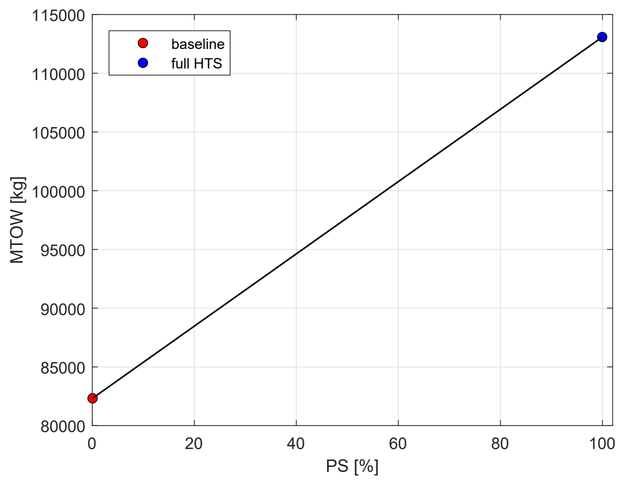

Figure 9.15. MTOW baseline and all-electric airplane comparison.

The comparison has been made as described below. The baseline aircraft MTOW equals 82313.38 kg, to which 22000 kg of fuel might be subtracted, along with the reserve. In addition, view that the all-electric architecture does not need kerosene any more, also the auxiliary power unit (APU) becomes unnecessary, and so other 188.5 kg has to be removed (this value refers to the Honeywell 131-9A APU [63]). Talking about gas-turbine engines, these are replaced by an equivalent number of motor-driven fans; as a consequence, no more compressors are needed, as well as

combustors and turbines, the lasts accounting for about 30% of the entire turbofan mass. The new propulsors will be made simply by a fan and a nozzle; so, the turbomachinery weight drops by about 60%, reducing the initial single engine mass of about 2975 kg by more or less 1190 kg. In turn, the weight of the electrical drivetrain has to be added, and of course the most impacting factor is that of batteries, which account for 87% of the total mass. Finally, the reconfigured aircraft MTOW equals 113089.763 kg, 27.2% more heavier than the baseline one. This is obviously a first approximation, as many features are not included in the analysis, such as, for example, the additional mass related to wires, the weight reduction due to fuel tanks removal, and so forth.
In any case, this preliminary analysis gives an overview on the possibility of building a "green" aircraft, characterized by zero emissions and a significant noise reduction coming from the absence of turbomachinery components and thus of the thermodynamic Brayton cycle. It also highlight benefits and disadvantages resulting from this new technology, along with obstacles and constraints imposed by actual level of scientific know-how and technology.

Chapter 10

Conclusions

10.1 Project findings

In this thesis, turbo/hybrid-electric propulsion has been investigated.
An electric drive train has been modelled, along with a conventional gas-turbine engine, then the two were coupled together to result in a new propulsion system architecture, in which power requirements are satisfied both by the kerosene-based turbofan and by electrical driven motors, powered by batteries and controlled by PMAD units. A power-split parameter is introduced in order to take into account the percentage of electrical power fed through the low pressure spool with respect to the total one. Multiple simulations have been run, each one set with a different value of PS, so as to see aircraft and engines behaviour, other than effects coming from the introduction of additional weight to the system as a all. Special attention has been paid to fuel consumption and emissions during take-off and climb phases, as well as on the overall mission performance.
Results have shown that the hybridization process is partially feasible and that some benefits can be achieved during the first part of the mission. However, some limits have been outlined, precisely those related to the huge weight gain when reaching a certain percentage of PS (15%÷20%). The analysis performed has highlighted an optimum point, which coincides with an electrical power input equal to 10% of the peak value met at take-off. With such hybridization setting, 3077.57 kg of kerosene is burnt during taxi and lift-off segments, with an overall fuel saving of approximately more than 550 kg, in comparison to the baseline configuration. This 16% improvement in fuel consumption immediately reflects on CO_2 emissions, which decrease proportionally, and on NO_x production, with an extraordinary -22.62% if compared to the conventional architecture. Giving a glance to the overall mission, a PS=10% accounts for 428.18 kg of additional fuel burnt (+2.11%) and this is a quite dramatic outcome. Concerning the others power split, some advantages related to take-off and climb are still there, even if to a lesser extent, but this is

not for the overall mission. For example, dealing with the early flight's stages, a PS=5% leads to 12.7% fuel saving, while higher PS modes raises the percentage till 15%. The situation looks completely different if the global flight envelope is taken into account. In this case, the smaller hybridization factor results in an efficiency drop of about 1%, whilst when 3.7 MW are fed by the motor, this value falls down to 5.88%. This tendency shows that it is not worth increasing the electrification further, because it would be useless and inefficient. Also the PS=15% and PS=20% configurations should be avoided, since no possible benefits would come out, either in terms of costs or in terms of technical complexity. What is wanted to underline here is that it does not make sense to design and build an extremely tough propulsion system, with all the challenges and problems it brings with, if profits are not consistent with the workload. None the less, benefits that turbo-electric propulsion has to achieve might be evident along the first flight segments, has showed for the 5% and 10% power-split configurations.
Possible fuel saving is affordable, along with an overall efficiency increment during the most demanding flight envelope points. In addition, further improvements come from TIT temperature drop, which lead to components' life extension and, as a consequence, to maintenance costs' reduction.
In summary, the hybridization process has many advantages and disadvantages too, depending on the flight phase considered and, if technology level is going to increase in a significant manner, it could bring back crucial profits and benefits and could be extended even toward higher power requirements aircraft.

10.2 Future works

In light of the results obtained in previous chapters, aircraft electrification could be carried out, in conjunction with know-how improvements, so as to further reduce gas-turbine engines' importance, till their complete removal. In short, the final purpose should be that of replacing fuel burn turbofan with more ecological and efficient electric driven fans; in doing this, a power-split equal to 100% would be achieved, and the overall power requirements will be completely satisfied by energy stored in batteries. In order to design such "eco-friendly" and extremely advanced aircraft architecture, superconducting technology is mandatory; in this way, losses associated to tied lines will drop almost to zero, while power converters and motors could gain a high power-to-weight ratio level. As a consequence, weights will significantly decrease, opening this new horizons even to bigger, long range aircraft. In dealing with superconduction, one must keep in mind that the working temperature has to be very low, around 80 K, so something is needed as cooling, such as a cryo-cooler or some liquid element (H_2 or N_2) stored in insulated tanks. Both options are bulky and heavy, and thus improvements should be done on them, both in terms of performance and materials' quality. None the less, according to future

technology developments, all-electric airplanes will replace conventional ones, so as to bring engineering one step ahead.
Another important aspect not considered in this analysis is the one related to maintenance and life-cycle costs. In fact, the introduction of new elements can lead to additional benefits, but there is also to take into account the possibility of multiple failures, as the complexity of the system is increased. Fuel consumption reduction can immediately bring to money saving, but if looking to the overall process and taking into consideration all the "product-life-chain", i.e from electrical components manufacturing, testing, installation, maintenance and disposal, things could go in a different way, as many more variables come into play.
The target to get is there, written and fixed, but the road is still longer, so far.

Bibliography

[1] Arne Seitz, Askin T. Isikveren, Mirko Hornung, *Pre-Concept Performance Investigation of Electrically Powered Aero-Propulsion Systems*, AIAA, Joint Propulsion Conferences, San Jose (CA), July 14-17, 2013.

[2] H. Kuhn, A. Sizmann, *Fundamental Prerequisites for Electric Flying*, Deutscher Luft-und Raumfahrtkongress, Munich, 2012.

[3] Tyler J. Wall, Richard T. Meyer, *A Survey of Hybrid Electric Propulsion for Aircraft*, AIAA, Propulsion and Energy Forum, Kalamazoo (MI), July 10-12 2017.

[4] Niccolò Rossi, *Conceptual Design of Hybrid-Electric Aircraft*, Politecnico di Milano, Milano, 2017.

[5] Patrick C. Vratny, Philipp Forsbach, Arne Seitz, Mirko Hornung, *Investigation of Universally Electric Propulsion Systems for Transport Aircraft*, 29^{th} Congress of the International Council of the Aeronautical Sciences, San Petersburg, September 7-12 2014.

[6] Scott W. Ashcraft, Andres S. Padron, Kyle A. Pascioni, Gary W. Stout, *Review of Propulsion Technologies for N+3 Subsonic Vehicle Concepts*, NASA, Cleveland, 2011.

[7] Joris Van Bogaert, *Assessment of Potential Fuel Saving Benefits of Hybrid-Electric Regional Aircraft*, TUDelft, Delft, 2015.

[8] Patrick C. Vratny, Clément Pornet, Askin T. Isikveren, Mirko Hornung, *Battery Pack Modelling Methods for Universally-Electric Aircraft*,4^{th} CEAS Air and Space Conference, Vien, 2013.

[9] Paolo Maggiore, *Sistema Elettrico*, Corso di Sistemi di Bordo Aerospaziali, Torino, 2015.

[10] Andy Ko, J. A. Schetz, William H. Mason, *Assessment of the Potential Advantages of Distributed-Propulsion for Aircraft*, ISABE, Blacksburg, 2003.

[11] Michael J. Armstrong, Mark Blackwelder, Andrew Bollman, Christine Ross, Angela Campbell, Catherine Jones, Patrick Norman, *Architecture, Voltage, and Components for a Turboelectric Distributed Propulsion Electric Grid*, NASA, Cleveland, 2015.

[12] James L. Felder, *NASA N3-X with Turboelectric Distributed Propulsion*, NASA, Cleveland.

[13] James L. Felder, Hyun Dae Kim, Gerald V. Brown, *Turboelectric Distributed*

Propulsion Engine Cycle Analysis for Hybrid-Wing-Body Aircraft, NASA, Cleveland, 2009.

[14] Allan R. Hambley, *Elettrotecnica*, Pearson Paravia Bruno Mondadori, 2009.

[15] Ulrich Kreutzer, *Electric Flight Takes Off*, Siemens, Picture of the Future, 2016.

[16] *Superconductivity*, CERN, CERN website, February 2013.

[17] Joe Khachan, Stephen Bosi *Superconductivity*, Sydney University.

[18] Kiruba S. Haran et al, *High power density superconducting rotating machines—development status and technology roadmap*, Supercond. Sci. Technol., 2017.

[19] Frederick Berg, Joseph Palmer, Paul Miller, Mark Husband, Graham Dodds, *HTS Electrical System for a Distributed Propulsion Aircraft*, IEEE Transaction on applied superconductivity, 2015.

[20] Paul N. Barnes, Michael D. Sumption, Gregory L. Rhoads, *Review of high power density superconducting generators: Present state and prospects for incorporating YBCO windings*, Cryogenics, Elsevier, Columbus, 2005.

[21] Gerald V. Brown, *Weights and Efficiencies of Electric Components of a Turboelectric Aircraft Propulsion System*, NASA, 49^{th} AIAA Aerospace Sciences Meeting, Orlando, 2011.

[22] Gerald V. Brown et al, *Efficient Flight-Weight Electric Systems*, NASA, 49^{th} NASA Technical conference, Cleveland, 2012.

[23] Sonja I. Schlachter, Wilfried Goldacker, Bernhard Holzapfel, Andrej Kudymow, Hong Wu, *DC-HTS Cables for Power Distribution in Hybrid-Electric Aircraft*, NASA, 49^{th} KIT, Aspen, 2016.

[24] Cesar A. Luongo, Philippe J. Masson, Taewoo Nam, Dimitri Mavris, Hyun D. Kim, Gerald V. Brown, Mark Waters, David Hall, *Next Generation More-Electric Aircraft: A Potential Application for HTS Superconductors*, IEEE/CSC&ESAS, European Superconductivity News Forum, 2008.

[25] Meletios Pagonis, *Electrical Power Aspects of Distributed Propulsion System in Turbo-Electric Powered Aircraft*, PhD thesis, Cranfield, 2015.

[26] Liu Chengyuan, *Turboelectric Distributed Propulsion System Modelling*, PhD thesis, Cranfield, 2013.

[27] *Aircraft Wires and Cables*, Nexans, Paris.

[28] David Koyama, *How the More Electric Aircraft is influencing a More Electric Engine and More*, Rolls Royce, Electrical Technologies for Aviation of the future, Tokyo, 2015.

[29] James L. Felder, Hyun Dae Kim, Gerald V. Brown, *Turboelectric Distributed Propulsion Engine Cycle Analysis for Hybrid-Wing-Body Aircraft*, NASA, 47^{th} AIAA Aerospace Sciences Meeting Including The New Horizons Forum and Aerospace Exposition, Orlando, 2009.

[30] Frank Anton, Wulf Roscher, *Airbus, Rolls-Royce and Siemens to develop Flying Demonstrator*, Siemens, Pictures of the future, 2017

[31] Hans-Jörg Steiner, Patrick C. Vratny, Askin T. Isikveren, Mirko Hornung, *Performance and Sizing of Transport Aircraft Employing Electrically-Powered Distributed Propulsion*, Bauhaus Luftfahrt, Munich, 2012

[32] Marty K. Bradley, Christopher K. Droney, *Subsonic Ultra Green Aircraft Research Phase II: N+4 Advanced Concept Development*, Boeing Research and Technology, Huntington Beach, 2012

[33] *Panasonic data-sheet*, Panasonic, 2007.

[34] Mohamed Rashed et al, *Conceptual Design of Battery Energy Storage for Aircraft Hybrid Propulsion*, The University of Nottingham, Electric & Hybrid Aerospace Technology Symposium, Cologne, 2012

[35] Gokcin Cinar, Dimitri N. Mavris, Mathias Emeneth, Alexander Schneegans, Carsten Riediger, Yann Fefermann, Askin Isikveren, *Sizing, Integration and Performance Evaluation of Hybrid Electric Propulsion Subsystem Architectures*, AIAA SciTech Forum, 55^{th} AIAA Aerospace Sciences Meeting, Grapevine, 2007

[36] Clément Pornet, Patrick C. Vratny, Arne Seitz, Askin T. Isikveren, *Methodology for Sizing and Performance Assessment of Hybrid Energy Aircraft*, Bauhaus Luftfahrt, Journal of Aircraft, Munich, 2014

[37] L.L.M Veldhuis, M. Voskuijl, *Exploration of Hybrid Electric Propulsion in regional Aircraft*, TU Delft, Delft.

[38] David G. Vutetakis, *Batteries*, Douglass Battery Co., The Avionics Handbook, Boca raton, 2001.

[39] *PowerTech systems*, PowerTech, France.

[40] Shuhui Li, Bao Ke, *Study of Battery Modeling usign Mathematical and Circuit Oriented Approaches*, The University of Alabama, IEEE, Tuscaloosa, 2011.

[41] M.R. Jongerden, B.R. Haverkort, *Battery Modeling*

[42] Jake Christensen, Paul Albertus, Roel S. Sanchez-Carrera, Timm Lohmann, Boris Kozinsky, Ralf Liedtke, Jasim Ahmed, Aleksandar Kojica, *A Critical Review of Li/Air Batteries*, Critical Reviews in Electrochemical and Solid-State Science and Technology, Journal of The Electrochemical Society, 2011.

[43] Peter G. Bruce, Stefan A. Freunberger, Laurence J. Hardwick, Jean-Marie Tarascon, *$Li - O_2$ and $Li - S$ batteries with high energy storage*, Nature Materials, 2011.

[44] Ahmad Rahmoun, Helmuth Biechl, *Modelling of Li-ion batteries using equivalent circuit diagrams*, Przeglad Elektrotechniczny, Kempten, 2011.

[45] Abbas Fotouhi, Daniel J. Auger, Karsten Propp, Stefano Longo, Mark Wild, *A review on electric vehicle battery modelling: from Lithium-ion towards Lithium-Sulphur*, Elsevier, Renewvable and Sustainable Energy Reviews, 2016.

[46] Kiruba S. Haran et al, *High power density superconducting rotating machines—development status and technology roadmap*, IOP Publishing, 2017.

[47] Yoshiki Miyairi, Christopher A. Perullo, *A Parametric Environment for Weight and Sizing Prediction of Motor/Generator for Hybrid Electric Propulsion*,

AIAA, 51^{st} AIAA/SAE/ASEE Joint Propulsion Conference Publishing, Orlando, 2015.

[48] Surong Huang, Jian Luo et al, *A General Approach to Sizing and Power Density Equations for Comparison of Electrical Machines*, IEEE, Transactions on industry applications, 1998.

[49] Jonathan E. Rucker, *Design and Analysis of a Permanent Magnet Generator for Naval Applications*, MIT, Master of Science in Electrical Engineering and Computer Science, 2005.

[50] S.K. Baik, Y.K. Kwona et al, *Electrical parameter evaluation of a 1 MW HTS motor via analysis and experiments*, Elsevier, Cryogenics, 2009.

[51] H. Fürsich, *Der Turbogenerator mit supraleitender Erregerwicklung im transienten Betrieb*, Springer-Verlag, Archiv für Elktrotechnik, München, 1976.

[52] Robert A. McDonald, *Electric Motor Modeling for Conceptual Aircraft Design*, AIAA, 51^{st} Aerospace Sciences Meeting including the New Horizons Forum and Aerospace Exposition, Grapevine, 2013.

[53] M. Bogomolov, *Concept study of 20 MW high-speed permanent magnet synchronous motor for marine propulsion*, TU/e, Eindhoven Technische Univestiteit, Eindhoven, 2013.

[54] Frederick Berg, Joseph Palmer, Paul Miller, Mark Husband, Graham Dodds, *HTS Electrical System for a Distributed Propulsion Aircraft*, IEEE, Transactions on applied superconductivity, 2015.

[55] Philippe J. Masson, Danielle S. Soban et al, *HTS Motors in Aircraft Propulsion: Design Considerations*, IEEE, Transactions on applied superconductivity, 2005.

[56] P. J. Masson, Cesar Luongo, *High Power Density Superconducting Motor for All-Electric Aircraft Propulsion*, IEEE, Transactions on applied superconductivity, 2005.

[57] Wei Xian et al, *Numerical assessment of efficiency and control stability of an HTS synchronous motor*, IOP, Journal of Physics, 2010.

[58] Paul Gemin, Tom Kupiszewski, Arthur Radun, *Architecture, Voltage and Components for a Turboelectric Distributed Propulsion Electric Grid (AVC-TeDP)*, NASA, Cleveland, 2015.

[59] Paul N. Barnes, Michael D. Sumption, Gregory L. Rhoads, *Review of high power density superconducting generators: Present state and prospects for incorporating YBCO windings*, Elsevier, Cryogenics, 2005.

[60] M. Lokhandwalla, K.S. Haran, J.P. Alexander, *Scaling studies of High Speed High Temperature Superconducting Generator*, IEEE, 2012.

[61] H. Daffix, P. Tixador, *Design of a fully Superconducting Synchronous Motor*, Electric Machines and Power Systems, 2007.

[62] Ozan Keysan, Markus Mueller, *A modular and cost-effective superconducting generator design for offshore wind turbines*, Superconductor Science and Technology, 2015.

[63] Dieter Scholz, *An Optiomal APU for Passenger Aircraft*, Aircraft Design and System Group (AERO), Hamburg University of Applied Sciences, 5th CEAS Air and Space Conference, Delft, September2015.

[64] *Smart Batteries*, Lunasoft, 2017.

[65] Arendt Wintrich, Ulrich Nicolai et al, *Application Manual Power Semiconductors*, Semikron, Semikron International GmBh, Verlag, 2015.

[66] *Electric Motors*, Audi, Audi technology portal, 2011.

[67] MIT Electric Vehicle Team, *A Guide to Understanding Battery Specifications*, MIT, 2008.

[68] M. Chen, G.A. Rincon-Mora, *Accurate Electrical Battery Model Capable of Predicting Runtime and I-V Performances*, IEEE, Transaction on Energy Conversion, 2006.

[69] *Electrochemical cells*, Gamry instruments, Warminster.

[70] A. Wintrich, U. Nicolai, W. Tursky, T. Reimann, *Application Manual Power Semiconductors*, ISLE, Verlag, 2011.

[71] G. Dvorsky, *HBC-Series V7*, Manual, Zlin.

[72] Semikron, *SemiSel*, Simulation tool, www.semikron.com.

[73] F. Sargos, *IGBT Power Electronics Teaching System, Principle for Sizing Power Converter*, Application Note, 2008.

[74] Noman Rao, Dinesh Chamund, *Calculating Power Losses in an IGBT Module*, Dynex, Application Note, 2014.

[75] *Growatt CP250 datasheet*, Segen, Growatt New Energy Technology Co., LTD.

[76] Johannes Brombach, Torben Schröter, Arno Lucken, Detlef Schulz, *Optimizing the Weight of an Aircraft Power Supply System through a +/- 270 VDC Main Voltage*,Przeglad Elektrotechniczny, Helmut-Schmidt-University, Airbus Operations GmbH, 2012.

[77] J Pyrhönen, T Jokinen, V. Hrabovocá, *Design of Rotating Electrical Machines*, 2nd edition, John Wiley&Sons, Ltd., 2008.

[78] A. Binder, *High speed PM machines*, Darmstadt, Lectural Note.

[79] *European Corinair manual*, http://reports.eea.europa.eu, 2001

[80] R. Grune, *Verlustoptimaler Betrieb einer elektrisch erregten Synchronmaschine für den Einsatz in Elektrofahrzeugen*, PhD Thesis, School of Electrical Engineering and Computer Science, Berlin, 2013.

[81] https://www.pipistrel.si/, Pipistrell, Slovenia.

[82] Marty K. Bradley, Christopher K. Droney *Subsonic Ultra Green Aircraft Research: Phase II – Volume II – Hybrid Electric Design Exploration*,NASA/CR, Boeing Research and Technology, Huntington Beach, 2015.

[83] Pawel Glowacki, Michal Kawalec, *Quantitative emissions of NO_x, CO and CO_2 during aircraft operations*, ICAS, 36^{th} Congress of the International Council of the Aeronautical Sciences, Daejeon (Korea), September 2016.

[84] Arthur H. Lefebvre, Dilip R. Ballal *Gas Turbine Combustion, Alternative Fuels and Emissions*, CRC Press, Taylor and Francis group, New York, 2010